Boundary Element Method in coil design for Magnetic Resonance Imaging

Teun de Smalen

Technische Universiteit Delft

Boundary Element Method in coil design for Magnetic Resonance Imaging

by

Teun de Smalen

to obtain the degree of Master of Science
at the Delft University of Technology,
to be defended publicly on Wednesday April 21, 2021 at 10:00 AM.

Student number:	4321014	
Project duration:	June 1, 2020 – April 21, 2021	
Thesis committee:	Dr. ir. R.F. Remis,	TU Delft, supervisor
	Prof. dr. A.G. Webb	LUMC & TU Delft
	T. O'Reilly,	LUMC
	Ir. B. de Vos,	LUMC

TU Delft

Abstract

MRI is an non-invasive imaging technique used by many physicians to diagnose and treat diseases. The technique however is still very expensive and thus out of reach for developing countries. This has led to the goal to design a low-cost MRI system. The challenges that arise from this system make it necessary to design coils in a different way than conventional MRI.

In this work the inverse boundary element method is used to create a coil design method for an arbitrary surface. This method is described and the mathematical framework is analyzed. A regularization method for the inverse problem has been designed in the form of a regularization matrix. This regularization matrix is constructed such that it can handle arbitrary surfaces. The regularization matrix is applied using Tikhonov regularization.

To validate the design method a proof of concept radiofrequency coil for the low field MRI system at the LUMC has been realized. This coil is designed and has been used to image the human brain of an adult. The results from simulations beforehand are in agreement with the physically built coil showing that this method makes it possible to design and construct a physically feasible coil on an arbitrary surface.

Acknowledgements

I would like to thank my supervisor Rob Remis. Rob has always been able to make time for me, even in his busy schedule. Giving me good insights in which direction to take with the project.

I am grateful to my daily supervisor, Bart de Vos. Especially during these difficult times he pushed me to every opportunity to go the LUMC. As well as the feedback and input he has given me throughput the project have been a great support.

I would like to thank the people at LUMC who have made it possible to be able to make a physical design, this have been the cherry on top of the project.

Also, I would like to thank my friends for helping me through these sometimes difficult times. The walks, drinks and fish were a welcome distraction during this time.

Lastly, I would like to thank my family for the support throughout all these years.

Contents

1 Introduction

Magnetic Resonance Imaging (MRI) is a powerful non-invasive non-ionizing medical imaging technique. It helps a physician in the making of a diagnosis and detect illnesses in an early stage. The technique is however very expensive in purchase as well as upkeep. Making this technique out of reach for developing countries.

The cost for operating the MRI scanner mostly comes from the superconducting magnets which are kept at a very low temperature using liquid helium. To be able to tackle both the high initial costs as well as the operating costs, a team from the Leiden University Medical Center (LUMC) in a joint collaboration with the Delft University of Technology (TU Delft) have been working on a low-cost MRI scanner. This scanner uses permanent magnets to create the main magnetic field instead of super conducting magnets used in conventional MRI, cutting down on the costs for design and maintenance.

The overarching goal of this project is to create an MRI scanner that costs less than $50.000 that can be exported to low resource African countries in order to treat hydrocephalus in children. Hydrocephalus is a condition causing accumulation of fluid in the brain. This fluid, cerebrospinal fluid (CSF), has functions in protecting the human brain and is constantly new CSF is produced in the body. In hydrocephalus the release of fluid from the brain is interrupted. Accumulating this fluid, which if left untreated is potentially fatal [1]. Current practice uses CT for imaging hydrocephalus in these countries and treated by placing a shunt. CT scans use ionizing radiation which can have disadvantageous effects on the (young) patient, making an affordable MRI scanner a more safe option in imaging hydrocephalus.

1.1. Magnetic Fields in MRI

The magnetic fields produced in an MRI scanner can be split up in three different components. Firstly, the main magnetic field (B_0) is used to polarize the sample in a certain direction. This magnetic field causes protons to have a change in their resonance frequency in the sample. This frequency is related to the magnetic field as

$$\omega = \gamma B. \tag{1.1}$$

Where ω is also known as the Larmor frequency, B is the magnitude of the magnetic flux density and γ is known as the gyromagnetic ratio. The gyromagnetic ratio is specific to a nucleus. The gradient coils within an MRI scanner are used for spatial encoding. In conventional MRI three coils are used in order to describe a point in 3D space. The magnitude of the gradient field is in the B_0 direction, while the field varies in three orthogonal spatial directions. The RF coil creates a magnetic field (B_1) that is perpendicular to the main magnetic field. The RF coil can be seen as the transmit and receive probe. It excites the sample at a frequency near the Larmor frequency and can subsequently measure a signal which can be used to form an image. More information on MRI systems can be found in [2].

1.1.1. Low Field MRI System

In conventional MRI the main magnetic field is directed in the direction of the bore. As briefly touched upon earlier in this section, the low field MRI scanner is made using permanent magnets. These permanent magnets are assembled in a certain configuration known as an Halbach array. This configuration creates a magnetic field that is homogeneous in the direction perpendicular to the axis of the bore. Creating a magnetic field in the x-direction as depicted in Figure 1.1. The mean magnetic field strength is 50.4 mT [3].

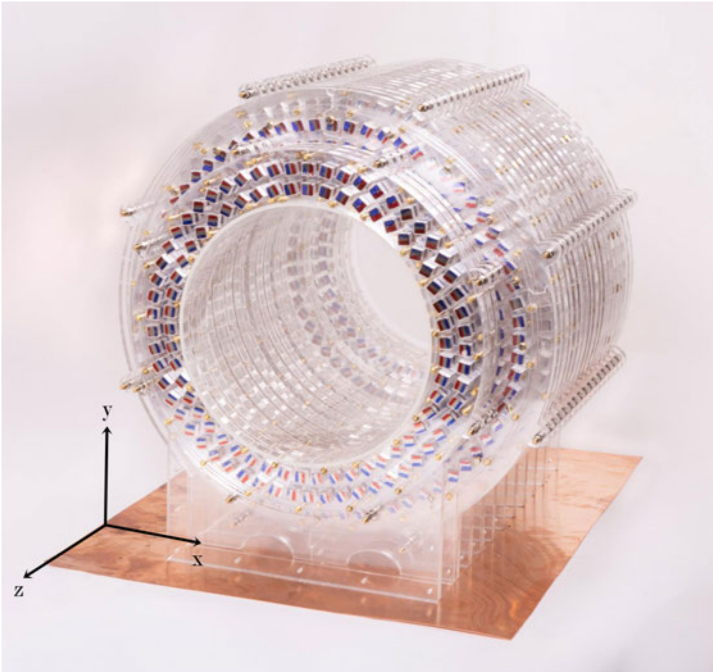

Figure 1.1: LUMC Low Field MRI system using permanent magnets in a Halbach array configuration. Image from Tom O'Reilly [3].

1.1.2. Coil design methods in MRI

As the fields that needed for MRI are very different, multiple coil design techniques exist to create these specific fields. These fields can be categorized in two groups of methods. These groups are the discrete winding methods and distributed winding methods. In the discrete method, current carrying wire loops are placed at certain locations and the magnitude of the current is determined. In Linear Programming, this problem is solved by choosing specific wire locations and optimizing how many loops are placed at each of these locations [4] to get a certain target field. Another method in this group uses discrete wire locations to remove higher order terms in the Taylor expansion of the magnetic field [5]. These methods can be used to very quickly derive a coil design with an accurate solution. However, for the linear programming method wire locations need to be known in advance. For the Taylor expansion the off-axis performance is often poor and high accuracy of wire positions is needed. These methods can only be used to design coils for specific fields.

In distributed winding methods, a current density is optimized to obtain a certain magnetic field. From this current density a wire pattern is deduced often using stream functions. Both analytical- and numerical methods exist to solve this problem. One of these analytical methods is the target field method introduced by Turner [6], where the currents are calculated directly from the specified field by inverting Ampere's Law. Forbes et al. [7] have built upon this method to design coils of finite length. These coil design methods are restricted to finite analytical surfaces on which a coil can be designed. Numerical methods that also may be applied are the Finite Element Method (FEM) and Boundary Element Method (BEM). In the Finite Element Method a computational volume is discretized and meshed. The method however is unsuitable for the inverse source problem considered here, since it is computationally too expensive [8]. In the Boundary Element Method an infinitesimal thin surface is discretized and meshed [9]. This reduces the degree of freedom compared to FEM, such that the problem is less computational expensive. A disadvantage of this method is that the surface should be correctly chosen for the application. Also the precision of calculations is bound by the size of the meshing. More information about coil design methods can be found in [5, 10].

Most coil design methods are bound to certain (analytical) structures or are only able to create coils with small regions of interest. In this work we are going to use the boundary element method to design a method to create coils on arbitrary surfaces.

1.2. Thesis Objective

This thesis focuses on coil design on arbitrary surfaces using the boundary element method in MRI. In particular, the focus is on gradient and RF coil design for which a quasi-static field analysis is applicable. The ultimate goal is to realize a practical design tool, which can be directly applied to the low-field MR systems that are currently under development.

1.3. Organization of the Report

In Chapter 2, the fundamental field equations are presented that relate the surface currents to the magnetic field. In discretized form, this leads to a matrix formulation that links the magnetic flux density and stream function to each other. In Chapter 3 the matrix formulation is used to first show that the forward problem converges for more accurate discretization, followed by solving the ill-posed inverse source problem which describes the design of a coil. Methods of regularization are needed to solve this problem and a regularization matrix is designed to regularize on an arbitrary surface. This method is then compared to other methods of regularization using the design of a gradient coil on a cylindrical shape. This method of regularization is used to design and build a radio-frequency coil in Chapter 4. The coil is used in the Low Field MRI system, to scan the human brain as well as a phantom. Subsequently, the imaging results are than compared to a different radiofrequency coil designed for this low field MRI system. Lastly, in Chapter 5 the conclusions and recommendations of this work are presented.

2

Boundary Element Method for Coil Design

The Boundary Element Method (BEM) is a technique that can be used for analyzing the behavior of a system affected by some external source. This external source is defined on the boundary, where this boundary is defined as an infinitely thin surface. Because the external source lies on this surface, it can be referred to as the *surface quantity* of the BEM problem. The system affected by the external source can be referred to as the *field quantity*. In this chapter the relation between these quantities is determined.

In Section 2.1 the relation between the field quantities and the surface quantities is derived. Followed by Section 2.2 in which we look at the connection between the surface current density and the stream functions. The relations discussed in the preceding sections are then used in Section 2.3 for the design of the matrix formulation of the Boundary Element Method.

2.1. Magnetic Field

The goal of this section is to determine the relation between the target field quantity and the surface quantity. In this problem the target field quantity is the magnetic flux density $\mathbf{B}$ and the surface quantity is the surface current density $\mathbf{J}_s$. The magnetic flux density is the target field prescribed at certain locations, while the surface current density is determined on a specified surface $\mathbb{S}^{\mathbb{src}}$. The fields that will be generated by the surface current density are time-varying fields. As discussed before, in our case these variations are relatively slow and thus the fields can be described using quasi-static analysis. The magnetic fields in this situation can be described by two of the Maxwell's equations in the quasi-static case, namely

$$\nabla \cdot \mathbf{B} = 0 \tag{2.1}$$

and

$$\nabla \times \mathbf{H} = \mathbf{J}, \tag{2.2}$$

where $\mathbf{J}$ is the current density and $\mathbf{H}$ is the magnetic field strength. $\mathbf{B}$ can be described using the constitutive relations [11]

$$\mathbf{B} = \mu_0 \mathbf{H} + \mu_0 \mathbf{M}, \tag{2.3}$$

where $\mathbf{M}$ is the Magnetization and μ_0 is the permeability of vacuum. The current density $\mathbf{J}$ is described on the surface $\mathbb{S}^{\mathbb{src}}$, which is assumed to be enclosed by free-space. Magnetization $\mathbf{M}$ vanishes in this situation, as free-space does not contain any magnetic moments. Equation 2.3 then reduces to

$$\mathbf{B} = \mu_0 \mathbf{H}, \tag{2.4}$$

combined with Equation 2.2 results in

$$\nabla \times \mathbf{B} = \mu_0 \mathbf{J}. \tag{2.5}$$

The divergence given in Equation 2.1 is equal to zero and therefore the magnetic flux density can be written as the curl of a vector potential, which is

$$\mathbf{B} = \nabla \times \mathbf{A}, \tag{2.6}$$

where $\mathbf{A}$ is the vector potential [12]. Combining Equation 2.5 and 2.6 gives

$$\nabla \times (\nabla \times \mathbf{A}) = \mu_0 \mathbf{J}, \tag{2.7}$$

which is the same as

$$\nabla(\nabla \cdot \mathbf{A}) - \nabla^2 \mathbf{A} = \mu_0 \mathbf{J}. \tag{2.8}$$

The divergence of $\mathbf{A}$, given by $\nabla \cdot \mathbf{A}$, can be chosen to get an unique vector field. We take the coulomb gauge which is given by $\nabla \cdot \mathbf{A} = 0$ [13], leading to

$$\nabla^2 \mathbf{A} = -\mu_0 \mathbf{J}. \tag{2.9}$$

This equation is known as Poisson's Equation [12]. For which the solution can be formed using the Green's Function

$$\mathbf{A}(\mathbf{r}) = \frac{\mu_0}{4\pi} \int_{r' \in \mathbb{V}^{src}} \frac{\mathbf{J}(\mathbf{r}')}{|\mathbf{r} - \mathbf{r}'|} \mathrm{d}V. \tag{2.10}$$

If Equations 2.6 and 2.10 are combined, we arrive back at the magnetic flux density $\mathbf{B}$

$$\mathbf{B}(\mathbf{r}) = \nabla \times \left(\frac{\mu_0}{4\pi} \int_{r' \in \mathbb{V}^{src}} \frac{\mathbf{J}(\mathbf{r}')}{|\mathbf{r} - \mathbf{r}'|} \mathrm{d}V \right), \tag{2.11}$$

which can be rewritten as

$$\mathbf{B}(\mathbf{r}) = \frac{\mu_0}{4\pi} \int_{r' \in \mathbb{V}^{src}} \frac{\mathbf{J}(\mathbf{r}') \times (\mathbf{r} - \mathbf{r}')}{|\mathbf{r} - \mathbf{r}'|^3} \mathrm{d}V. \tag{2.12}$$

This equation is known as Biot-Savart law for a volume. The equation describes the relation between the magnetic flux density $\mathbf{B}$ and the current density in a volume. We are looking for a surface quantity instead of a volume quantity, the surface quantity is the surface current density $\mathbf{J}_s$. You can show that the Biot-Savart law for a surface is almost the same as for a volume, only the integral is over a surface instead of a volume. Equation 2.13 describes Biot-Savart law for a surface.

$$\boxed{\mathbf{B}(\mathbf{r}) = \frac{\mu_0}{4\pi} \int_{r' \in \mathbb{S}^{src}} \frac{\mathbf{J_s}(\mathbf{r}') \times (\mathbf{r} - \mathbf{r}')}{|\mathbf{r} - \mathbf{r}'|^3} \mathrm{d}S.} \tag{2.13}$$

The Biot-Savart Law relates the magnetic flux density $\mathbf{B}$ at a specific location $\mathbf{r}$ and the surface current density $\mathbf{J}_s$ at the locations $\mathbf{r}'$. This equation describes the relation where the Boundary Element Method for coil design is built on and will be used in Section 2.3.

2.2. Stream Function

In the previous section a relation between the magnetic flux density $\mathbf{B}$ and the surface current density $\mathbf{J}_s$ has been derived. To be able to physically build a coil, a pattern of current carrying wires is needed. The stream function method is a powerful tool to be able to obtain these wire patterns. In this section the relationship between the surface current density and stream function is determined. Furthermore, some properties of the the stream function and their implications are discussed. The conservation of charge dictates that the charge density at any point in space is related to the current density by the continuity equation for a quasi-static problem

$$\nabla_s \cdot \mathbf{J_s} = 0. \tag{2.14}$$

This equation states that the *surface* divergence of $\mathbf{J_s}$ should be zero. Such that $\mathbf{J_s}$ is source-free, which means there is no charge generated or lost inside the surface. Just as for Equation 2.1 and 2.6, the surface current density can be written as some vector potential $\mathbf{K}$

$$\mathbf{J_s}(\mathbf{r}) = \nabla_s \times \mathbf{K}(\mathbf{r}). \tag{2.15}$$

It is important to note that $\mathbf{r}$ spans the surface over $\mathbb{S}^{\mathrm{src}}$ and not the complete domain. The surface current density flows on a surface, such that the vector potential only has one vector component in the direction of the normal to the surface [14]. Which means, we can rewrite Equation 2.15 as

$$\boxed{\mathbf{J_s}(\mathbf{r}) = \nabla \times \psi(\mathbf{r})\mathbf{n}(\mathbf{r}),} \tag{2.16}$$

where $\mathbf{n}(\mathbf{r})$ is a normal vector pointing outward. $\psi(\mathbf{r})$ is known as the stream function. The stream function is a *scalar* field. As stated earlier in this section the stream function can be used to design coil wire patterns, to be able to deduce these wire patterns from the stream function data some properties are used. As stated earlier in this section we want to use the stream function to design a wire pattern that resembles the surface current density. The first property is related to the streamlines of the stream function, these streamlines are constant values of the stream function ψ. This holds for a three dimensional cartesian coordinate system with a surface where the surface current density is defined on, with an example it can be shown these definitions hold. These properties and proofs are based on [15, 16]. For this example the surface is taken as the xy-plane, since in the next part also a two dimensional cartesian surface is used, such that the surface current density is given as

$$\mathbf{J_s}(\mathbf{r}) = J_{s,x}(\mathbf{r})\hat{\mathbf{x}} + J_{s,y}(\mathbf{r})\hat{\mathbf{y}}. \tag{2.17}$$

The definition of the streamline states that it is tangential to the vector field. The cross product between a vector that is tangent to the surface current density and the surface current density should be equal to zero

$$\mathrm{d}\mathbf{u} \times \mathbf{J_s} = \mathbf{0}. \tag{2.18}$$

Where this tangential component is given as

$$\mathrm{d}\mathbf{u} = \hat{\mathbf{x}}\mathrm{d}x + \hat{\mathbf{y}}\mathrm{d}y + \hat{\mathbf{z}}\mathrm{d}z. \tag{2.19}$$

Solving Equation 2.18 gives the following solutions

$$J_{s,y}\mathrm{d}z = 0, \tag{2.20}$$
$$J_{s,x}\mathrm{d}z = 0, \tag{2.21}$$
$$J_{s,y}\mathrm{d}x - J_{s,x}\mathrm{d}y = 0. \tag{2.22}$$

Rewriting the last equation gives

$$\frac{\mathrm{d}x}{\mathrm{d}y} = \frac{J_{s,x}}{J_{s,y}} \tag{2.23}$$

This equation is the differential equation related to the streamline of the surface current density. We need to show that this is equal to a constant value of the stream function, as this shows that taking a streamline of the stream function is equivalent to a constant flow of the surface current density. The relationship between the surface current density and the stream function can be given using Equation 2.16, where the normal is in the z-direction.

$$\mathbf{J_s}(\mathbf{r}) = \nabla \times \psi(\mathbf{r})\hat{\mathbf{z}} = \frac{\partial \psi}{\partial y}\hat{\mathbf{x}} - \frac{\partial \psi}{\partial x}\hat{\mathbf{y}}. \tag{2.24}$$

Such that the components of the surface current density are given as

$$J_{s,x} = \frac{\partial \psi}{\partial y}, \tag{2.25}$$

$$J_{s,y} = -\frac{\partial \psi}{\partial x}. \tag{2.26}$$

The derivative of the stream function is given as

$$\mathrm{d}\psi = \frac{\partial \psi}{\partial x}\mathrm{d}x + \frac{\partial \psi}{\partial y}\mathrm{d}y. \tag{2.27}$$

Combining this derivative with the components of the surface current density yields

$$\mathrm{d}\psi = -J_{s,y}\mathrm{d}x + J_{s,x}\mathrm{d}y. \tag{2.28}$$

Constant lines means that the derivative should be equal to zero, meaning

$$\mathrm{d}\psi = -J_{s,y}\mathrm{d}x + J_{s,x}\mathrm{d}y = 0. \tag{2.29}$$

Rewriting yields

$$\frac{\mathrm{d}x}{\mathrm{d}y} = \frac{J_{s,x}}{J_{s,y}}. \tag{2.30}$$

This equation is clearly the same as Equation 2.23. Since these equations are the same, the streamlines of the surface current density are the same as constant values of the stream function. Another property of the streamlines for the current density relates the streamlines to current carrying wires. If streamlines of the stream function are taken with constant values $\psi_1 = C$ and $\psi_2 = C + \Delta\psi$. Such that there is a current density flowing between the two levels of the stream function. A current can be determined from the surface current density as

$$I = \int_{\mathcal{L}} \mathbf{J_s} \cdot \mathrm{d}\mathbf{l}. \tag{2.31}$$

Since the surface current density is a conservative vector field, the current density has no path dependency. Such that the segment can be taken in for example the y-direction. Which gives

$$I = \int_{\mathcal{L}} J_{s,x}\mathrm{d}y. \tag{2.32}$$

The x-component of the current density is given in Equation 2.25, substituting into the previous equation gives

$$I = \int_{\mathcal{L}} \frac{\partial \psi}{\partial y} \mathrm{d}y = \int_{\mathcal{L}} \mathrm{d}\psi. \tag{2.33}$$

If we now bound the integral to the streamlines a current difference is given as

$$\Delta I = \int_{\psi_1}^{\psi_2} \mathrm{d}\psi = \int_{C}^{C+\Delta\psi} \mathrm{d}\psi = \Delta\psi. \tag{2.34}$$

So the difference between two streamlevels is analogous to the current difference. This current can be approximated by a current carrying wire equally spaced between the different streamlevels. For coil design, often only one amplifier is used such that only one current level can be generated. If the levels for the streamlines are chosen such that the difference between each level is the same, the current through each wire is the same. Then by stitching the wires together in series, a coil can be designed using only one current level for the current carrying wires. Using the stream functions a current carrying wire pattern can be designed.

2.3. Boundary Element Method

In the boundary element method a surface is discretized in nodes, where the combination of neighboring nodes form elements. Such an element has a triangular shape where the three vertices correspond to three nodes of the discretized surface. Different elements are possible, for example quadrilaterals, however the geometry of the triangle has the advantage that two vertices of the triangle span a plane in which the triangle lies. In this plane any curvature that existed in the undiscretized surface is neglected, this introduces an error. For elements with more than three nodes, these nodes do not necessarily all lie in this plane, which leads to a situation in which the problem can not be simplified in a two dimensional problem or an extra error is introduced. This error would not be introduced for a triangular element, however the amount of elements is required to be higher than for elements with more vertices. This means more calculations need to be done and thus this method is slower than others.

Figure 2.1 depicts an example of a discretized surface where every enclosed triangle is an element. Each element has a unit normal vector, $\mathbf{n}$, associated with it. These normals need to be directed outwards on the same side of the plane for every element.

2.3.1. Discretized Relationship between surface- and field quantity

In the boundary element method, the surface is discretized into nodes and elements. In this section this discretized formulation is derived and a matrix formulation is given. This matrix formulation will be used to find the unknown stream function values. The surface quantity used in the implementation of the Boundary Element Method is not the surface current density $\mathbf{J_s}(\mathbf{r})$, but the stream function $\psi(\mathbf{r})$. Because the stream function is a scalar, the amount of unknowns is less in comparison with the surface current density. As discussed in the previous section, the surface current density can be written as the curl of the stream function as shown in Equation 2.16. The stream function is continuous on the surface $\mathbb{S}_{src}$, in the boundary element method it is approximated by a discretized function given in Equation 2.35.

$$\psi(\mathbf{r}') \approx \sum_{n=1}^{N} I_n \psi_n(\mathbf{r}'), \tag{2.35}$$

where N is the total amount of nodes, $\psi_n(\mathbf{r})$ is the stream function of the nth node and I_n the weight coefficient the nth node. Equations 2.16 and 2.35 can be combined resulting in

$$\mathbf{J_s}(\mathbf{r}') \approx \sum_{n=1}^{N_n} I_n \nabla \times \left[\psi_n(\mathbf{r}')\mathbf{n}(\mathbf{r})\right] = \sum_{n=1}^{N} I_n \mathbf{f}_n(\mathbf{r}'), \tag{2.36}$$

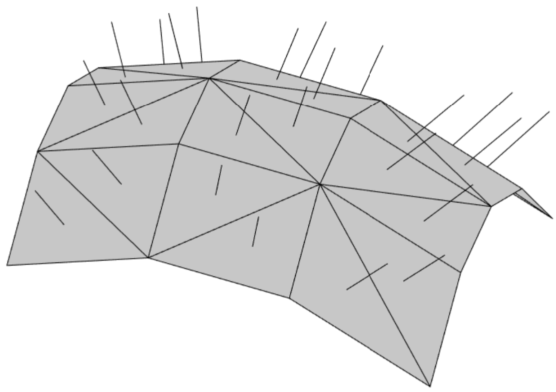

Figure 2.1: An example of a surface discretized into nodes, where each corner of a triangle is a node. Three nodes form an element, the black lines are the normals of each of the elements. Each element has a normal that points in the same direction outwards of the surface.

where $\mathbf{f}_n$ describes the current distribution for node n [17, 18]. The surface current density is given in Equation 2.16 as the curl of the stream function. The discretized surface current density is given as

$$\mathbf{f}_n(\mathbf{r}') = \begin{cases} \mathbf{v}_{n,i}, & \text{if } \mathbf{r}' \text{ belongs to } \Delta_{ni}, \quad i = 1, \ldots, N_n, \\ 0, & \text{elsewhere.} \end{cases} \tag{2.37}$$

where Δ_{ni} denotes the ith element associated with the nth node and $\mathbf{v}_{n,i}$ is the vector associated with node n and element i. In other words, the surface current density of a node is determined using the elements this node is associated with. Where each of these elements has a vector in counter clockwise direction and together describe the discretized curl operation. Figure 2.2 graphically depicts this discretized curl. Using the discretized formulation for the surface current density and thus combining Equations 2.13 and 2.36 the magnetic flux density is written as

$$\mathbf{B}(\mathbf{r}) = \frac{\mu_0}{4\pi} \sum_{n=1}^{N_n} I_n \int_{r' \in \mathbb{S}^{src}} \frac{\mathbf{f_n}(\mathbf{r}') \times (\mathbf{r} - \mathbf{r}')}{|\mathbf{r} - \mathbf{r}'|^3} \mathrm{d}S. \tag{2.38}$$

Where I_n are the unknowns of the boundary element problem and the integrals can be calculated. Using Equation 2.37 the magnetic flux density becomes

$$\mathbf{B}(\mathbf{r}) = \frac{\mu_0}{4\pi} \sum_{n=1}^{N_n} I_n \sum_{i=1}^{N_e} \int_{r' \in \Delta_{ni}} \frac{\mathbf{v}_{ni} \times (\mathbf{r} - \mathbf{r}')}{|\mathbf{r} - \mathbf{r}'|^3} \mathrm{d}S^n. \tag{2.39}$$

Where S^n is the area of element n. If we take

$$\mathbf{A}_n(\mathbf{r}) = \sum_{i=1}^{N_e} \int_{r' \in \Delta_{ni}} \frac{\mathbf{v}_{ni} \times (\mathbf{r} - \mathbf{r}')}{|\mathbf{r} - \mathbf{r}'|^3} dS^n = \sum_{i=1}^{N_e} \mathbf{A}_{n,i}, \tag{2.40}$$

such that

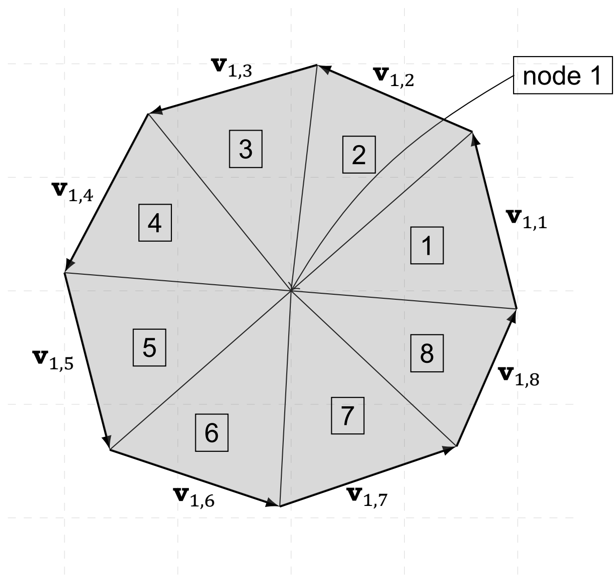

Figure 2.2: Example of a node with the corresponding current basis function $\mathbf{f}_n(\mathbf{r})$. Specific for this example is the node 1, $\mathbf{f}_1$. This node is connected to 8 elements, denoted from 1 up to 8, and 8 vectors corresponding to these specific elements.

$$\mathbf{B}(\mathbf{r}) = \sum_{n=1}^{N} I_n \mathbf{A}_n(\mathbf{r}). \tag{2.41}$$

Where both $\mathbf{B}(\mathbf{r})$ and $\mathbf{A}(\mathbf{r})$ have three components in the cartesian system given as

$$\mathbf{B}(\mathbf{r}) = \begin{bmatrix} B_x(\mathbf{r}) \\ B_y(\mathbf{r}) \\ B_z(\mathbf{r}) \end{bmatrix} \quad \text{and} \quad \mathbf{A_n}(\mathbf{r}) = \begin{bmatrix} A_{n,x}(\mathbf{r}) \\ A_{n,y}(\mathbf{r}) \\ A_{n,z}(\mathbf{r}) \end{bmatrix}. \tag{2.42}$$

If we focus on a specific component, for example the B_x component the formulation becomes

$$B_x(\mathbf{r}) = \sum_{n=1}^{N} I_n A_{n,x}(\mathbf{r}). \tag{2.43}$$

This summation can be given as a vector product if we define the following vectors as

$$\mathbf{x} = \begin{bmatrix} I_1 \\ \vdots \\ I_{N_n} \end{bmatrix} \quad \text{and} \quad \mathbf{a}(\mathbf{r}) = \begin{bmatrix} A_{1,x}(\mathbf{r}) \\ \vdots \\ A_{N_n,x}(\mathbf{r}) \end{bmatrix} \tag{2.44}$$

with dimensions N_n by 1 for both vectors. Such that the vector product is given as

$$B_x(\mathbf{r}) = \mathbf{a}^\top(\mathbf{r})\mathbf{x}. \tag{2.45}$$

Where $\mathbf{x}$ is a vector containing the unknown stream function values. $\mathbf{a}(\mathbf{r})$ is the transfer vector containing the relation between the stream function and the magnetic flux density at location $\mathbf{r}$. If we extend $\mathbf{r}$ to contain all N_t target locations the magnetic flux density can be written as a vector

$$\mathbf{b} = \begin{bmatrix} B_x(\mathbf{r_1}) \\ \vdots \\ B_x(\mathbf{r_{N_t}}) \end{bmatrix} \tag{2.46}$$

with dimensions N_t by 1. Such that vector $\mathbf{a}$ can be extended to a matrix $\mathbf{A}$ to give a matrix formulation

$$\boxed{\mathbf{b} = \mathbf{A}\mathbf{x}.} \tag{2.47}$$

Where $\mathbf{A}$ is

$$\mathbf{A} = \begin{bmatrix} \mathbf{a}(\mathbf{r_1})^\top \\ \vdots \\ \mathbf{a}(\mathbf{r_{N_t}})^\top \end{bmatrix} = \begin{bmatrix} A_{1,x}(\mathbf{r_1}) & \cdots & A_{N_n,x}(\mathbf{r_1}) \\ \vdots & \ddots & \vdots \\ A_{1,x}(\mathbf{r_{N_t}}) & \cdots & A_{N_n,x}(\mathbf{r_{N_t}}) \end{bmatrix} \tag{2.48}$$

The matrix $\mathbf{A}$ is a matrix of with a size of N_t by N_n. This matrix formulation is the system of equations that is used in the boundary element method. Where the $\mathbf{A}$ matrix can be based on the B_x, B_y or B_z component accordingly. The matrix elements of $\mathbf{A}$ need to be determined, in this section the magnetic flux density is determined on a per node basis. However, in the next section it will be shown how the the magnetic flux density is calculated per element instead and how this relates back to an expression per node as we have determined here.

2.3.2. Magnetic flux density created by an element

As discussed previously, the magnetic flux density induced by an element needs to be determined. In this section this is determined for an arbitrary element.
This arbitrary element is a triangle with vertices denoted by nodes P,Q and S and corresponding vectors $\mathbf{p}$, $\mathbf{q}$ and $\mathbf{s}$. The nodes are ordered in a counterclockwise fashion in a right handed coordinate system. The opposing vectors form a counterclockwise rotation. Figure 2.3a denotes the arrangement, the vector opposing to a certain vertex has been given the same letter as that vertex because this vector denotes the effect for that specific vertex as graphically shown in Figure 2.2. We assume that the surface, and thus the element, lies in a cartesian system with corresponding axis x, y and z. In the analysis of an element, to simplify the calculation of the surface integral, the coordinate system is altered. Such that the element under investigation lies in a plane with an axis set to zero and a node at the origin. We denote these axis with u,v, and the third axis will be called w. This change of coordinate system is done using a shift and rotation, Figure 2.3b shows an example of such a change. For every element this shift and rotation are different, such that every element has its own u, v, w coordinate system.
In the next section the transformation to this new coordinate system is discussed. Followed by an analysis of the magnetic flux density produced by an element.

Change of Coordinate System

In this section we discuss the relationship between the xyz-coordinate system and the uvw-coordinate system. If we denote the elements in the uvw-domain with an $'$, a relationship between both of the coordinate systems can be determined. The method used in this section is based on [19]. If we first define the vertices in the xyz-cartesian coordinate system as

$$P = \begin{bmatrix} P_x \\ P_y \\ P_z \end{bmatrix}, \quad Q = \begin{bmatrix} Q_x \\ Q_y \\ Q_z \end{bmatrix}, \quad S = \begin{bmatrix} S_x \\ S_y \\ S_z \end{bmatrix}, \tag{2.49}$$

and then shift these vertices towards the origin where P is located at the origin.

$$P_s = P - P, \quad Q_s = Q - P, \quad S_s = S - P \tag{2.50}$$

Such that a rotation around the origin can be done to rotate towards the uvw-coordinate system.

$$[P' \quad Q' \quad S'] = \mathbf{R}[P_s \quad Q_s \quad S_s]. \tag{2.51}$$

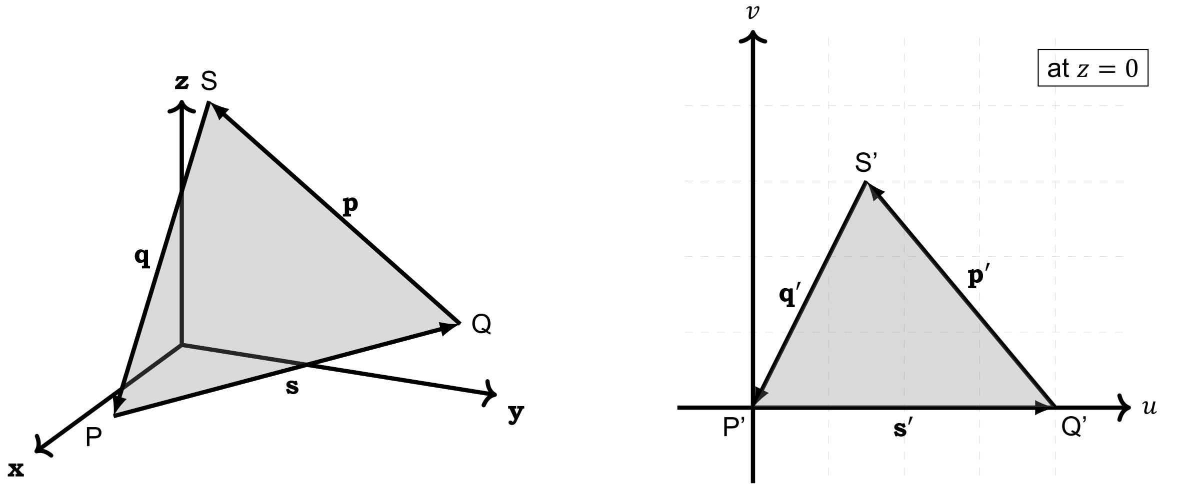

(a) An example of a triangle in the xyz cartesian coordinate system. Where P,Q,S and are the vertices of the triangles, with the opposing side as corresponding vector. The vectors are oriented in the counter-clockwise direction.

(b) An example of a triangle in the uv cartesian coordinate system. Where P',Q',S' and are the vertices of the triangles, with the opposing side as corresponding vector. The vectors are oriented in the counter-clockwise direction.

Figure 2.3: An example of how a triangle is transformed in to the uv-plane.

The vertices are shift by the value of P, such that P lies at the origin of the new coordinate system. $\mathbf{R}$ denotes the rotation matrix used, the rotation matrix is a 3x3 matrix. If we let $\mathbf{R}$ now look like:

$$\mathbf{R} = \begin{bmatrix} \hat{\mathbf{e}}_u^T \\ \hat{\mathbf{e}}_v^T \\ \hat{\mathbf{e}}_w^T \end{bmatrix} = \begin{bmatrix} \hat{\mathbf{e}}_x & \hat{\mathbf{e}}_y & \hat{\mathbf{e}}_z \end{bmatrix} = \begin{bmatrix} e_{u,x} & e_{u,y} & e_{u,z} \\ e_{v,x} & e_{v,y} & e_{v,z} \\ e_{w,x} & e_{w,y} & e_{w,z} \end{bmatrix} \tag{2.52}$$

where $\hat{\mathbf{e}}_u$, $\hat{\mathbf{e}}_v$, $\hat{\mathbf{e}}_w$, $\hat{\mathbf{e}}_x$, $\hat{\mathbf{e}}_y$ and $\hat{\mathbf{e}}_z$ are all column-vectors. The arms of the triangle should stay the same length for ease of implementation, the second node, Q, will be placed along the u-axis. If all arms stay the same length $\mathbf{R}$, and thus are unit length and orthogonal it can be said that the triangles' arms are still the same length. Thus $\hat{\mathbf{e}}_u$, $\hat{\mathbf{e}}_v$, $\hat{\mathbf{e}}_w$ are unit-vectors. The matrix will then be an orthonormal matrix, such that

$$\mathbf{R}^{-1} = \mathbf{R}^T \quad \text{and} \quad \mathbf{R}^T\mathbf{R} = \mathbf{I}, \tag{2.53}$$

where $\mathbf{I}$ is the identity matrix. Every element of the matrix $\mathbf{R}$ denotes the corresponding effect from each specific variable of xyz onto uvw and vice versa, i.e. $e_{u,x}$ is the effect from u on x or vice versa. Looking at Figure 2.3b, we want Q_s to be located at the u-axis, the top row-vector $\hat{\mathbf{e}}_u$ should map that. Which gives

$$\hat{\mathbf{e}}_u = \frac{1}{||\mathbf{s}||_2}\mathbf{s} \tag{2.54}$$

where $\mathbf{s}$ is the vector from the node P to node Q and from the origin to node Q_s as seen in Figure 2.3a. For $\hat{\mathbf{e}}_w$ we know that it should be orthogonal to $\hat{\mathbf{e}}_u$ and also orthogonal to the arms of the triangle that will lie in the uv-plane. These arms are $\mathbf{p}$ and $\mathbf{q}$ an arbitrary choice can be made, resulting in

$$\hat{\mathbf{e}}_u \cdot \hat{\mathbf{e}}_w = 0 \tag{2.55}$$

and

$$\mathbf{q} \cdot \hat{\mathbf{e}}_w = 0 \tag{2.56}$$

Which yields the result

$$\hat{\mathbf{e}}_w = \frac{1}{\|\hat{\mathbf{e}}_u \times \mathbf{q}\|}\hat{\mathbf{e}}_u \times \mathbf{q}. \tag{2.57}$$

Lastly $\hat{\mathbf{e}}_v$ needs to be determined, as this is perpendicular to both $\hat{\mathbf{e}}_u$ and $\hat{\mathbf{e}}_w$ it can be given as

$$\hat{\mathbf{e}}_v = \frac{1}{\|\hat{\mathbf{e}}_w \times \hat{\mathbf{e}}_u\|}(\hat{\mathbf{e}}_w \times \hat{\mathbf{e}}_u). \tag{2.58}$$

For a different point in space $\mathbf{r}$ in the xyz cartesian system the location in the uvw cartesian, denoted by $\mathbf{d}$, can be determined as

$$\boxed{\mathbf{d} = \mathbf{R}(\mathbf{r} - P).} \tag{2.59}$$

The inverse relation is given by

$$\boxed{\mathbf{r} = \mathbf{R}^{-1}\mathbf{d} + P = \mathbf{R}^{\mathsf{T}}\mathbf{d} + P.} \tag{2.60}$$

With these relations established, we can determine the magnetic flux density created by an element.

Surface current density within an element

For an element with nodes P,Q and S and corresponding vectors $\mathbf{p}$, $\mathbf{q}$ and $\mathbf{s}$ we want to determine what the magnetic flux density is at certain locations due to this specific element. The nodes all have corresponding nodal coordinates in a cartesian system. For ease of computation the plane in which this element lies is coupled to a coordinate system u, v and w. Where the triangle lies in the u, v-plane as discussed in the previous section, Figure 2.3 gives a graphical view on the problem.

First we show how the divergence of the transformed coordinate system can be given and is proven. Followed by a derivation of the stream function within that transformed element. Lastly this stream function is used to determine the magnetic flux density due to an element. The method used in this section is based on Pissanetzky [9]. Where Pissanetzky starts of with the partial derivatives in Equation 2.71 and 2.72 and then moves on to the surface current density for an element in Equation 2.94. In this thesis the foundation on which these equations are determined and their derivations are given. The surface current density within an element, $\mathbf{J}_\mathbf{s}^\mathbf{e}$, must satisfy the continuity equation. For a cartesian coordinate system xyz the continuity equation is given as

$$\nabla_{xyz} \cdot \mathbf{J}_\mathbf{s}^\mathbf{e} = \frac{\partial J^e_{s;x}}{\partial x} + \frac{\partial J^e_{s;y}}{\partial y} + \frac{\partial J^e_{s;z}}{\partial z}. \tag{2.61}$$

Where ∇_{xyz} is the divergence in the xyz coordinate system. For the transformed coordinate system in uvw we now show that for an arbitrary $\mathbf{R}$, that is a unitary matrix, the continuity equation is

$$\nabla_{uvw} \cdot \mathbf{J}_\mathbf{s}^\mathbf{e} = \frac{\partial J^e_{s;u}}{\partial u} + \frac{\partial J^e_{s;v}}{\partial v} + \frac{\partial J^e_{s;w}}{\partial w}. \tag{2.62}$$

If we take for example the u-component, by using the chain rule for partial derivatives it can be given in terms of x, y and z;

$$\frac{\partial J^e_{s;u}}{\partial u} = \frac{\partial J^e_{s;u}}{\partial x}\frac{\partial x}{\partial u} + \frac{\partial J^e_{s;u}}{\partial y}\frac{\partial y}{\partial u} + \frac{\partial J^e_{s;u}}{\partial z}\frac{\partial z}{\partial u}. \tag{2.63}$$

Where the components of this expression can be determined using the expression for the Rotation Matrix in Equation 2.52 given as

$$\frac{\partial x}{\partial u} = e_{u,x}, \quad \frac{\partial y}{\partial u} = e_{u,y}, \quad \frac{\partial z}{\partial u} = e_{u,z} \tag{2.64}$$

and

$$\frac{\partial J^e_{s;u}}{\partial x} = \frac{\partial J^e_{s;x}}{\partial x} e_{u,x}, \quad \frac{\partial J^e_{s;u}}{\partial y} = \frac{\partial J^e_{s;y}}{\partial y} e_{u,y}, \quad \frac{\partial J^e_{s;u}}{\partial z} = \frac{\partial J^e_{s;z}}{\partial x} e_{u,z} \tag{2.65}$$

Such that the partial derivative of is given by

$$\frac{\partial J^e_{s;u}}{\partial u} = \frac{\partial J^e_{s;x}}{\partial x} e^2_{u,x} + \frac{\partial J^e_{s;y}}{\partial y} e^2_{u,y} + \frac{\partial J^e_{s;z}}{\partial x} e^2_{u,z} \tag{2.66}$$

The same can be done for the other partial derivatives $\frac{\partial J^e_{s;v}}{\partial v}$ and $\frac{\partial J^e_{s;w}}{\partial w}$. Combining these equations with Equation 2.62 and reordering the components the following expression is obtained

$$\nabla \cdot \mathbf{J^e_s} = \frac{\partial J_{s;x}}{\partial x}(e^2_{u,x} + e^2_{v,x} + e^2_{w,x}) + \frac{\partial J_{s;y}}{\partial y}(e^2_{u,y} + e^2_{v,y} + e^2_{w,y}) + \frac{\partial J_{s;z}}{\partial z}(e^2_{u,z} + e^2_{v,z} + e^2_{w,z}). \tag{2.67}$$

This is the same as

$$\nabla_{uvw} \cdot \mathbf{J^e_s} = \frac{\partial J_{s;x}}{\partial x}\|\mathbf{e_x}\|^2_2 + \frac{\partial J_{s;y}}{\partial y}\|\mathbf{e_y}\|^2_2 + \frac{\partial J_{s;z}}{\partial z}\|\mathbf{e_z}\|^2_2. \tag{2.68}$$

Since the vectors $\mathbf{e_x}$, $\mathbf{e_y}$ and $\mathbf{e_z}$ are unit-vectors their corresponding norms are 1 and thus the equation can be further simplified.

$$\nabla_{uvw} \cdot \mathbf{J^e_s} = \frac{\partial J^e_{s;x}}{\partial x} + \frac{\partial J^e_{s;y}}{\partial y} + \frac{\partial J^e_{s;z}}{\partial z} = \nabla_{xyz} \cdot \mathbf{J^e_s}. \tag{2.69}$$

It is now clear that indeed for an arbitrary unitary rotation matrix $\mathbf{R}$ the continuity equation is indeed given by Equation 2.62. For the continuity equation for an element in the uv-plane, the w component is zero. Such that the continuity equation is given as

$$\frac{\partial J^e_{s;u}}{\partial u} + \frac{\partial J^e_{s;v}}{\partial v} = 0. \tag{2.70}$$

For which the solution as function of the stream function is given by

$$J^e_{s;u} = \frac{\partial \psi}{\partial v} \tag{2.71}$$

and

$$J^e_{s;v} = -\frac{\partial \psi}{\partial u}. \tag{2.72}$$

The vertices in uv-plane are denoted by P', Q' and S' as discussed in the previous section. Their corresponding vectors in the uv-plane are $\mathbf{p}'$, $\mathbf{q}'$ and $\mathbf{s}'$ which can be expressed as

$$\mathbf{p}' = \begin{bmatrix} p'_u \\ p'_v \end{bmatrix}, \mathbf{q}' = \begin{bmatrix} q'_u \\ q'_v \end{bmatrix} \text{ and } \mathbf{s}' = \begin{bmatrix} s'_u \\ s'_v \end{bmatrix}. \tag{2.73}$$

For every node a corresponding stream function value is used, denoted by I_p, I_q and I_s. These values are the unknowns in the inverse boundary element problem. In the next part we will show how both the stream function and the surface current density relate to these unknowns. We take the stream function as linear in both u and v and at the location of each of the nodes we want the stream function to be that specific value. Which gives the following form of the stream function

$$\psi(u,v) = Au + Bv + C, \tag{2.74}$$

where A, B and C are scalar values. We know that at the location of a specific vertex, the stream function should be equal to the corresponding nodal value of the stream function. For example at the locations of node P' the stream function should be equal to I_p. For every specific node these requirements are given as

$$\psi(P') = I_p, \quad \psi(Q') = I_q \quad \text{and} \quad \psi(S') = I_s. \tag{2.75}$$

We know that P' lies at the origin, resulting in

$$\psi(P') = \psi(0,0) = I_p. \tag{2.76}$$

So the constant C is equal to I_p. On the location of nodes Q' and S' the stream function values should be I_q and I_s consequently

$$\psi(Q') = Au + Bv + I_p = I_q, \tag{2.77}$$

and

$$\psi(S') = Au + Bv + I_p = I_s. \tag{2.78}$$

Where Q' is located at the location the end of the vector $\mathbf{p}'$ and S' is located at the beginning of the vector $\mathbf{q}'$ as can be seen in Figure 2.3b. Using the notation given in Equation 2.73 the following expressions can be given:

$$\psi(Q') = \psi(p'_u, p'_v) = Ap'_u + Bp'_v + I_p = I_q, \tag{2.79}$$

and

$$\psi(S') = \psi(-q'_u, -q'_v) = A(-q'_u) + B(-q'_v) + I_p = I_s. \tag{2.80}$$

The unknowns of the stream function are A and B, since we have two equations and two unknowns this problem can be solved. Using Equation 2.79 we get

$$A = \frac{I_s - I_p - B(-q'_v)}{-q'_u}. \tag{2.81}$$

Filling into to Equation 2.80 gives

$$\psi(S') = \frac{I_s - I_p - B(-q'_v)}{-q'_u} s'_u + Bs'_v + I_p = I_q. \tag{2.82}$$

We want the unknown variable B so rewriting the previous Equation presents

$$B\left(s'_v - \frac{q'_v}{q'_u} s'_u\right) = I_q - I_p + (I_s - I_p)\frac{s'_u}{q'_u}. \tag{2.83}$$

Further rewriting separates B from all other variables gives

$$B = \frac{q'_u(I_q - I_p) + s'_u(I_s - I_p)}{s'_v q'_u - s'_u q'_v}. \tag{2.84}$$

The denominator can be rewritten using the Shoelace formula [20], that states that the area of the triangle is given by

$$S^e = \frac{1}{2}|\mathbf{s}' \times -\mathbf{q}'| = |s'_v q'_u - s'_u q'_v|. \tag{2.85}$$

Where the magnitude of the cross product is equal to the area of the polygon formed by $\mathbf{s}'$ and $-\mathbf{q}'$. Since the triangle in our problem is in the first quadrant and thus the absolute value is not needed, the denominator is equal to twice the surface area of the triangle denoted by S^e, some further rewriting yields

$$B = \frac{1}{2S^e}\big(I_q q'_u + I_s s'_u + I_p(-q'_u - s'_u)\big). \tag{2.86}$$

If we sum the three vectors $\mathbf{p}'$, $\mathbf{q}'$ and $\mathbf{s}'$ the result is zero as can be seen in Figure 2.3b, so

$$\mathbf{p}' + \mathbf{q}' + \mathbf{s}' = \mathbf{0}. \tag{2.87}$$

So for the u-component

$$p'_u = -q'_u - s'_u. \tag{2.88}$$

Which gives

$$B = \frac{1}{2S^e}(I_q q'_u + I_s s'_u + I_p p'_u). \tag{2.89}$$

Similar rewriting can be done for A. Filling Equation 2.89 into Equation 2.81 and using similar steps as for B results in

$$A = -\frac{1}{2S^e}(I_q q'_v + I_s s'_v + I_p p'_v). \tag{2.90}$$

The unknowns determined in Equations 2.89 and 2.90 can be filled into Equation 2.74 which yields

$$\psi(u,v) = \frac{1}{2S^e}\Big[-(I_p p'_v + I_q q'_v + I_s s'_v)u + (I_p p'_u + I_q q'_u + I_s s'_u)v\Big] + I_p. \tag{2.91}$$

This expression describes the stream function within an element with respect to the value at the vertices of the element. Using the equations derived from the continuity equation, Equations 2.71 and 2.72, we can derive the components of the surface current density. These components are

$$J^e_{s;u}(u,v) = \frac{1}{2S^e}(I_p p_u + I_q q_u + I_s s_u) \tag{2.92}$$

and

$$J^e_{s;v}(u,v) = \frac{1}{2S^e}(I_p p_v + I_q q_v + I_s s_v). \tag{2.93}$$

These two equations can be combined to the surface current density as

$$\boxed{\mathbf{J_s^e}(u,v) = \begin{bmatrix} J^e_{S;u} \\ J^e_{S;v} \end{bmatrix} = \frac{1}{2S^e}(I_p\mathbf{p} + I_q\mathbf{q} + I_s\mathbf{s}).} \tag{2.94}$$

The surface current density $\mathbf{J_s}$ is constant throughout the element, as it does not depend on u or v. The stream function is linear within an element and piece-wise linear over the complete discretized surface. For a specific element, the difference between two values at specific nodes is equal to the amount of current entering or leaving via that specific edge of the triangle. For example the difference between the stream function at nodes P and Q is $I_p - I_q$, which is the current entering/leaving through that side of the triangle as shown in Section 2.2.

Magnetic flux density proced by an element

With an equation for the surface current density containing the unknowns of the problem the magnetic flux density $\mathbf{B_t^e}(\mathbf{d})$ due to this specific element on a specific location can be determined using Equation 2.13 and is given as

$$\mathbf{B_t^e}(\mathbf{d}) = \frac{\mu_0}{4\pi} \iint_{\mathbf{d}' \in S} \frac{\mathbf{J_s^e}(\mathbf{d}') \times (\mathbf{d} - \mathbf{d}')}{|\mathbf{d} - \mathbf{d}'|^3} \mathrm{d}S^e. \tag{2.95}$$

Where $\mathbf{d}$ and $\mathbf{d}'$ denote the coordinates in the uvw cartesian system. The components of $\mathbf{B_t^e}(\mathbf{d})$ are also in the uvw system, such that the components are $B^e_{t;u}$, $B^e_{t;v}$ and $B^e_{t;w}$. However, the components in the xyz system are needed, B^e_x, B^e_y and B^e_z. To get these specific components, a conversion is needed. In the next set of Equations, this conversion is shown. The conversion of the coordinate systems is given in Equation 2.59. If we plug this into Equation 2.95 in for the field point $\mathbf{d}$, we obtain

$$\mathbf{B_t^e}(\mathbf{r}) = \frac{\mu_0}{4\pi} \iint_{\mathbf{d}' \in S^e} \frac{\mathbf{J_s^e}(\mathbf{d}') \times (\mathbf{R_e}(\mathbf{r} - P) - \mathbf{d}')}{|\mathbf{R_e}(\mathbf{r} - P) - \mathbf{d}'|^3} \mathrm{d}S^e. \tag{2.96}$$

Where R_e is the rotation specific for this element. As stated earlier $\mathbf{J_s^e}$ is constant throughout an element and therefore it is independent of $\mathbf{d}'$, such that the equation can be rewritten as

$$\mathbf{B_t^e}(\mathbf{r}) = \frac{\mu_0}{4\pi}\mathbf{J_s^e} \times \iint_{d' \in S^e} \frac{(\mathbf{R_e}(\mathbf{r} - P) - \mathbf{d}')}{|\mathbf{R_e}(\mathbf{r} - P) - \mathbf{d}'|^3} \mathrm{d}S^e. \tag{2.97}$$

If we now rewrite this equation as a vector product. The magnetic flux density can be given as

$$\mathbf{B_t^e}(\mathbf{r}) = \begin{bmatrix} J^e_{S;u} \\ J^e_{S;v} \\ 0 \end{bmatrix} \times \mathbf{C^e} \tag{2.98}$$

where $\times$ is the cross-product and the third component of the surface current density $J^e_{S;w}$ is zero by design and where $\mathbf{C^e}$ is the integral given as

$$\mathbf{C^e} = \frac{\mu_0}{4\pi} \iint_{d' \in S^e} \frac{(\mathbf{R_e}(\mathbf{r} - P) - \mathbf{d}')}{|\mathbf{R_e}(\mathbf{r} - P) - \mathbf{d}'|^3} \mathrm{d}S^e, \tag{2.99}$$

where $\mathbf{C^e}$ is a vector with components in uvw domain. Given as

$$\mathbf{C} = \begin{bmatrix} C^e_u \\ C^e_v \\ C^e_w \end{bmatrix}. \tag{2.100}$$

The integrals in $\mathbf{C^e}$ are solved by discretization using the two-dimensional midpoint-rule [21]. The discretization is given as

$$\mathbf{C^e} \approx \frac{\mu_0}{4\pi} \sum_{i=1}^{N} \sum_{j=1}^{M} \begin{cases} \frac{(\mathbf{R_e}(\mathbf{r}-P)-\mathbf{d'_{i,j}})}{|\mathbf{R_e}(\mathbf{r}-P)-\mathbf{d'_{i,j}}|^3} \Delta u \Delta v, & \text{if } \mathbf{d'_{i,j}} \in S^e, \\ 0, & \text{elsewhere} \end{cases} \tag{2.101}$$

where Δu and Δv are the distances between midpoints in the u and v direction consequently. The location $\mathbf{d'_{i,j}}$ is given as

$$\mathbf{d'_{i,j}} = \begin{bmatrix} u_i \\ v_j \end{bmatrix}. \tag{2.102}$$

Where u_i and v_j correspond to the locations on the discretized grid. By combining Equations 2.98 and 2.100 the magnetic flux density is given as

$$\mathbf{B^e_t}(\mathbf{r}) = \begin{bmatrix} J^e_{s;u} \\ J^e_{s;v} \\ 0 \end{bmatrix} \times \begin{bmatrix} C^e_u \\ C^e_v \\ C^e_w \end{bmatrix} = \begin{bmatrix} J^e_{s;v} C^e_w \\ -J^e_{s;u} C^e_w \\ J^e_{s;u} C^e_v - J^e_{s;v} C^e_u \end{bmatrix}. \tag{2.103}$$

The components of the surface current density $\mathbf{J^e_s}$ contain the unknowns I's and thus need to be separated. The formulation can be rewritten as

$$\mathbf{B^e_t}(\mathbf{r}) = \begin{bmatrix} 0 & C^e_w \\ C^e_w & 0 \\ C^e_v & -C^e_u \end{bmatrix} \begin{bmatrix} J^e_{s;u} \\ J^e_{s;v} \end{bmatrix} = \begin{bmatrix} 0 & C^e_w \\ -C^e_w & 0 \\ C^e_v & -C^e_u \end{bmatrix} \mathbf{J^e_s} \tag{2.104}$$

The translation of the vector components of the magnetic flux density in the coordinate system uvw, given as $\mathbf{B^e_t}$, to the magnetic flux density in the xyz coordinate system can be given as an inverse rotation. Which is given as

$$\begin{bmatrix} B^e_x(\mathbf{r}) \\ B^e_y(\mathbf{r}) \\ B^e_z(\mathbf{r}) \end{bmatrix} = \mathbf{R_e}^{-1} \begin{bmatrix} B^e_{t;u}(\mathbf{r}) \\ B^e_{t;v}(\mathbf{r}) \\ B^e_{t;w}(\mathbf{r}) \end{bmatrix}. \tag{2.105}$$

Combining Equations 2.104 and 2.105 gives

$$\begin{bmatrix} B^e_x(\mathbf{r}) \\ B^e_y(\mathbf{r}) \\ B^e_z(\mathbf{r}) \end{bmatrix} = \mathbf{R_e}^{-1} \begin{bmatrix} 0 & C^e_w \\ -C^e_w & 0 \\ C^e_v & -C^e_u \end{bmatrix} \mathbf{J^e_s}. \tag{2.106}$$

Equation 2.94 describing the surface current density can also be written as a dot product between two vectors

$$\mathbf{J^e_s} = \frac{1}{2S^e} \begin{bmatrix} \mathbf{p'} & \mathbf{q'} & \mathbf{s'} \end{bmatrix} \begin{bmatrix} I_p \\ I_q \\ I_s \end{bmatrix} \tag{2.107}$$

Resulting in a complete formulation of the magnetic flux density for an element as

$$\begin{bmatrix} B^e_x(\mathbf{r}) \\ B^e_y(\mathbf{r}) \\ B^e_z(\mathbf{r}) \end{bmatrix} = \frac{1}{2S^e} \mathbf{R_e}^{-1} \begin{bmatrix} 0 & C^e_w \\ -C^e_w & 0 \\ C^e_v & -C^e_u \end{bmatrix} \begin{bmatrix} \mathbf{p'} & \mathbf{q'} & \mathbf{s'} \end{bmatrix} \begin{bmatrix} I_p \\ I_q \\ I_s \end{bmatrix}. \tag{2.108}$$

This equation shows how the different nodes of the stream function ψ influence the magnetic flux density. In the last step, we separate the elements of ψ by placing them on the diagonal of a matrix such that the output becomes the matrix

$$\begin{bmatrix}\mathbf{B}^{P;e} & \mathbf{B}^{Q;e} & \mathbf{B}^{S;e}\end{bmatrix} = \frac{1}{2S^e}\mathbf{R_e}^{-1}\begin{bmatrix} 0 & C_w^e \\ -C_w^e & 0 \\ C_v^e & -C_u^e \end{bmatrix}\begin{bmatrix}\mathbf{p}' & \mathbf{q}' & \mathbf{s}'\end{bmatrix}\begin{bmatrix} I_p & 0 & 0 \\ 0 & I_q & 0 \\ 0 & 0 & I_s \end{bmatrix}. \tag{2.109}$$

where $\mathbf{B^{P;e}}$, $\mathbf{B^{Q;e}}$ and $\mathbf{B^{S;e}}$ denote the vectors containing the components of the magnetic flux density corresponding to that specific node in relation to the element being evaluated. Using this notation, every column of the output corresponds to the magnetic flux density value according to that stream function node.

If we look specifically at node P, this equation becomes

$$\mathbf{B}^{P;e} = \frac{I_p}{2S^e}\mathbf{R_e}^{-1}\begin{bmatrix} 0 & C_w^e \\ -C_w^e & 0 \\ C_v^e & -C_u^e \end{bmatrix}\mathbf{p}'. \tag{2.110}$$

This formulation describes how the magnetic flux density created by an element looks like. In the next section this formulation is used to determine the magnetic flux density created by a node.

2.3.3. Magnetic flux density created by a node

The goal of this section is to find the elements of the matrix $\mathbf{A}$ as discussed in Section 2.3.1. In Section 2.3.1 this matrix has been given as

$$\mathbf{A} = \begin{bmatrix} \mathbf{a}(\mathbf{r_1})^\top \\ \vdots \\ \mathbf{a}(\mathbf{r_{N_t}})^\top \end{bmatrix} = \begin{bmatrix} A_{1,x}(\mathbf{r_1}) & \dots & A_{N_n,x}(\mathbf{r_1}) \\ \vdots & \ddots & \vdots \\ A_{1,x}(\mathbf{r_{N_t}}) & \dots & A_{N_n,x}(\mathbf{r_{N_t}}) \end{bmatrix}.$$

These elements are the magnetic flux densities created by a node. These elements are the x-component of $\mathbf{A}_n$ which in Section 2.3.1 has been given as

$$\mathbf{A}_n(\mathbf{r}) = \sum_{i=1}^{N_e}\int_{r'\in\Delta_{ni}} \frac{\mathbf{v}_{ni}\times(\mathbf{r}-\mathbf{r}')}{|\mathbf{r}-\mathbf{r}'|^3}dS^n = \sum_{i=1}^{N_e}\mathbf{A}_{n,i}.$$

This equation is a sum over all N_e elements, the summand $\mathbf{A}_{n,i}$ can be related to the formulation given in Equation 2.110. Where node P is replaced by n and element e is replaced by i. The following equation is determined

$$\mathbf{A}_{n,i}(\mathbf{r}) = \mathbf{B}^{n;i} = \frac{I_n}{2S^n}\mathbf{R_i}^{-1}\begin{bmatrix} 0 & C_w^i \\ C_w^i & 0 \\ C_v^i & -C_u^i \end{bmatrix}\mathbf{v}'_{ni}, \tag{2.111}$$

where $\mathbf{v}'_{ni}$ is given as

$$\mathbf{v}'_{ni} = \begin{bmatrix} \hat{\mathbf{e}}_{u,i} \\ \hat{\mathbf{e}}_{v,i} \end{bmatrix}\mathbf{v}_{ni}. \tag{2.112}$$

If we, as in Section 2.3.1, want the B_x-component of the magnetic flux density, only the top row of $\mathbf{R^{-1}}$ is needed. As discussed at the formalism of $\mathbf{R}$, the rotation matrix is orthonormal and thus $\mathbf{R^{-1}} = \mathbf{R}^\top$.

Using Equation 2.52, the top row of $\mathbf{R}^\top$ is given by $\mathbf{e}_x^\top$. Such that for the x-component of $\mathbf{A}_{n,i}$ is given by

$$A_{n,i,x}(\mathbf{r}) = \frac{1}{I_n}\mathbf{B}^{n;i} = \frac{1}{2S^n}\mathbf{e}_{i,x}^\top \begin{bmatrix} 0 & C_w^i \\ C_w^i & 0 \\ C_v^i & -C_u^i \end{bmatrix} \mathbf{v}'_{ni}. \tag{2.113}$$

In the matrix $\mathbf{A}$ the x-components of each node is specified denoted by $A_{n,x}(\mathbf{r})$, which is equal to

$$A_{n,x}(\mathbf{r}) = \sum_{i=1}^{N_e} A_{n,i,x} = \sum_{i=1}^{N_e} \frac{1}{2S^n}\mathbf{e}_{i,x}^\top \begin{bmatrix} 0 & C_w^i \\ C_w^i & 0 \\ C_v^i & -C_u^i \end{bmatrix} \mathbf{v}'_{ni}. \tag{2.114}$$

By using this equation for different locations $\mathbf{r}$ the matrix $\mathbf{A}$ can be filled. As given in Section 2.3.1, the matrix formulation is given as

$$\mathbf{b} = \mathbf{A}\mathbf{x}.$$

This matrix formulation will be used in the forward- and inverse problems discussed in the next chapter.

3

Forward- and Inverse Source Problem

In this chapter the forward- and inverse source problem of the Boundary Element Method are discussed. In the previous chapter the relation between the magnetic flux density and the stream function has been discussed and a matrix representation has been developed. This matrix representation is given as

$$\mathbf{b} = \mathbf{A}\mathbf{x}.$$

Where $\mathbf{b}$ is a vector containing the magnetic flux density at each of the locations. Vector $\mathbf{x}$ contains the stream function values at each of the nodes. The matrix $\mathbf{A}$ contains the relation between both of these quantities. In the next section, Section 3.1, the forward problem is discussed, which means the magnetic flux density, $\mathbf{b}$, is assumed to be unknown. Results on convergence and possible errors are discussed. Followed by the inverse source problem in Section 3.2. In the inverse source problem the stream function values, $\mathbf{x}$, are unknown. This problem is less trivial to solve and different methods of solving this problem are discussed.

3.1. Forward Problem

As discussed in the introduction of this section, the forward problem gives a solution for the unknown magnetic flux density $\mathbf{b}$. The goal of solving this forward source problem is to verify expectations and show the possible drawbacks of this matrix formulation. This verification is done using a problem of which we know the analytical solution, a Helmholtz coil. First the design and analytical solution are discussed, followed by the designs used for the verification. Lastly the results of the analytical solution and the simulation are compared.

3.1.1. Setup of analytical solution

The configuration used is a Helmholtz coil [22]. A Helmholtz coil consists of two coils with radius a positioned opposite to each other at a distance a, in both coils a current I flows in the same direction. Figure 3.1 graphically depicts the configuration. The Helmholtz coil has a straightforward analytical solution for the axial component along the axes of the configuration [22]. In our setup shown in Figure 3.1 this is the z-component along the z-axis. The corresponding equation for the magnetic flux density becomes

$$B_z(0,0,z) = \frac{\mu_0 I a^2}{2\left[(d/2 - z)^2 + a^2\right]^{3/2}} + \frac{\mu_0 I a^2}{2\left[(d/2 + z)^2 + a^2\right]^{3/2}}. \tag{3.1}$$

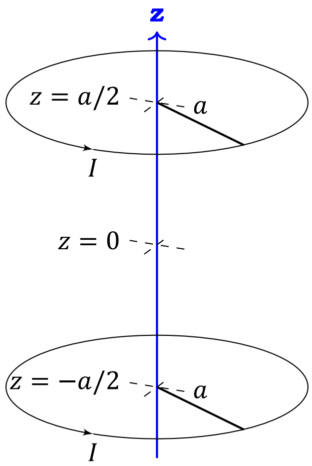

Figure 3.1: Configuration of the Helmholtz coil pair used in the comparison of the forward problem.

3.1.2. Simulation designs

To verify the Boundary Element Method two different configurations are used. These designs are depicted in Figures 3.2 and 3.3. The first model, Figure 3.2, is a design consisting of two plates. These plates are separated a distance of a apart, where a is the same as in the analytical problem. The plates has a size of $3a$ by $3a$, such that the complete loop lies within the surface. The second design, Figure 3.3, is a cylinder with a radius that is equal to the radius of the coils a. The length of the cylinder is longer than the distance the coils are apart.

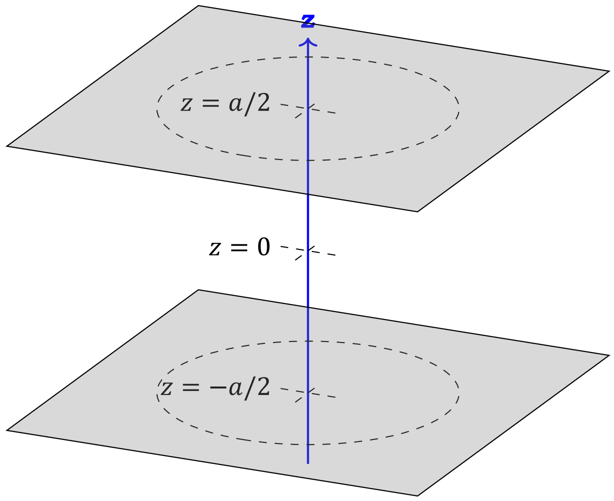

Figure 3.2: Two plate configuration used in the simulation, the dashed circle are the locations of the coils as described in Figure 3.1. The gray area describes the location where the boundary element method will be performed on $\mathcal{S}^{src}$.

The two plate configuration is chosen to see the effect on the magnetic flux density if a line with a certain curvature is approximated by a piece-wise linear grid. The second method is chosen to see what the effect is of the approximation of flattening a cylindrical surface into the planes the triangles live in. This is nicely depicted by Kukaba [23] and shown in Figure 3.4.

To perform these simulations the stream function needs to be determined on the discretized surface. The stream function values at any location can be determined by choosing a starting point and using a line integral over the surface current density given in Section 2.2. The surface current density is derived from the analytical solution. Meaning, from the current flowing through the Helmholtz coil an analytical stream function is determined. This stream function is then discretized on the specific surface. Two examples of these discretized stream functions on the surface are given in Figure 3.5a and Figure 3.5b.

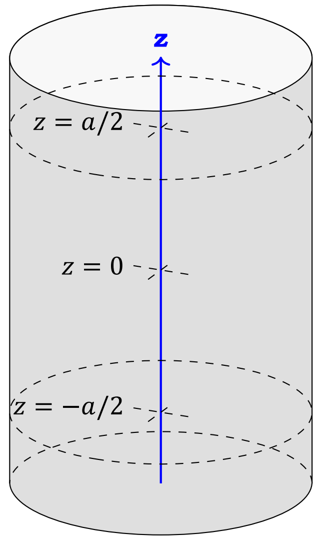

Figure 3.3: Cylindrical configuration used in the simulation, the dashed circle are the locations of the coils as described in Figure 3.1. The gray area describes the location where the boundary element method will be performed on.

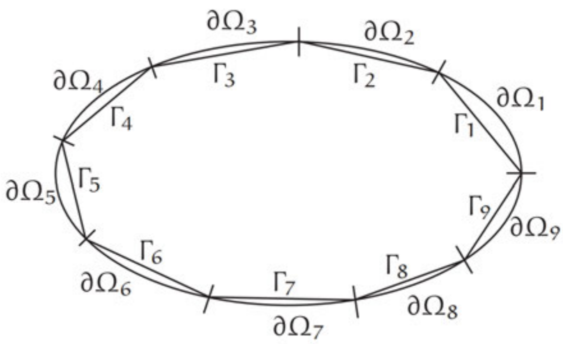

Figure 3.4: Top view of the cylinder showing how between nodes a cylinder is discretized. Where $\partial\Omega$ denotes a part of the original cylinder and Γ denotes a discretized element. Image from [23].

The analytical- and simulation results

As discussed previously in this section, the analytical results can be determined along the center line of the coils. For these simulations we take the radius of the loop and the distance between the coil as $a = 0.2$ meter. Such that Equation 3.1 can be written as

$$B_z(0,0,z) = \frac{0.02\mu_0 I}{\left[(0.1-z)^2 + 0.04\right]^{3/2}} + \frac{0.02\mu_0 I}{\left[(0.1+z)^2 + 0.04\right]^{3/2}}. \tag{3.2}$$

In these simulations different amount of elements and nodes are used, to see the effect of the meshing of the surface on the magnetic flux density. In Figure 3.6a the mean error determined by the difference between the analytical solution and the magnetic flux density is determined using the discretized stream function. The amount of elements increase equally in both the x- and y direction. It is clear that as the elements get smaller, the error decreases as the influence of linear spreading decreases. In Figure 3.6b the mean error is given for the cylindrical configuration as discussed before. The amount of elements increases equivalently in the radial and tangential direction. Also here the error decreases by taking smaller elements.

Looking at both figures, the error decreases more rapidly but less smoothly for the two plate scenario. This can be explained by where the nodes are placed on the discretized surface. If the original wire location is in the center between two nodes a better approximation might happen compared to a situation where the wire is close to either of the nodes. From these results it can be concluded that the

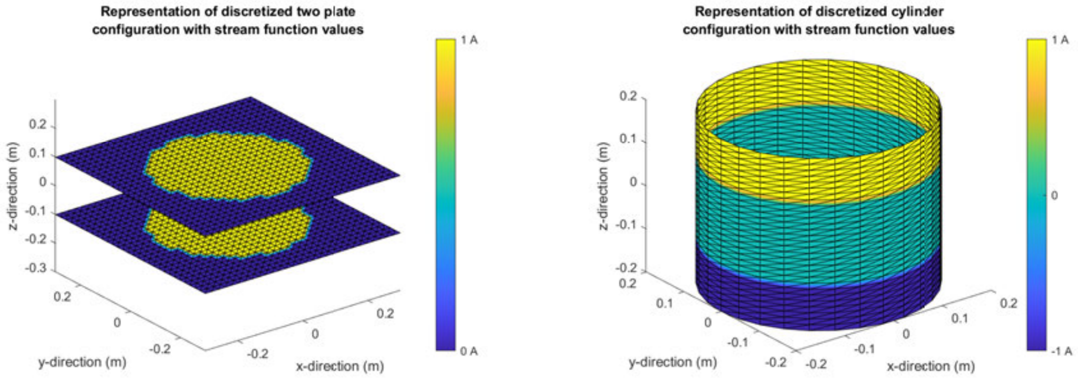

(a) Example of the stream function on the discretized surface of the two plate design.

(b) Example of the stream on the discretized surface of the cylindrical design.

Figure 3.5: Figures showing the configurations used in determining the forward problem.

discretization can result in a solution that attains the analytical solution.

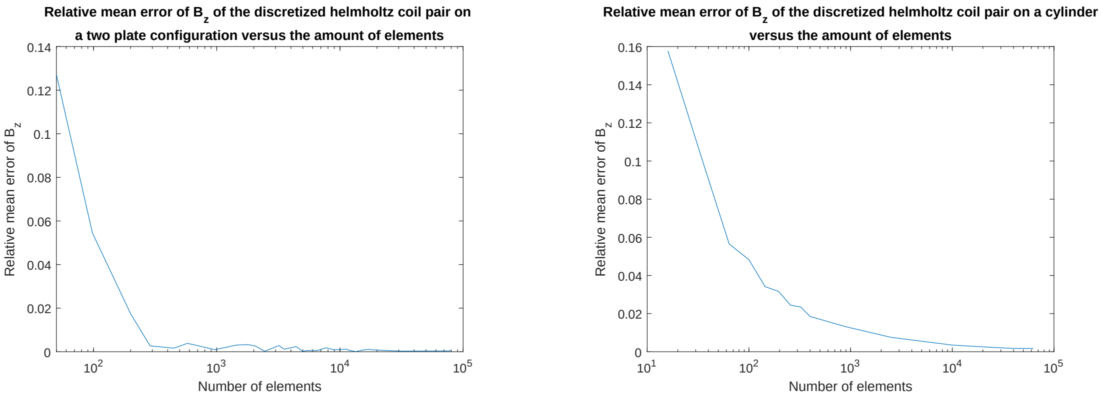

(a) Relative mean error of the magnetic flux density for the helmholtz coil discretized on two plates. The amount of elements grows equivalently in both the $x-$ and $y-$ direction.

(b) Relative mean error of the magnetic flux density for the helmholtz coil discretized on cylinder. The amount of elements grows equivalently in the radial and tangential direction.

Figure 3.6: Figures showing the mean error of the magnetic flux density versus the amount of wires for both the two-plate configuration as well as the cylinder.

3.2. Inverse Source Problem

For the inverse problem, we prescribe a certain target field and want to determine the stream function that creates this magnetic field. From the stream function we can determine a wire pattern. The magnetic flux density is this target field and the values of the target field points are in the vector $\mathbf{b}$. The unknown stream function values are located in the vector $\mathbf{x}$. The matrix formulation given in Equation 2.47 is repeated

$$\mathbf{b} = \mathbf{A}\mathbf{x}$$

and the dimensions are $\mathbf{A} \in \mathbb{R}^{N_t \times N_n}$, $\mathbf{b} \in \mathbb{R}^{N_t \times 1}$ and $\mathbf{x} \in \mathbb{R}^{1 \times N_n}$. The matrix $\mathbf{A}$ is not necessarily square nor invertible so a matrix inversion does not necessarily provide a solution. This problem is an ill-posed problem as it does not satisfy the conditions formulated by Hadamard [24]. These conditions are *existence*, *uniqueness* and *stability*. Which means the problem might not have a solution, a solution that is not unique or is unstable. An approximate solution can be formed by minimizing the least squares solution.

$$\underset{\mathbf{x}}{\text{minimize}} \, \|\mathbf{A}\mathbf{x} - \mathbf{b}\|_2^2 \tag{3.3}$$

3.2.1. Regularization

The formulation in Equation 3.3 satisfies the *existence* and *uniqueness* requirements of the Hadamard's conditions. However, the matrix $\mathbf{A}$ is close to singular and thus ill-conditioned. Leading to a situation where a small change in $\mathbf{b}$ leading to a large change in the solution. Such that the *stability* criterion is not satisfied. To stabilize the solution a regularization term is added, such that the minimization problem is

$$\underset{\mathbf{x}}{\text{minimize}} \, \|\mathbf{A}\mathbf{x} - \mathbf{b}\|_2^2 + \lambda \, \|\mathbf{L}\mathbf{x}\|_2^2 \, . \tag{3.4}$$

This minimization problem is known as the Tikhonov regularization [24]. Where λ is the regularization parameter and $\mathbf{L}$ is the regularization matrix. The regularization parameter determines the amount of regularization, while the regularization matrix can be designed for certain purposes depending on geometry and effect. Both are discussed in the subsequent sections. The problem can be written different form in which both terms are combine in one matrix, given as

$$\underset{\mathbf{x}}{\text{minimize}} \left\| \begin{pmatrix} \mathbf{A} \\ \sqrt{\lambda}\mathbf{L} \end{pmatrix} \mathbf{x} - \begin{pmatrix} \mathbf{b} \\ \mathbf{0} \end{pmatrix} \right\|_2^2 = \underset{\mathbf{x}}{\text{minimize}} \, \|\tilde{\mathbf{A}}\mathbf{x} - \tilde{\mathbf{b}}\|_2^2 \, . \tag{3.5}$$

Where the solution for $\mathbf{x}$ can be given as

$$\mathbf{x}_\lambda = \underset{\mathbf{x}}{\arg\min} \, \|\tilde{\mathbf{A}}\mathbf{x} - \tilde{\mathbf{b}}\|_2^2 \, . \tag{3.6}$$

This formulation can be used to compute an optimal $\mathbf{x}$ that satisfies Hadamard's conditions.

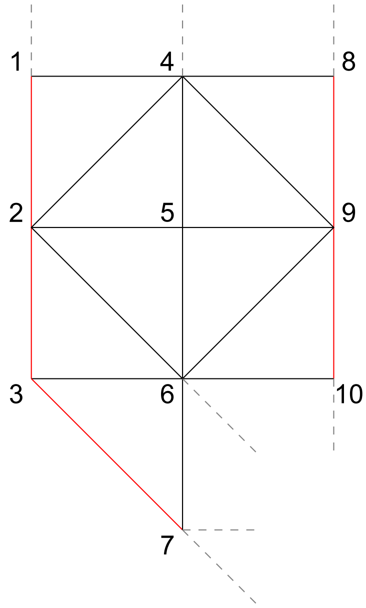

Figure 3.7: An example of a discretized surface, with at the boundaries colored red. The dashed lines implies that the domain extends in these directions. The surface is not closed and for a practical implementation, that should be the case.

3.2.2. Boundary conditions

As has been briefly touched upon in Section 2.3.2, if two nodes differ in stream function value. The difference between the two is the amount of current leaving or entering via that side. To satisfy the continuity equation as has been given in Equation 2.14 no current is allowed to leave or enter through the edges of the simulation domain. This implies that nodes at the same boundary of the domain should have the same value. In Figure 3.7 an example is given of a mesh where the boundaries are colored red. Two different boundaries exist on this domain, the nodes on each of these boundaries should have the same value. But both boundaries do not need to have the same value. The boundaries can be found by the fact that every side of a triangle that is a boundary is only part of one triangle. An algorithm has been written that uses this knowledge to find which nodes are on the boundaries and to which boundary they belong. For the example given in Figure 3.7 this means that the following conditions should hold

$$\begin{aligned} \mathbf{x}_1 = \mathbf{x}_2 = \mathbf{x}_3 = \mathbf{x}_7, \\ \mathbf{x}_8 = \mathbf{x}_9 = \mathbf{x}_{10}. \end{aligned} \tag{3.7}$$

Where $\mathbf{x}_i$ is the nodal stream function value of node i. These equations can be written as the following set of linear equations

$$\begin{aligned} \mathbf{x}_1 - \mathbf{x}_2 &= 0, \\ \mathbf{x}_2 - \mathbf{x}_3 &= 0, \\ \mathbf{x}_3 - \mathbf{x}_7 &= 0, \\ \mathbf{x}_8 - \mathbf{x}_9 &= 0 \text{ and} \\ \mathbf{x}_9 - \mathbf{x}_{10} &= 0. \end{aligned} \tag{3.8}$$

These conditions can be split into a matrix ($\mathbf{L_e}$) multiplied by the vector $\mathbf{x}$, which will satisfy the linear equations stated before. This is given as

$$\mathbf{L_e}\mathbf{x} = \mathbf{0}. \tag{3.9}$$

Where $\mathbf{L_e}$ is

$$\mathbf{L_e} = \begin{bmatrix} 1 & -1 & 0 & 0 & 0 & 0 & 0 & 0 & 0 & 0 \\ 0 & 1 & -1 & 0 & 0 & 0 & 0 & 0 & 0 & 0 \\ 0 & 0 & 1 & 0 & 0 & 0 & -1 & 0 & 0 & 0 \\ 0 & 0 & 0 & 0 & 0 & 0 & 0 & 1 & -1 & 0 \\ 0 & 0 & 0 & 0 & 0 & 0 & 0 & 0 & 1 & -1 \end{bmatrix} \tag{3.10}$$

This formulation can be added to minimization of Equation 3.4 as constraint. Such that we get

$$\begin{aligned} &\underset{\mathbf{x}}{\text{minimize}}\ ||\mathbf{Ax}-\mathbf{b}||_2^2 + \lambda\,||\mathbf{Lx}||_2^2 \\ &\text{subject to } \mathbf{L_e x} = \mathbf{0}. \end{aligned} \tag{3.11}$$

This constrained minimization is known as constrained least squares [25]. This can be solved but is relatively slow, compared to unconstrained least squares. So the formulation is changed to the unconstrained least squares as

$$\underset{\mathbf{x}}{\text{minimize}}\ ||\mathbf{Ax}-\mathbf{b}||_2^2 + \lambda\,||\mathbf{Lx}||_2^2 + \lambda_e\,||\mathbf{L_e x}||_2^2. \tag{3.12}$$

Where λ_e is the regularization parameter of these edges. λ_e should be large compared to the other factors in play, given as

$$\lambda_e \gg \lambda \frac{||\mathbf{L}||_2^2}{||\mathbf{L_e}||_2^2} \quad \text{and} \quad \lambda_e \gg \frac{||\mathbf{A}||_2^2}{||\mathbf{L_e}||_2^2}. \tag{3.13}$$

By taking λ_e very large, in the minimization it can be assumed it is a constraint. Such that to a high degree the values at the edges are constant, some very small variations between different nodes might happen. However, these variations are so small that they will not lead to any significant difference in result. The results from the unconstrained least squares are to a high degree the same as of the constrained least squares. However, the unconstrained least squares MATLAB® implementation is much faster then the constrained implementation. In the next sections the constraint is part of the minimization problem. However, for ease of reading in the formulation in the next sections this extra component is *not* shown.

3.2.3. Determining the regularization parameter

The regularization parameter λ determines the amount of regularization applied, however we do not want to regularize to much as the minimum norm solution would be less satisfied. That is, the solution differs to much from the original problem. An analytical option can be expressed but does not provide solution as it depends on $\mathbf{x}$. A method used to find the optimal λ is the L-curve [26]. In this method we compare the norm of the solution, $||\mathbf{x}_\lambda||_2$, and the residual of the problem, $||\mathbf{Ax}_\lambda - \mathbf{b}||_2$, for different values for λ. The solution norm shows us the size of the x_λ while the residual norm is shows the mean square error of this problem. This can be shown graphically as in Figure 3.8.

If we look at the vertical part of the curve. We can see that for an increasing λ the solution norm $||\mathbf{x}_\lambda||_2$ decreases rapidly while the residual norm $||\mathbf{Ax}_\lambda - \mathbf{b}||_2$ barely changes. This implies the regularization is not applied enough and the solution is unstable. If we look at the horizontal part of the curve. The solution norm $||\mathbf{x}_\lambda||_2$ changes slowly, however these small changes in the solution norm result in a big change in residual norm. Which means that the solution starts to look less like the optimal solution $\mathbf{b}$. At a certain point the regularization takes over, from $\lambda = 1$ onwards, such that the solution converges to zero. The most optimal situation happens when both solution norm and residual norm are as small as possible. This happens at the corner of the curve, denoted $\lambda = 0.1$. The L-curve is a useful tool to determine in which range one has to search for a solution, other parameters that will be in later sections can help to determine which value is actually used.

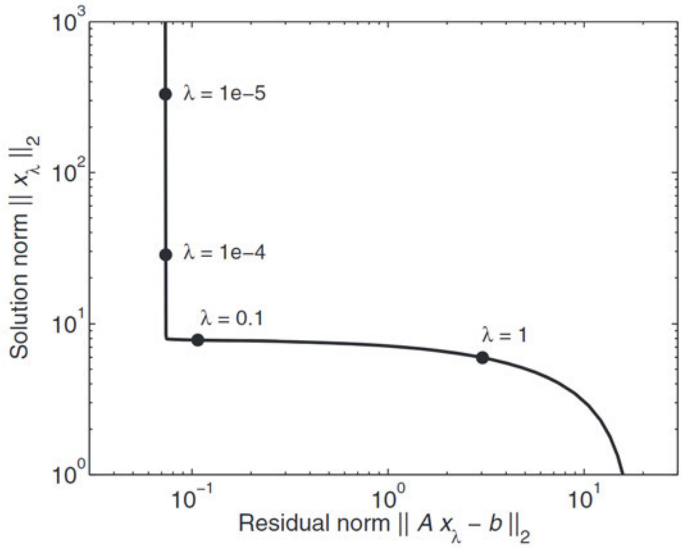

Figure 3.8: Example of a L-curve for the variable $\mathbf{x}_\lambda$ from [24, p. 73].

3.2.4. Possibility of regularization matrices

In this section different regularization matrices are discussed and tested. These are tested on the cylindrical design. The target field is a gradient in the z-direction for the x component of the magnetic flux density (B_x). The target field points form a cylinder inside the other coil, this is depicted in Figure 3.9. The target locations are spaced from $z = -0.1m$ to $z = 0.1m$ and spanned the radius of half the radius of the boundary surface. The gradient strength is set at 0.5 millitesla per meter. This is chosen for the comparison since analytical methods have found very efficient solutions to this problem, as discussed in the thesis from de Vos [15]. The first method discussed minimizes $\mathbf{x}$ itself as regularization. Followed by the second order difference operator for the cylinder. The last method shown is a method we propose to regularize for an arbitrary surface. Figures showing the stream function as well as wire patterns are shown. These wires are determined by placing wires on equally spaced stream function levels, which means that the current through the wires is the same for each of the wires. Such that by stitching the wires together a coil with only one current level can be made.

Identity Matrix as regularization matrix

At this point we have not yet determined a regularization matrix $\mathbf{L}$, in many problems an often made choice for this regularization matrix is the identity matrix

$$\mathbf{L} = \mathbf{I} \tag{3.14}$$

where $\mathbf{I}$ is the identity matrix. Such that the minimization problem is

$$\underset{\mathbf{x}}{\text{minimize}} \, \|\mathbf{Ax} - \mathbf{b}\|_2^2 + \lambda \, \|\mathbf{Ix}\|_2^2 \,. \tag{3.15}$$

The multiplication of the identity matrix $\mathbf{I}$ and the vector $\mathbf{x}$ is the vector, so the problem can be given as

$$\underset{\mathbf{x}}{\text{minimize}} \, \|\mathbf{Ax} - \mathbf{b}\|_2^2 + \lambda \, \|\mathbf{x}\|_2^2 \,. \tag{3.16}$$

The effect of this regularization method leads to decrease of the values in $\mathbf{x}$. However, there is no relation between the different values within $\mathbf{x}$. So differences between values in $\mathbf{x}$ will not change. If we rewrite this minimization problem as in Equation 3.5 we get

$$\underset{\mathbf{x}}{\text{minimize}} \left\| \begin{pmatrix} \mathbf{A} \\ \sqrt{\lambda}\mathbf{I} \end{pmatrix} \mathbf{x} - \begin{pmatrix} \mathbf{b} \\ \mathbf{0} \end{pmatrix} \right\|_2^2 = \underset{\mathbf{x}}{\text{minimize}} \, \|\tilde{\mathbf{A}}\mathbf{x} - \tilde{\mathbf{b}}\|_2^2 \,. \tag{3.17}$$

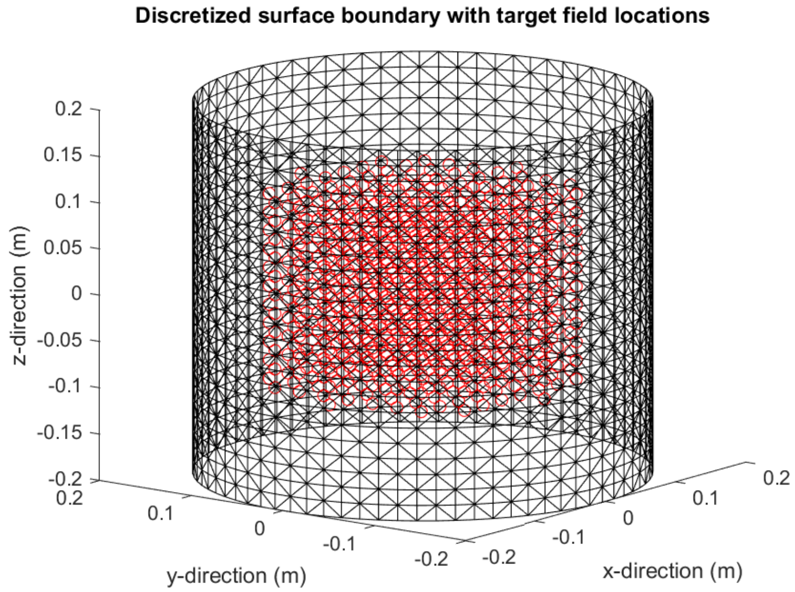

Figure 3.9: Discretized boundary surface of the cylinder with the target points shown by the red circles. The target points form a smaller cylinder.

This problem can be solved in MATLAB® using the function `lsqminnorm` [27, pp. 7530 – 7535]. If we solve the L-curve, as discussed in the previous section, and use the problem as discussed in the beginning of this section Figure 3.10 is obtained. It is clear that this L-curve, not even closely resembles an "L". This implies that throughout the decrease of the norm of $\mathbf{x}$, the target field error increases. By taking less spread-out target locations, the curve looks more like an "L", but does not as well represent a gradient field. On the right side of the curve, the norm of $\mathbf{x}$ decreases for a constant residual norm. At this point the solution no longer resembles the target field. Three values from λ have been taken along the curve, marked in Figure 3.10 with the vertical lines. Their specific distributions of the stream function on the surface of the cylinder are given in Figures 3.11a, 3.11c and 3.11e.

Also wire patterns for these regularization parameters are determined, where each of the wire patterns is created with equally spaced contours and consisting of 12 stream function levels. These are given in Figures 3.11b, 3.11d and 3.11f. As can be seen for the stream function the surface, the minimum and maximum value decreases for higher regularization parameter as expected. Because the maximum and minimum come closer together, to get the same effect on the magnetic field. The current gets more spread over the cylinder. The variations for each of the wire patterns is apparent, however. Even with a solution that is highly regularized there is a lot of small variations. Leading to small current loops, these loops make it hard to physically build the coil.

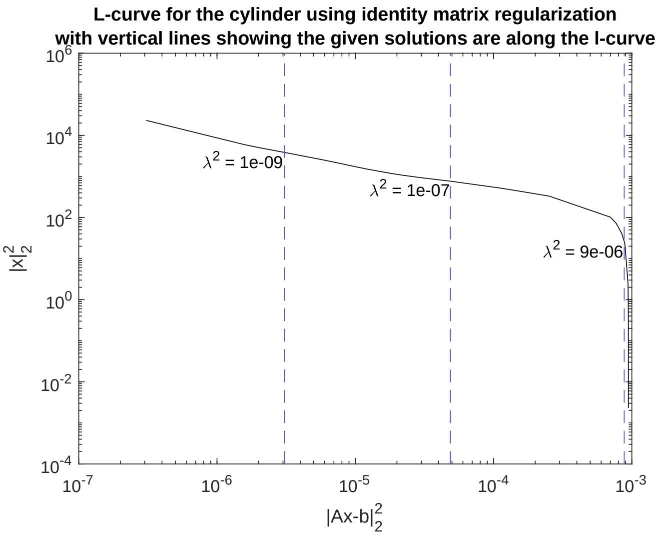

Figure 3.10: The L-curve for the discretized cylinder with regularization using the identity matrix.

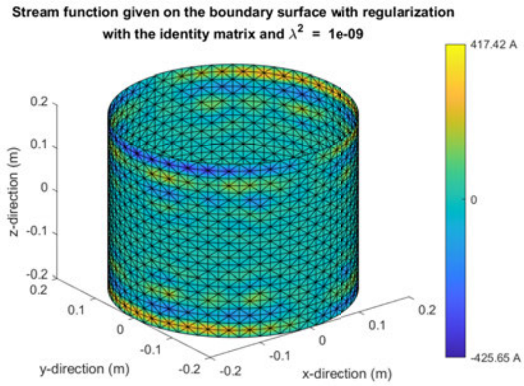

(a) Stream function on boundary surface with $\lambda^2 = 1 * 10^{-9}$.

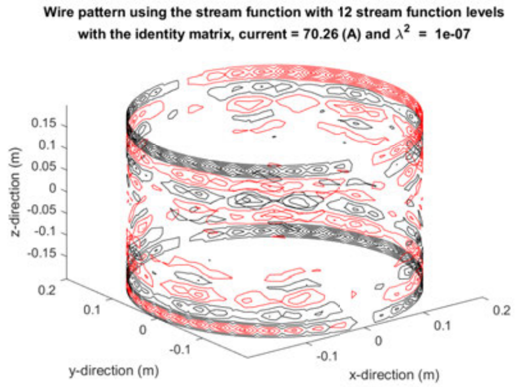

(b) Wire pattern for $\lambda^2 = 1 * 10^{-9}$.

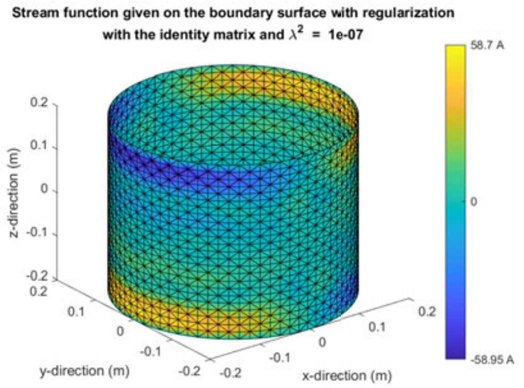

(c) Stream function on boundary surface with $\lambda^2 = 1 * 10^{-7}$.

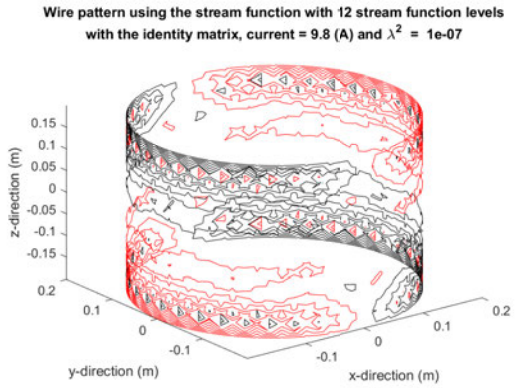

(d) Wire pattern for $\lambda^2 = 1 * 10^{-7}$.

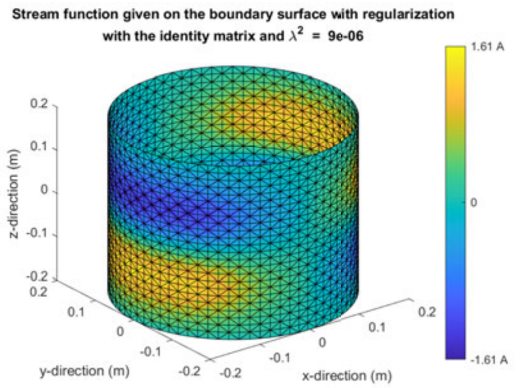

(e) Stream function on boundary surface with $\lambda^2 = 9 * 10^{-6}$.

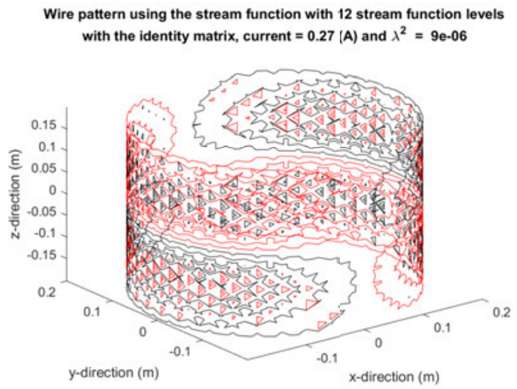

(f) Wire pattern for $\lambda^2 = 9 * 10^{-6}$.

Figure 3.11: Stream function on boundary surface and wire pattern with regularization using the identity matrix regularization for different λ's. The Wire patterns consist of 12 equally spaced stream levels.

Second order difference operator as regularization matrix

A regularization method that can be used for two dimensional surfaces is the second order difference operator [28]. This is the discretized variant of the second order derivative, if the elements of $\mathbf{x}$ form a regular grid where the element $\mathbf{x}_{i,j}$ is the ith row and the jth column of the regular grid as given in Figure 3.12.

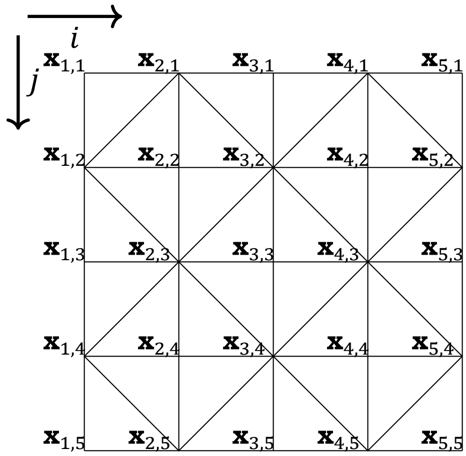

Figure 3.12: An example of a regular grid with numbered nodes for the second order difference matrix.

The second order difference operator for a specific node is given as

$$u_{i,j} = \frac{\mathbf{x}_{i+1,j} + \mathbf{x}_{i-1,j}}{2{h_1}^2} + \frac{\mathbf{x}_{i,j+1} + \mathbf{x}_{i,j-1}}{2{h_2}^2} - \mathbf{x}_{i,j} \tag{3.18}$$

where h_1 and h_2 are the grid sizes in the first- and second dimension. For boundary nodes similar expressions can be derived and can be found in Hu et al. [28]. This previous equation can be written as

$$u_{i,j} = \mathbf{l}_{i,j}^{\mathsf{T}} \mathbf{x}, \tag{3.19}$$

where $\mathbf{l}_{i,j}$ contains the weights of the second order difference operator corresponding to each of the nodes. If these vectors are stacked into a matrix for all i and j, the regularization matrix can be given as

$$\mathbf{L}_{2D} = \begin{bmatrix} \mathbf{l}_{1,1} & \mathbf{l}_{1,2} & \dots & \mathbf{l}_{1,N_n} & \mathbf{l}_{2,1} & \dots & \mathbf{l}_{N_n,N_n} \end{bmatrix}^{\mathsf{T}}. \tag{3.20}$$

To understand what this method does, let us think of the first order derivative of the stream function as the ”speed” at which the stream function changes and the second order derivative as the ”acceleration” of the stream function. To be able to generate field, there needs to be change in speed. If we would use the first order derivative as the regularization parameter, the speed would be minimized. Which leads to fluctuations a certain spots with a lot of influence. In case of the second order derivative we minimize the acceleration, this implies that speed is tended to be constant. Meaning change is allowed, however we try to keep the rate of change constant. Such that the distribution over the surface is smooth. The least squares formulation for this method is then

$$\underset{\mathbf{x}}{\text{minimize}} \left\| \begin{pmatrix} \mathbf{A} \\ \sqrt{\lambda}\mathbf{L}_{2D} \end{pmatrix} \mathbf{x} - \begin{pmatrix} \mathbf{b} \\ \mathbf{0} \end{pmatrix} \right\|_2^2$$

If we again look at the L-curve, Figure 3.13, similar behavior is seen as for the identity matrix regularization. As well as for that case, along the curve three locations have been chosen given by the vertical lines. In Figures 3.14a, 3.14c and 3.14e the stream function on the boundary surface is given. In Figures 3.14b, 3.14d and 3.14f the wire patterns determined from the stream functions are determined. Again twelve equally spaced stream function levels are used to determine these wire patterns. From the stream function figures it is obvious that the distribution gets more smoothly distributed over the complete surface, also the maximum and minimum value decrease a lot. This same result can be seen from the wire patterns.

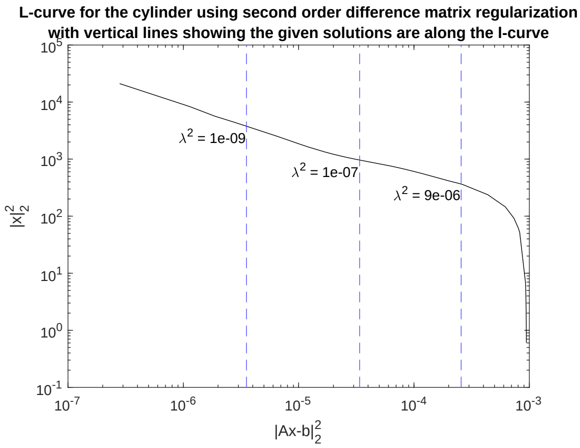

Figure 3.13: The L-curve for the discretized cylinder with regularization using the second order derivative regularization matrix.

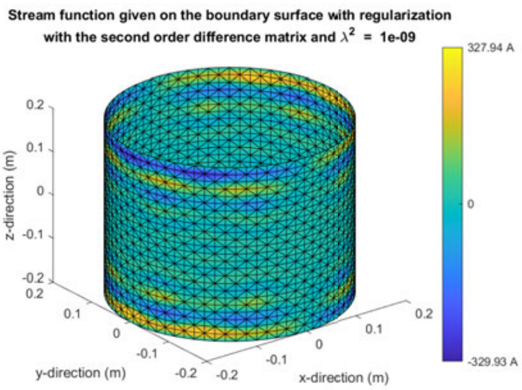

(a) Stream function on boundary surface with $\lambda^2 = 1 * 10^{-9}$.

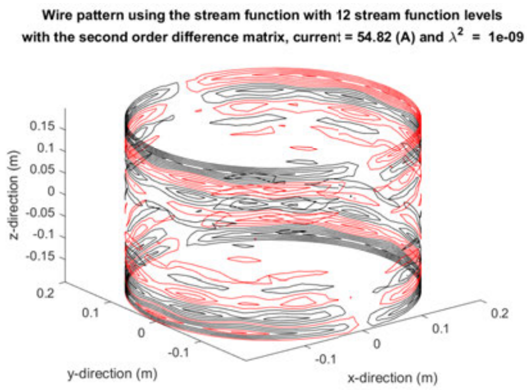

(b) Wire pattern for $\lambda^2 = 1 * 10^{-9}$.

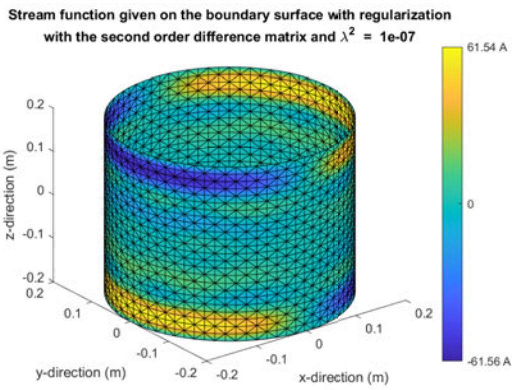

(c) Stream function on boundary surface with $\lambda^2 = 1 * 10^{-7}$.

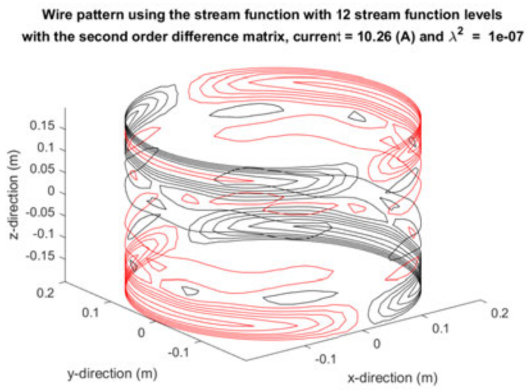

(d) Wire pattern for $\lambda^2 = 1 * 10^{-7}$.

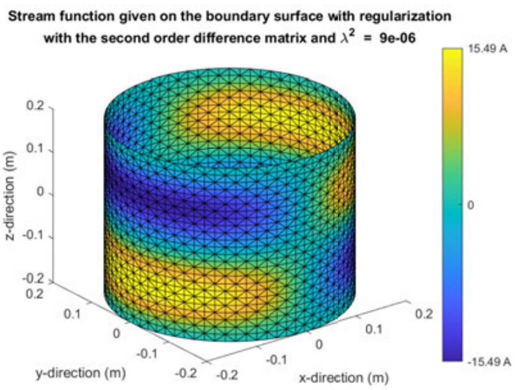

(e) Stream function on boundary surface with $\lambda^2 = 9 * 10^{-6}$.

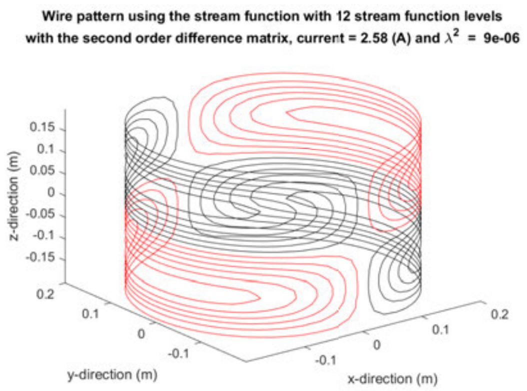

(f) Wire pattern for $\lambda^2 = 9 * 10^{-6}$.

Figure 3.14: Stream function on boundary surface and wire pattern with regularization using the second order difference matrix regularization for different λ's. The Wire patterns consist of 12 equally spaced stream levels.

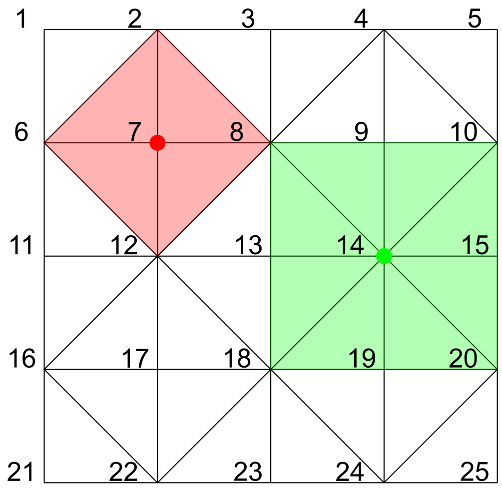

Figure 3.15: Discretized nodes with elements for the arbitrary shape method. For nodes 7 and 14 the connected nodes are given by the colored areas. Node 7 is connected to nodes; 2, 6, 8 and 12. Node 14 is connected to nodes 8, 9, 10 13, 15, 18, 19 and 20.

Regularization matrix for an arbitrary surface

The goal in this thesis is to create a method which is capable to determine the wire pattern for a certain magnetic field on an arbitrary surface. The previously discussed methods, the identity matrix and second order difference operator, both have their drawbacks. The identity matrix does not smooth the wires, so building wire patterns determined by this method will not be sufficient. The second order difference scheme is able to create smooth wires but expects the nodes to form a regular grid on a two dimensional surface. Assuming the surface is indeed two dimensional an irregular grid can be made regular by interpolation between nodes.

To get to a two dimensional model, a possibility is to use flattening algorithms. However not every three dimensional problem is developable. Which means that from the flattened version one can not bend it to the three dimensional version without overlapping or tearing [29]. In the ideal situation all areas and angles of the original three dimensional surface are preserved into the two dimensional flattened model, this is usually not possible so another metric is targeted, for example angle-preserving flattening [30] or length-preserving flattening [31]. The second order difference operator could than be used on such a two dimensional surface, however the error introduced in the flattening of the surface will lead to errors in the regularization matrix. An example of such a problem would be that in the three dimensional model, two nodes are close to each other but that is no longer the case in the flattened surface when using the angle-preserving method. Since the nodes are far apart, more change in stream function value is allowed in the regularization that is desirable. A same sort of example holds for length-preserving flattening. The best fit of flattening method very much depends on the three dimensional shape of the surface.

As we do not want to restrict to certain shapes, a method that is completely independent of shape has been developed. The regularization for node i uses all nodes node i is connected to. An example is given in Figure 3.15, where all colored nodes are connected to the node in the center. The line of the regularization matrix $\mathbf{L}_{arb}$ for node i can be written as

$$u_i = \sum_{j=1}^{N_n} \begin{cases} \frac{1}{|\mathbf{r}_j - \mathbf{r}_i|^2}(\mathbf{x}_j - \mathbf{x}_i), & \text{if } \mathbf{x}_j \in \Delta_i \\ 0, & \text{elsewhere} \end{cases}. \tag{3.21}$$

Where $\mathbf{r}_i$ and $\mathbf{r}_j$ are the locations of the ith and jth node consequently. Δ_i is a list that contains the nodes that node $\mathbf{x}_i$ is connected to. In a similar fashion as with the second order discrete difference operator the elements of the regularization matrix are related as

$$u_i = \mathbf{l}_i^{\mathsf{T}}\mathbf{x}. \tag{3.22}$$

Where the vector $\mathbf{l}_i$ contains the weights of u_i for each of the elements of $\mathbf{x}$. The regularization matrix is given as

$$\mathbf{L}_{arb} = \begin{bmatrix} \mathbf{l}_1 & \dots & \mathbf{l}_{N_n} \end{bmatrix}^{\mathsf{T}}. \tag{3.23}$$

For example, for node 7 from Figure 3.15, the nonzero elements of $\mathbf{l}_7$ are

$$\begin{aligned}
\mathbf{l}_7[2] &= \frac{1}{|\mathbf{r}_2 - \mathbf{r}_7|^2},\\
\mathbf{l}_7[6] &= \frac{1}{|\mathbf{r}_6 - \mathbf{r}_7|^2},\\
\mathbf{l}_7[7] &= -\left(\frac{1}{|\mathbf{r}_2 - \mathbf{r}_7|^2} + \frac{1}{|\mathbf{r}_6 - \mathbf{r}_7|^2} + \frac{1}{|\mathbf{r}_8 - \mathbf{r}_7|^2} + \frac{1}{|\mathbf{r}_{12} - \mathbf{r}_7|^2}\right),\\
\mathbf{l}_7[8] &= \frac{1}{|\mathbf{r}_8 - \mathbf{r}_7|^2} \quad \text{and}\\
\mathbf{l}_7[12] &= \frac{1}{|\mathbf{r}_{12} - \mathbf{r}_7|^2}.
\end{aligned} \tag{3.24}$$

The least squares regularization is given as

$$\underset{\mathbf{x}}{\text{minimize}} \left\| \begin{pmatrix} \mathbf{A} \\ \sqrt{\lambda}\mathbf{L}_{arb} \end{pmatrix} \mathbf{x} - \begin{pmatrix} \mathbf{b} \\ \mathbf{0} \end{pmatrix} \right\|_2^2.$$

This method uses the knowledge that is available for the nodes and elements. The method is based on the second order derivative method and the weights are created in a similar fashion as for the second derivative method. The arbitrary shape method behaves similar to the second order derivative method, as the weights between nodes is determined in a similar way. However, for the arbitrary shape method more nodes are connected. As can be seen, the diagonal nodes (for a regular grid) are also connected. As these nodes do lay further away from each other, their impact is present but less then the impact of the nodes in the same column or row since the weight decreases with the factor $1/R^2$.
A drawback of this developed method is that it does not work for every method of discretized surface. This is dependent on how the elements are arranged. A set of elements around a node should make as close as possible to a square or diamond shape with nodes equally spaced apart, as given in Figure 3.15. If this is not the case, it could lead to a ”pull” direction. Meaning, the regularization is applied more heavily in a certain direction then in another. Leading to a wire pattern that is skewed in this pull direction. This problem can however be resolved by choosing the elements differently, the model discretization software used in this work (Autodesk® Meshmixer™ [32]) can be set to make squares and diamond shapes from sets of elements.

For this method the L-curve is determined, which again has a similar shape as for the other two methods, with three values for λ given. The stream function distribution for these regularization parameters is given in Figure 3.17a, 3.17c and 3.17e consequently. The wire patterns using 12 equally spaced stream function levels are given in Figures 3.17b, 3.17d and 3.17f. The results from both the stream function distribution as well as the wire pattern look very similar to the results from the second order derivative method. From these results we can conclude that this method can be used to find a stable solution that can be build for an arbitrary shape. In the next chapter, this method will be used to determine an RF coil to image the brain.

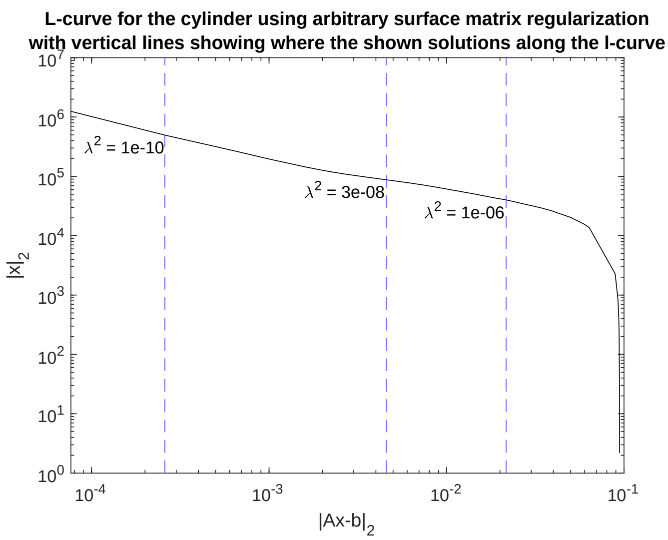

Figure 3.16: The L-curve for the discretized cylinder with regularization using the arbitrary shape regularization matrix.

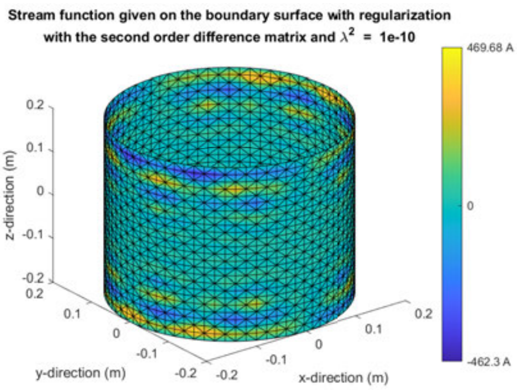

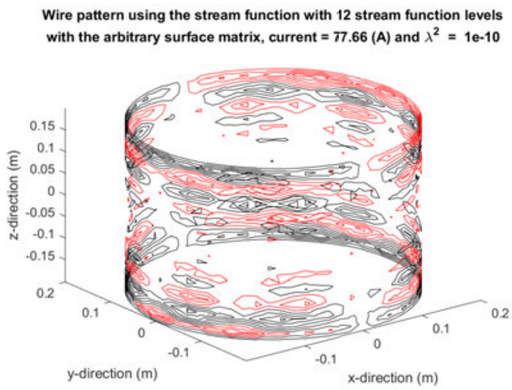

(a) Stream function on boundary surface with $\lambda^2 = 1 * 10^{-10}$.

(b) Wire pattern for $\lambda^2 = 1 * 10^{-10}$.

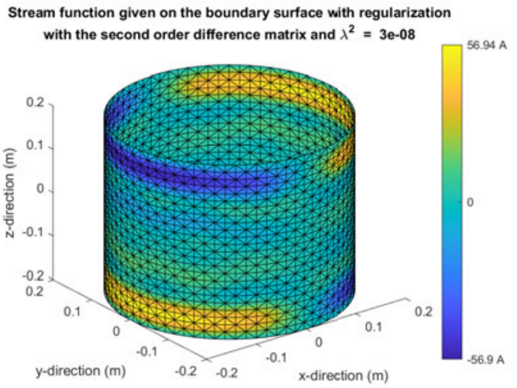

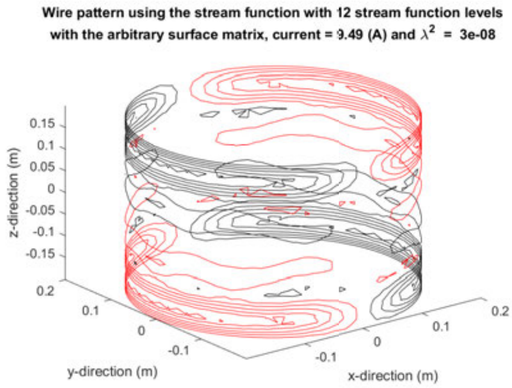

(c) Stream function on boundary surface with $\lambda^2 = 3 * 10^{-8}$.

(d) Wire pattern for $\lambda^2 = 3 * 10^{-8}$.

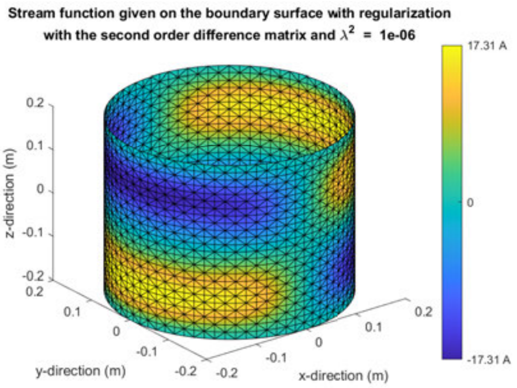

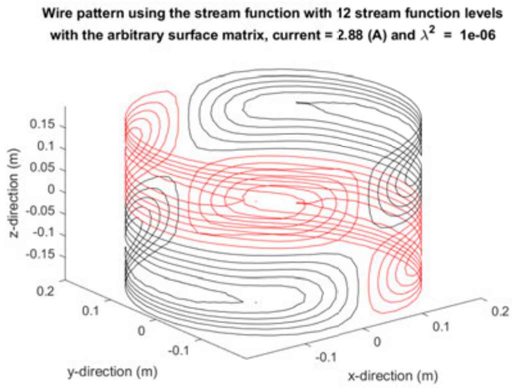

(e) Stream function on boundary surface with $\lambda^2 = 1 * 10^{-6}$.

(f) Wire pattern for $\lambda^2 = 1 * 10^{-6}$.

Figure 3.17: Stream function on boundary surface and wire pattern with regularization using the regularization matrix for arbitrary surfaces for different λ's. The wire patterns consist of 12 equally spaced stream levels.

4

Implementation

In this chapter the design process of a radiofrequency (RF) coil for the 50 millitesla Halbach-based MRI system [3] is discussed. This RF coil is meant to image an adult sized human brain. This RF coil is used as a transmitter and receiver and operates at the Larmor frequency of roughly 2.15 MHz. Since this frequency is relatively low. The quasi-static field assumptions still hold for this coil design. For more information on radiofrequency coils refer to [33].

First the design requirements are discussed in Section 4.1. Followed by the design of the surface of the RF coil and the choice of target locations in Section 4.2. In Section 4.3 the design choices made for the coil are discussed and and an analysis of the magnetic field inside the coil is given in Section 4.4. In Section 4.5 the coil construction is discussed. Lastly, in Section 4.6 the results from imaging using the designed coil are discussed and compared to another RF coil. Results are presented for both a human subject as well as a phantom.

4.1. Design requirements

The RF coil designed in this chapter is to be used for the 50.4 millitesla MRI scanner using permanent magnets. As discussed in Section 1.1.1, the main magnetic field in this scanner is in one of the transverse components with the respect to the direction of the bore. As shown in Figure 1.1 the main magnetic field B_0 is directed in the x-direction. The RF field, B_1, should be perpendicular to the main magnetic field. The RF coil built as part of this thesis uses the axial component of the magnetic field (B_z). The following design requirements are determined:

- The RF coil should have the capability to image the complete brain of a human adult.
- The RF coil should be optimized for power efficiency.
- The unloaded minimum bandwidth of the RF coil is between 20 and 25 kHz, this corresponds to a Q-factor of roughly 100.

Using these requirements, in the next section the coil surface and target locations are determined.

4.2. Design of surface and Target locations

For the first requirement we need to determine where the brain is locate. To properly image, the magnetic field created by the RF coil should be an homogeneous magnetic field. Inhomogeneity in the magnetic field can lead to undesired darker or lighter area's in the images. A deviation of 20% relative to mean magnetic flux density is deemed acceptable.
Secondly we need to know where in the head the brain is actually located. In Figure 4.1 an example of a brain is given with dimensions that have been determined using data from the Leiden University Medical Center (LUMC). As can be seen the brain covers mostly the top part of the skull. This is approximately 90 mm from the top of the skull. The brainstem is located lower, seen from the top of the skull, into the head and further to the back of the head. Going as deep as 150 mm deep about 90 mm from the back of the head.

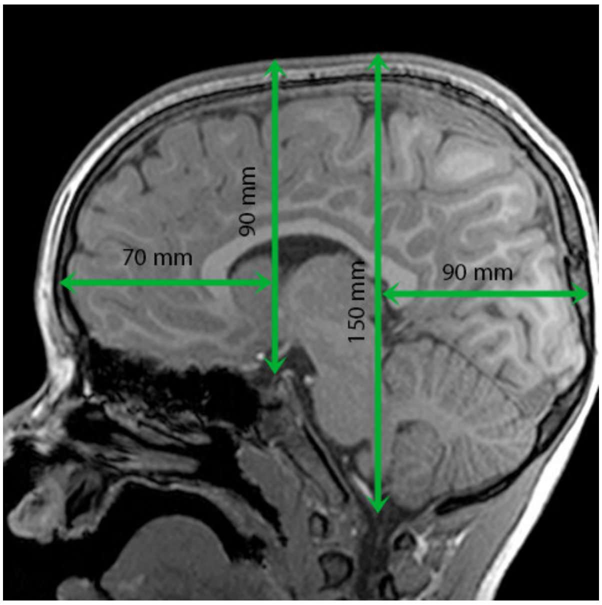

Figure 4.1: Sagittal slice through the human head showing the brain, dimensions have been added for which the coil is designed. Figure without dimensions from [34].

Using the information presented above a surface was created, an helmet-like design has been made using Solidworks® [35]. This design is based on a coil that was already built by Tom O'Reilly, this coil is used as a reference during the MR imaging. This design is chosen since a high filling factor is desirable for higher power efficiency. The coil should be as close to the sample as possible for the highest possible filling factor. On the backside of the head an extension into the neck has been made. Which is slightly tapered inwards, to follow the heads curvature. This leads to the design shown in Figure 4.2.

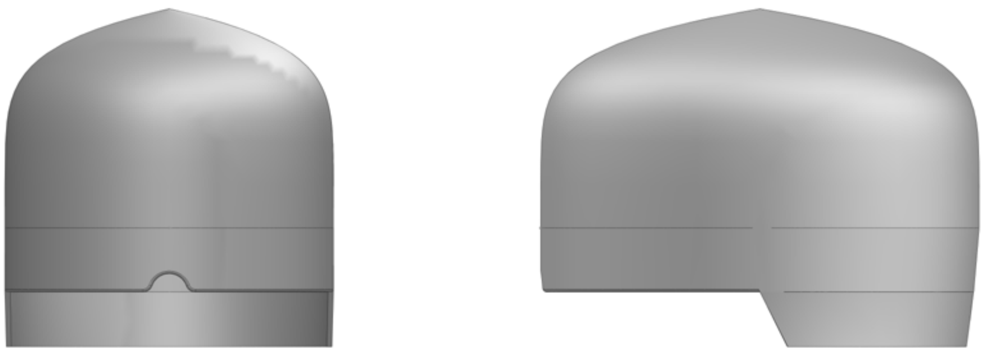

Figure 4.2: Solidworks model on which the surface for the boundary element method is based on.

From this model, the outer layer is separated and discretized to create a model that can be used for the boundary element method. An extensive explanation of how this can be done is given in Appendix A, this appendix is a manual consisting the procedure of creating a coil from the boundary element method. In Figure 4.3a the discretized outer layer is shown. The reference frame is the same reference frame as that of the MRI main magnet as seen in Figure 1.1.1. The discretized grid contains of 3413 nodes and 6739 elements.

Using the information about where the brain is located within the head, the target field locations are determined. These are shown in Figure 4.3b, represented by the red circles. The target points fill the helmet from about one centimeter inwards from the boundary as well as the complete back of the helmet to cover the brain stem. These target locations summed up combines to 4020 locations. The target locations should be equally spaced in the target volume. Otherwise certain part of the volume becomes more prevalent over other parts of the volume. This can lead to an undesired error distribution.

The amount of target locations can be increased, however results do not improve with more locations than sufficient to describe the target field volume while simulating times do increase. For an increase of target field locations to be useful, the amount of nodes and triangle should also be increased. However, this also would further increase the computation time. Smaller meshing would also create smaller wire segments and thus smaller variations. That would not necessarily make the coil more easily buildable.

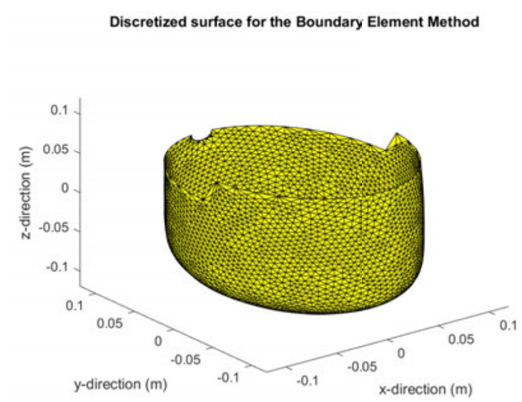

(a) The discretized coil surface of the radio-frequency coil.

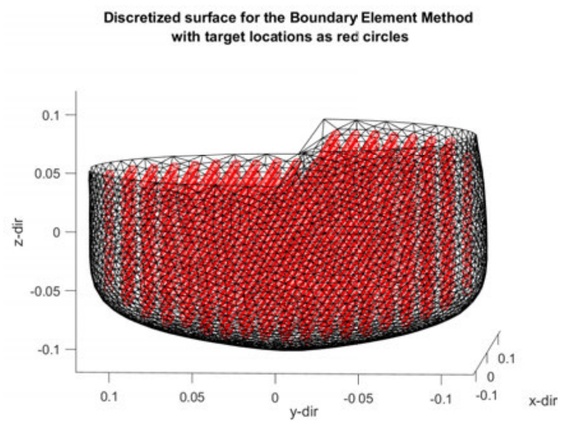

(b) The discretized coil surface of the RF coil given by the elements. The red circles describe the target field locations.

Figure 4.3: Discretized coil surface with and without target field locations given.

4.3. Determining the wire pattern

With the boundary surface and the target field points determined, the wire patterns can be obtained. Using the requirements discussed in Section 4.1, an analysis is done to determine the regularization parameter and the amount of wires used for the RF coil. The regularization matrix is determined using the method for arbitrary surfaces as discussed in Section 3.2.4. Using the different regularization parameters the L-curve can be created. The L-curve is given in Figure 4.4. As can be seen, there is not such a sharp corner where there is a clear transition between the two different parts of the curve. However, it is clear that we want a homogeneous field with a stable solution. For the most homogeneous field with a stable wire pattern, we want to be as close as possible to the corner in the L-curve. This is shown by the left vertical dashed line in Figure 4.4. The solutions along the horizontal part are taken as possible solutions as well, given by the right vertical dashed line. For the proposed configuration this is the region within the limits $\lambda^2 = 5 \times 10^{-9}$ and $\lambda^2 = 7 \times 10^{-6}$. The further to the left along the curve, there is less error introduced in the magnetic field.

The second criterion states that the coil should be as power efficient as possible. To determine the power efficiency of each of the designs, we have sought-after a metric that is independent of the amount of turns. This metric has been defined as

$$S = \frac{B_z}{IR} \quad (T/V). \tag{4.1}$$

Where I is the current through the wires and R the resistance of the coil. To solve for this metric, a wire pattern needs to be determined because this metric depends on both the resistance and current. The resistance can be calculated using Equation 4.2, where l is the coil length and A is the area of the wire. In Figure 4.5 the sensitivity against the amount of wires is given for one of the regularization parameters. The magnetic flux density (B_z) is determined as the mean over all target field points. As can be seen, the metric becomes constant from a certain amount of wires. This amount of wires is the amount needed to approximate the stream function. This implies that if the amount wires is sufficient to approximate the stream function, the metric is shows behavior of the stream function. This metric

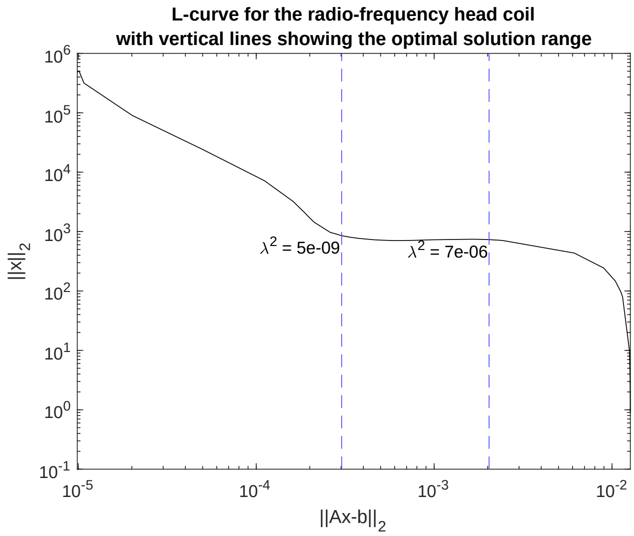

Figure 4.4: L-curve of regularization for the radio-frequency head coil

might not say much about the actual coil power usage of each of the wire patterns. However, it does make it possible to compare the different stream function designs from the regularization.

$$R = \frac{\rho l}{A} \quad (\Omega) \tag{4.2}$$

With a sufficient amount of wires, Figure 4.6 has been determined, here we can see the metric over the different regularization parameters. The metric is maximized for values of λ that are high, which by looking to the L-curve, will give a very inhomogeneous magnetic field. This can be explained by the effect that the "hard to satisfy" target locations are dropped for higher values of λ. These target locations are located near the open side of the model. For these higher λ's the current becomes relatively small such that this higher efficiency is attained.

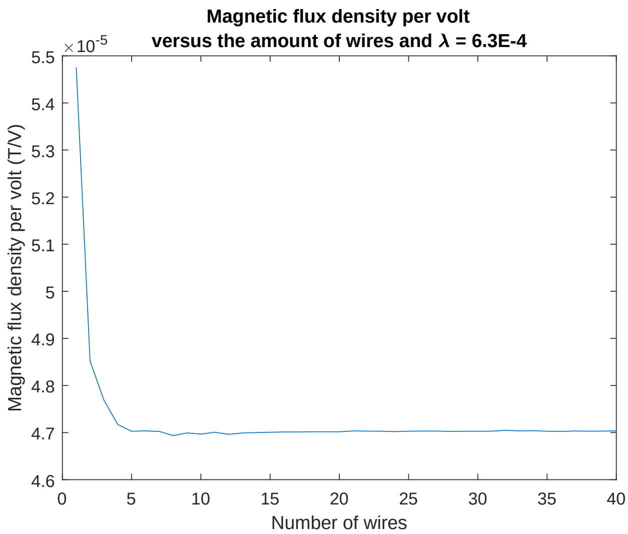

Figure 4.5: The Coil power metric plotted against the number of wires used for the wire pattern for regularization parameter $\lambda = 6.3 \times 10^{-4}$

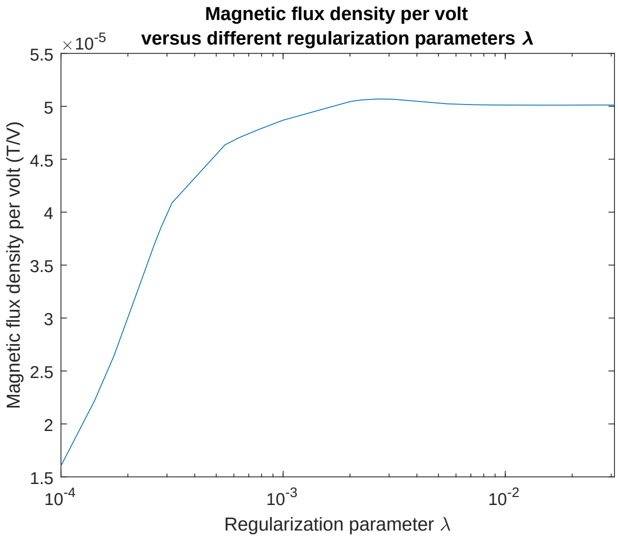

Figure 4.6: Coil power metric plotted against the different regularization parameters for 25 wires in each of the cases.

The bandwidth of a coil is determined by the operating frequency and the Q-factor of the coil. The Bandwidth is given by

$$BW = \frac{\omega}{Q} \quad (rad/s), \tag{4.3}$$

where the Q-factor is given by

$$Q = \frac{\omega L}{R} = \frac{2\pi f L}{R}. \tag{4.4}$$

Where L is the inductance, R is the resistance, ω is the angular precession frequency and f the Larmor frequency. The inductance can be calculated and discretized as [36]

$$L = \frac{\mu_0}{4\pi} \oint_l \oint_l \frac{\mathrm{d}\mathbf{l}_1 \cdot \mathrm{d}\mathbf{l}_2}{\|\mathbf{r}_1 - \mathbf{r}_2\|_2}, \tag{4.5}$$

$$L \approx \frac{\mu_0}{4\pi} \sum_{n=1}^{N_{seg}} \sum_{m=1}^{N_{seg}} \frac{(\mathbf{r}[n] - \mathbf{r}[n-1]) \cdot (\mathbf{r}[m] - \mathbf{r}[m-1])}{\|\mathbf{r}[n] - \mathbf{r}[m])\|_2}. \tag{4.6}$$

where $\mathbf{r}$ contains the locations of the wire segments, N_{seg} is the amount of segments. The resistance and inductance can be used to calculate the Q-factor and bandwidth consequently. The calculation of both the resistance and inductance is for a dc current. In higher frequencies, two effects come in to play, the skin-effect and the proximity effect [37]. The skin effect describes the charge distribution within a conductor, for increasing frequency the charge accumulates at the skin of the conductor. Leading to an increase in resistance for higher frequencies. The inductance decreases due to the skin-effect, however this effect is relatively small at high frequencies [38].

The proximity effect describes the effect of current through a conductor affecting the distribution of current in another conductor [37]. This effect is highly dependent on the shape of the conductor. This makes it difficult to calculate. So in the calculation of both the resistance and inductance the proximity effect has been ignored.

In Figure 4.7a the resistance is given versus an increasing number of wires, in Figures 4.7b and 4.8 the same is done for the inductance and quality factor. From these figures it can be seen that the resistance increases linearly with the amount of wires, while the inductance increase quadratically. Leading to a linear increase of the Q-factor with the number of wires.

However, this linear increase is not expected from literature [33, pp. 485]. The expectation is that the Q-factor should be independent of the amount of wires. For a bandwidth of 20 kilohertz, a Q-factor of about 100 is needed. However, since we neglect the proximity effect and losses in the capacitors used for tuning and matching the Q-factor is chosen higher than this 100. Higher amount of wires could also lead to other problems, such as the need of segmentation to contour wavelength effects.

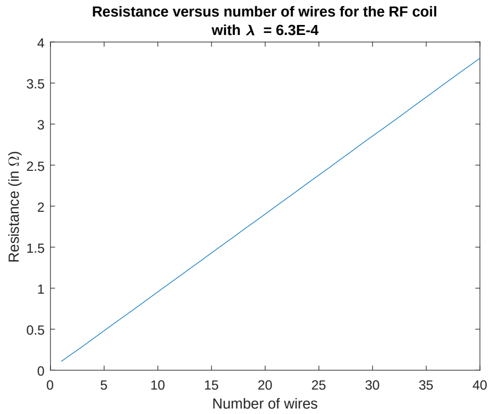

(a) Resistance versus the number of wires for $\lambda = 6.3 \times 10^{-4}$.

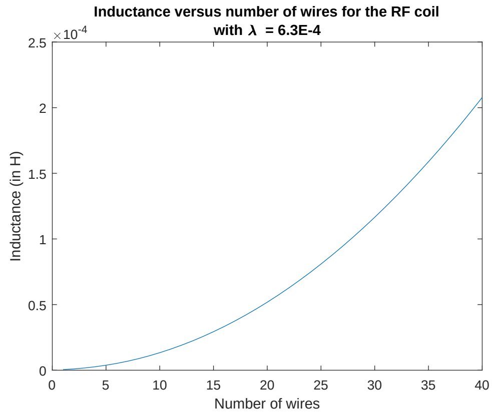

(b) Inductance versus the number of wires for $\lambda = 6.3 \times 10^{-4}$.

Figure 4.7: Resistance and Inductance versus the number of wires for $\lambda = 3 \times 10^{-4}$. In these calculations the skin-effect is included, the proximity effect is *not* included.

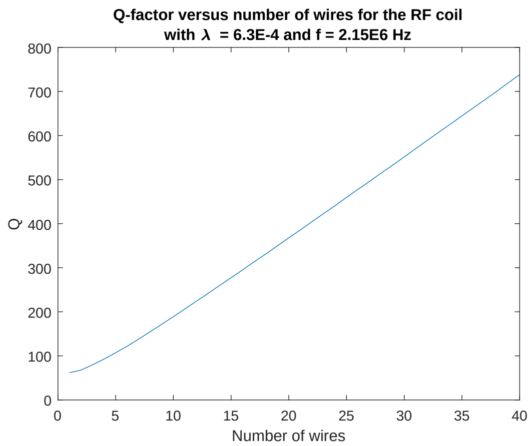

Figure 4.8: Q-factor versus the number of wires for $\lambda = 6.3 \times 10^{-4}$ and frequency of $f = 2.15$ MHz. In these calculations the skin-effect is included, the proximity effect is *not* included.

The regularization parameter is chosen at $\lambda = 6.3 \times 10^{-4}$ ($\lambda^2 = 4 \times 10^{-7}$) and the amount of wires is chosen at 16. The regularization parameter is chosen as a trade-off between the error on the magnetic flux density and the power efficiency. The amount of wires is chosen at 16, which gives a quality factor of around 300. The stream function on the coil surface is given in Figure 4.9. The amount of wires is sufficiently represent the stream function levels and has a Q-factor that fits the requirements. The wire pattern from this stream function surface is shown in Figure 4.10.

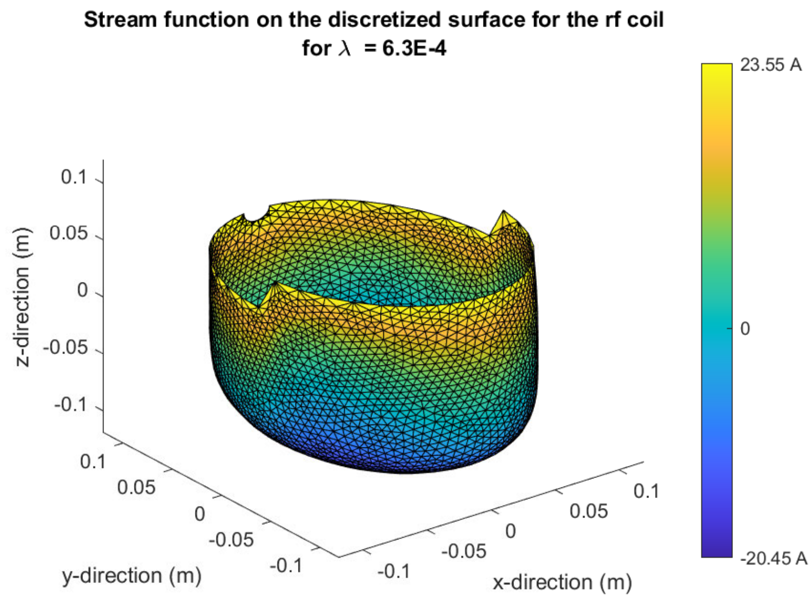

Figure 4.9: Stream Function on the surface of the rf coil for $\lambda = 6.3 \times 10^{-4}$ for a target field of 0.2 mT

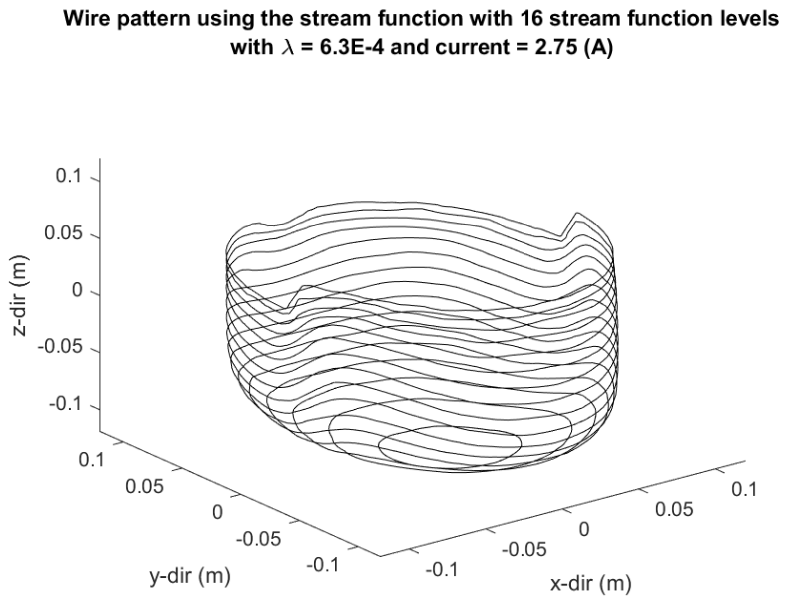

Figure 4.10: The wire pattern on the discretized surface for $\lambda = 6.3 \times 10^{-4}$ and 16 stream function levels for target field of 0.2 mT.

4.4. Simulation results of the coil design

In the previous section a choice regarding the wire pattern is discussed, we now show the corresponding magnetic flux density. In Figure 4.11 the histogram of the relative error of the magnetic flux density is given for both the error determined from the stream function values, as well as the error on the magnetic flux density determined using the wire pattern. The histogram shows the distribution of the error for all the target locations. As can be seen, the error from the stream function distribution has a higher peak near zero and the error distribution is smaller. The average is thus smaller. The wire pattern has lower but wider distribution, which in turn means that the errors differ a bit more in comparison to the error from the stream function.

In Figure 4.12 slices of the magnetic flux density within and outside the coil are given. Figures 4.12a, 4.12c and 4.12e are sagittal (yz-plane) slices. Figures 4.12b, 4.12d and 4.12f are transverse slices (xy-plane). Looking at the sagittal slices, it can be seen that the magnetic flux density is homogeneous within the coil and reaches to the edge of the coil with minimal deterioration. The majority of the inside of the coil is within 10% homogeneity. However, 3 main hotspots can be seen. These hotspots do not form a problem in imaging the brain, as they are expected to either be not severe enough or not lay in a part of the volume where the brain situated. The two first transverse slices reinforce this conclusion of an homogeneous field. The last slice, Figure 4.12f, is past the end of the front side of the coil, where y is positive, and the magnetic flux density is clearly deteriorated. However, on the back side of the coil where the coil still substantial magnitude is present. Such that we expect that imaging should still be possible here.

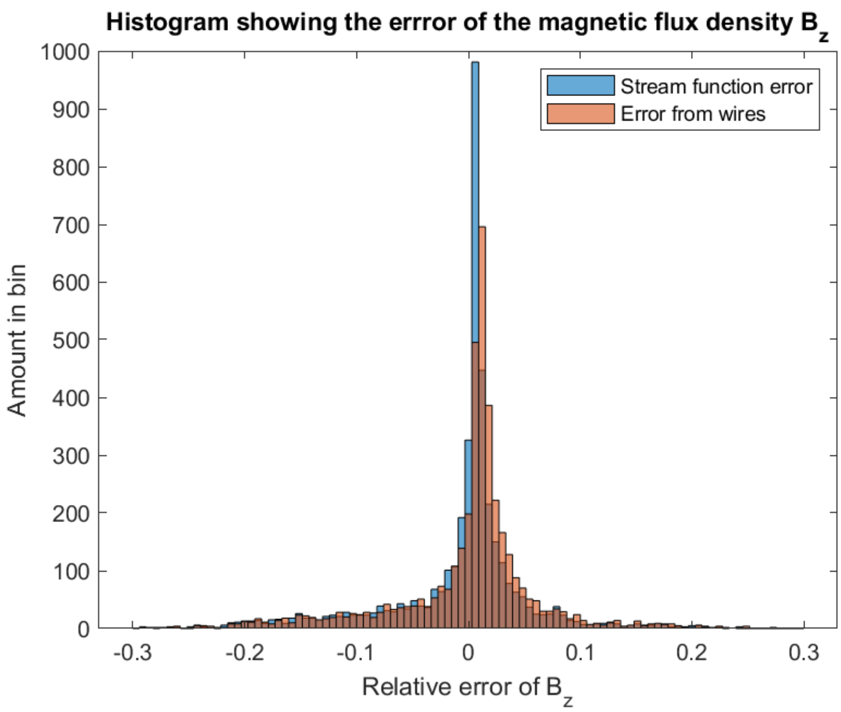

Figure 4.11: Histogram showing the error of the magnetic flux density for all target locations determined from the stream function values as well as the error on the magnetic flux density determined using the wire pattern.

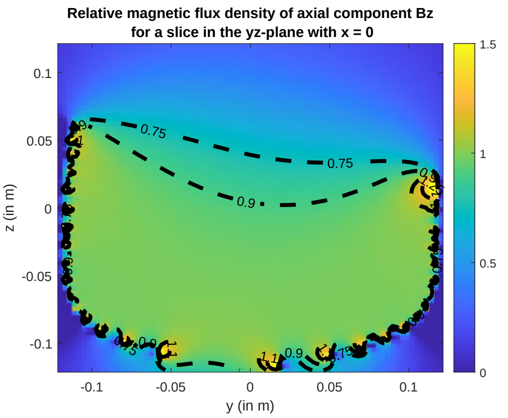

(a) Sagittal slice in the yz-plane through the rf head coil located at $x = 0$ meter for the magnetic flux density component B_z.

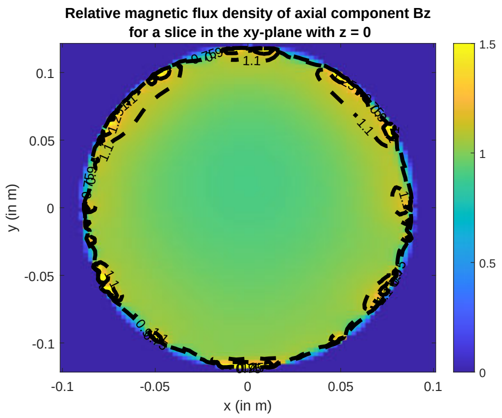

(b) Transverse slice in the xy-plane through the rf head coil located at $z = 0$ meter for the magnetic flux density component B_z.

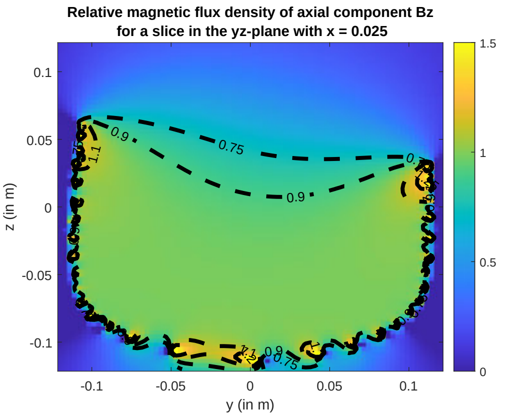

(c) Sagittal slice in the yz-plane through the rf head coil located at $x = 25$ millimeter for the magnetic flux density component B_z.

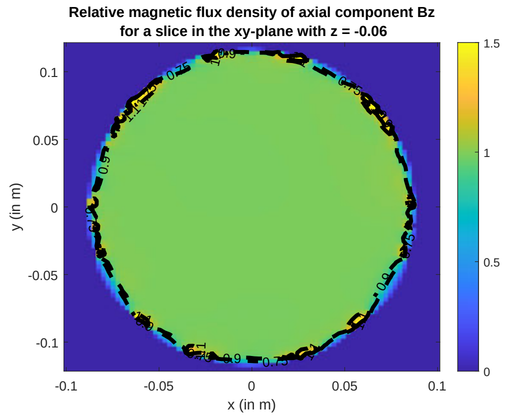

(d) Transverse slice in the xy-plane through the rf head coil located at $z = 60$ millimeter for the magnetic flux density component B_z.

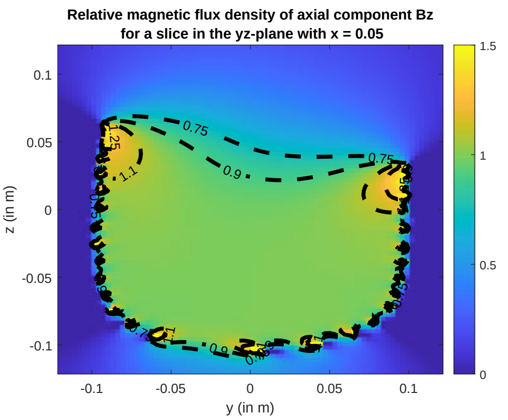

(e) Sagittal slice in the yz-plane through the rf head coil located at $x = 50$ millimeter for the magnetic flux density component B_z.

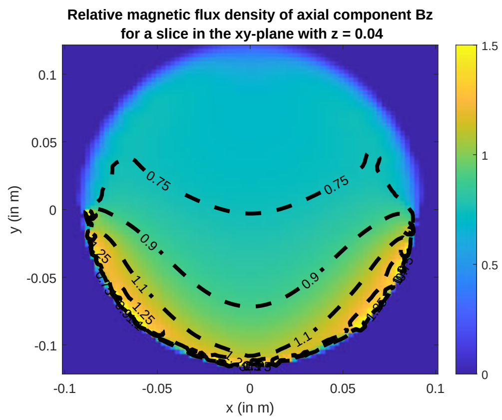

(f) Transverse slice in the xy-plane through the rf head coil located at $z = -40$ millimeter for the magnetic flux density component B_z.

Figure 4.12: Slices of the magnetic flux density component B_z relative to mean of the field over all target locations.

4.5. Coil construction

The wire pattern determined in the previous sections still consists of separate wires. Because equal current runs through each of the individual loops, the wires can be stitched together, the stitched wire pattern is given in Figure 4.13. The difference in error distribution is given as an histogram in Figure 4.14. It is clear that some of the smallest errors are increased, however it still closely resembles the error distribution before stitching as well as the error distribution of the stream function.

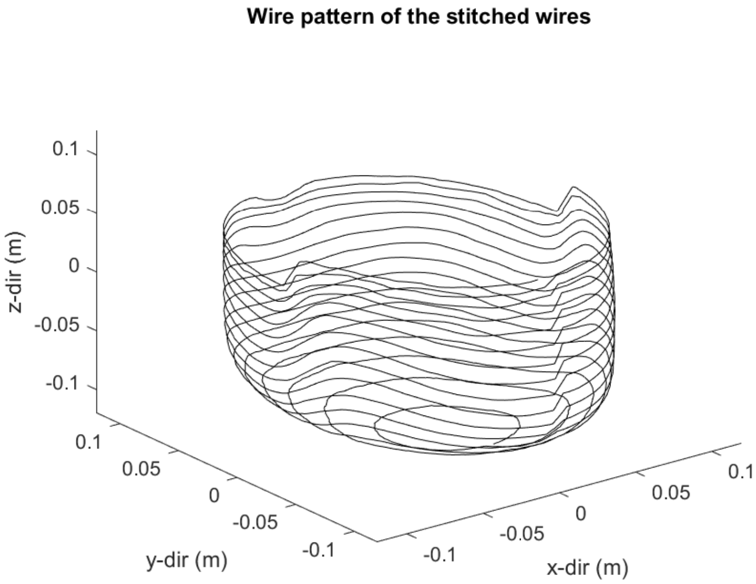

Figure 4.13: The stitched wire pattern deduced from the separate wires.

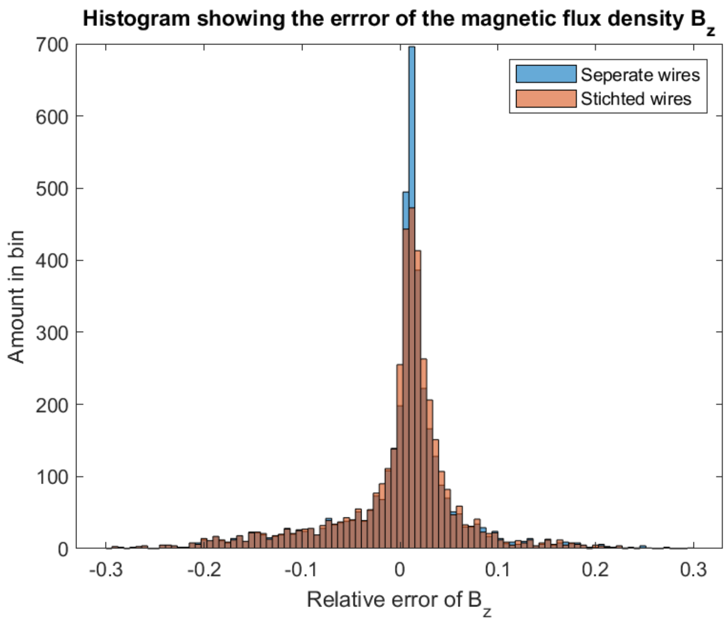

Figure 4.14: Histogram showing the relative error of the magnetic flux density for all target locations for the unstitched- and stitched wires.

The wire positions are used to create slots in the Solidworks model, in these grooves the copper wire can be placed. An extensive explanation of this procedure is given in Appendix A. Figure 4.15 shows the carved out surface as it looks like in Solidworks and Figure 4.16 shows the 3d printed result.

The coil is wired using enamel-coated copper wire, such that the coil can be touched without touching the conducting copper wire. In the wiring process copper wire with a radius of 0.4 millimeter is used. The wired coil is shown in Figure 4.17, two rests on the backside of the coil are added to make sure the coil is in the correct position within the bore.

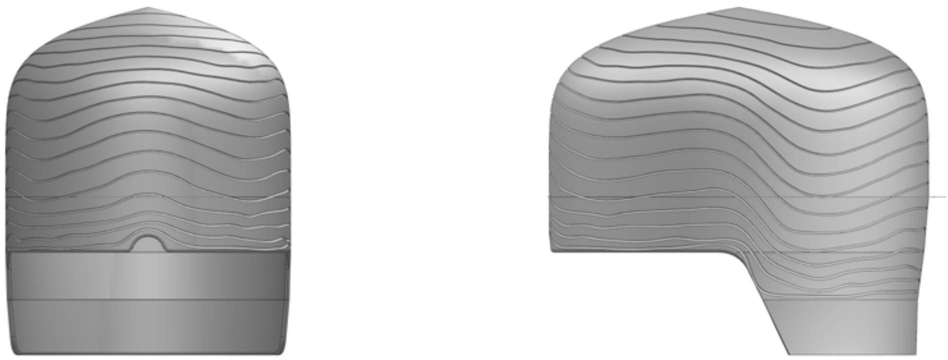

Figure 4.15: Solidworks model with the slots added to wire the coil.

(a) Frontside of the 3d printed headcoil.

(b) Backside of the 3d printed headcoil.

Figure 4.16: Front- and backside of the 3d printed headcoil.

(a) Frontside of the 3d printed headcoil.

(b) Side view of the 3d printed headcoil.

Figure 4.17: Frontside and side view of the 3d printed headcoil with wires.

4.5.1. Coil matching and tuning

To image using the head coil, the coil needs to be tuned to the right frequency and matched to 50 ohm. This is done using a tuning and matching circuit, this circuit is depicted in Figure 4.18. This tuning- and matching circuit is known as a parallel-tuned series-matched circuit [33]. This circuit adds additional loses to the Q-factor and thus influences the imaging bandwidth and image quality.

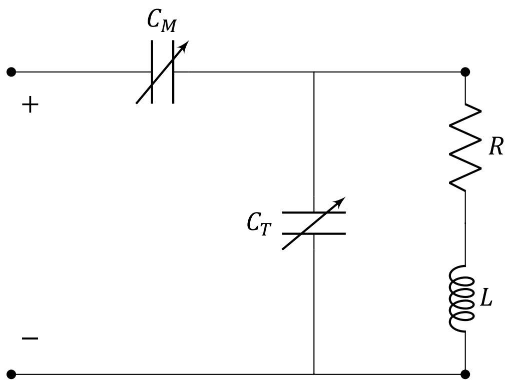

Figure 4.18: Tuning and Matching used for the rf coil. Where the amplifier is connected to the open terminals. The coil is described by the resistance and inductance. The tuning is done using the tuning capacitor C_T and the matching using the matching capacitor C_M

4.6. Imaging Results

The coil designed in this thesis has been used to image an adult male subject. These results are compared to a coil that has been created by the LUMC which has been used in the past to image the human brain. This coil designed by T. O'Reilly at the LUMC is used as reference to compare with. The brain of a human subject as well as a phantom have been imaged. The phantom can be placed further into the bore and is closer to the middle of the bore, so the field inhomogeneities at the end of the bore do not affect the imaging. In Table 4.1 the acquisition parameters of the four measurements are given.

Figure 4.19: Two coils used in imaging side by side. The coil on the left side is designed by T. O'Reilly, on the right side is the coil designed using the Boundary Element Method.

Table 4.1: Acquisition parameters of the two coils used in the imaging. Unloaded values are with no human or phantom inside the coil.

Coil	Subject	Q unloaded	Q loaded	Bandwidth unloaded (kHz)	Bandwidth loaded (kHz)	90 ° Flip Angle Power (dB)
BEM	Human	55	47	39	46	-14.25
Reference	Human	N/A	61	N/A	35	-18.58
BEM	Phantom	55	56	39	38	-16.18
Reference	Phantom	N/A	108	N/A	20	-17.36

From these parameters it is clear that the Q-factor is much lower than the Q-factor determined in Section 4.3. The Q-factor for an unloaded coil is about six times smaller than the simulations suggested. However, as earlier stated effects as the proximity effect have been neglected. The flip angle power needed is also higher for the BEM coil design, however this is expected since the imaging volume is also bigger than the imaging volume of the reference coil.
The resistance and inductance have also been calculated for the BEM designed coil. These measurement are done at low frequency so these do not describe the high frequency impact on the parameters. In Table 4.2 this information is shown. The figures do differ substantially, this is expected to be partly due to the extra wire that was still attached during these measurements. However, these figures are much close together than the difference in Q that is observed between the calculation and measurements. From this data it is clear that at high frequencies it is hard to determine the expected quality factor using the current simulations.

Table 4.2: Calculated and Measured values of both the Resistance and Inductance for the coil designed using BEM.

Method	Resistance (Ω)	Inductance (μH)
Calculated	0.34	33.5
Measured	0.4	38.9

4.6.1. Brain Imaging

The sagittal slices of the human subject for both coils are given in Figure 4.20. These image locations are chosen similarly as the sagittal slices in Figures 4.12a, 4.12c and 4.12e. That is, Figures 4.20a and 4.20b both are sagittal slices at the center ($x = 0$ meter). Figures 4.20c and 4.20d are both slices 24 millimeter from the center ($x = 0.024$ meter), while Figures 4.20e and 4.20f are slices at 48 millimeter from the center ($x = 0.048$ meter). From the figures, it is clear the SNR is lower for the BEM designed coil compared to the reference coil. This can be explained by the lower Q-factor and wider imaging bandwidth, leading to an increase in noise being picked up.

From these images it is hard to determine if more of the human brain can be imaged as other field inhomogeneities influence the image quality. At the front side of the head, which is the bottom of the images, some more signal seems to be present. For both coils it is clear that at the backside of the head near the neck, there is signal loss. This is due to inhomogeneities in either the main magnetic field or gradient coils at this location. The subject has a short neck, so imaging at a location within the bore where these field homogeneities are not present is not possible.

In Figure 4.21 transverse slices of the human brain are shown for both of the coils. The transverse slices at the center, Figures 4.21a and 4.21b, differ slightly from each other. The BEM designed coil has a more uniform magnetic field distribution at the bottom side of the image. However, again the SNR is worse for the BEM designed coil. These same conclusion can also be drawn from the other figures.

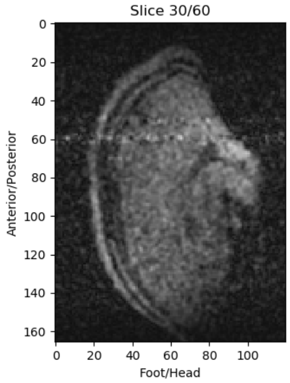

(a) Sagittal slice of the human brain at the center $x = 0$ meter using the BEM designed coil.

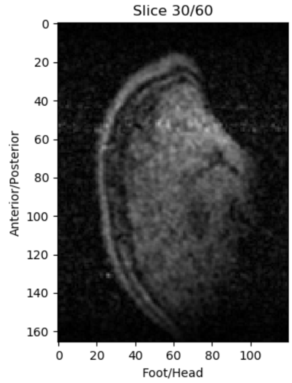

(b) Sagittal slice of the human brain at the center $x = 0$ meter using the reference coil.

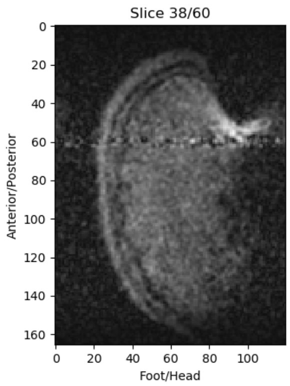

(c) Sagittal slice of the human brain at $x = 24$ millimeter using the BEM designed coil.

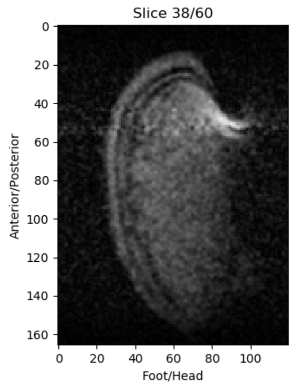

(d) Sagittal slice of the human brain at $x = 24$ millimeter using the reference coil.

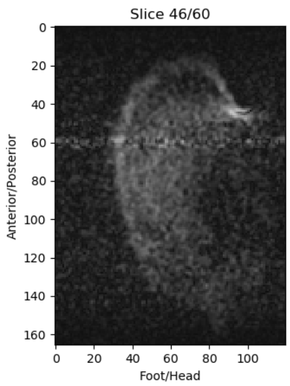

(e) Sagittal slice of the human brain at $x = 48$ millimeter using the BEM designed coil.

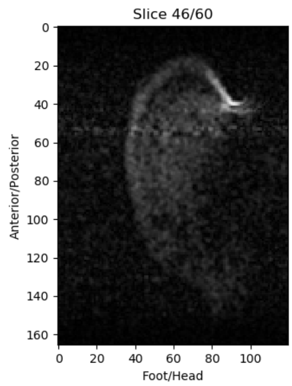

(f) Sagittal slice of the human brain at $x = 48$ millimeter using the reference coil.

Figure 4.20: Sagittal slices for both the BEM designed coil (left) and the reference coil (right) using the human subject. Images are acquired using a Turbo Spin Echo sequence. Acquisition parameters: 180 x 180 x 249, data matrix: 60(x) x 120(z) x 166(y), TR/TE: 400/19ms, echo train length: 5, scan duration: 9 min 36s. The x- and y-axis in the figures are in pixels. The pixel size is 1.5 x 1.5 millimeter for both measurements.

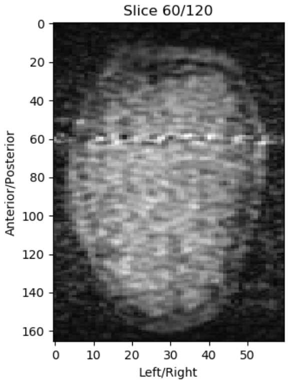

(a) Transverse slice of the human brain at the center $z = 0$ meter using the BEM designed coil.

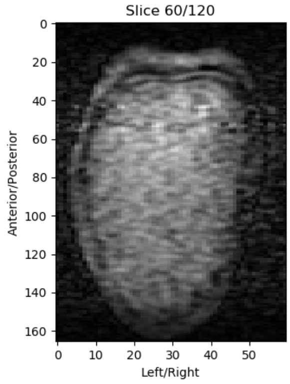

(b) Transverse slice of the human brain at the center $z = 0$ meter using the reference coil.

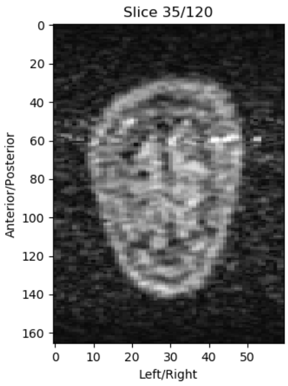

(c) Transverse slice of the human brain at $z = -37.5$ millimeter using the BEM designed coil.

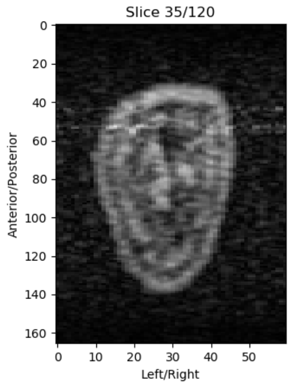

(d) Transverse slice of the human brain at $z = -37.5$ millimeter using the reference coil.

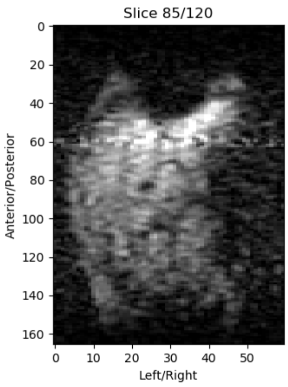

(e) Transverse slice of the human brain at $z = 37.5$ millimeter using the BEM designed coil.

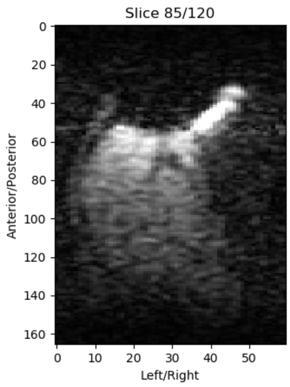

(f) Transverse slice of the human brain at $z = 37.5$ millimeter using the reference coil.

Figure 4.21: Transverse slices for both the BEM designed coil and the reference coil using the human subject. Images are acquired using a Turbo Spin Echo sequence. Acquisition parameters: 180 x 180 x 249, data matrix: 60(x) x 120(z) x 166(y), TR/TE: 400/19ms, echo train length: 5, scan duration: 9 min 36s. The x- and y-axis in the figures are in pixels. The pixel size is 3.0 x 1.5 millimeter for both measurements.

4.6.2. Phantom Imaging

As a human cannot be pushed further into the bore, a phantom has been used to image at the center of the bore where the artifacts created by the main magnetic field and gradient field are less present. For the imaging a head phantom is used filled with water H_2O and sodium chloride $NaCl$. In Figure 4.22 the head phantom is shown. It is important to note that the head phantom is not completely filled, such that the top side, where the nose is located, is not filled with water during the acquisition.

(a) Side view of the phantom used in the acquisition.

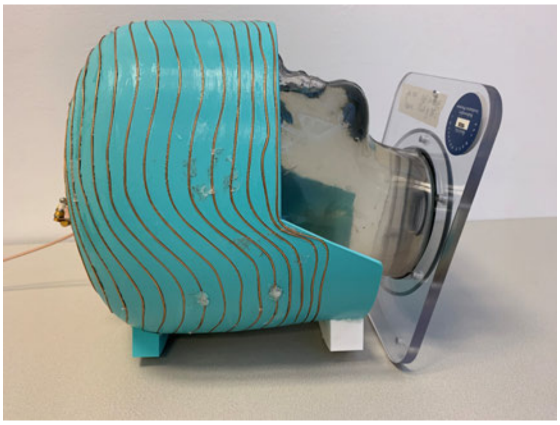

(b) Side view of the phantom and BEM head coil used in the acquisition.

Figure 4.22: Images of the phantom used for the acquisition.

This simulation has been done for both the coil designed using the Boundary Element Method as well as the coil that was already built by Thomas O'Reilly at the LUMC. In Figure 4.23 the sagittal slices are given, the field of view on both of these images is not the same. Looking at the x-axis of the figures, it can be seen that these axis are not the same. The Field of View (FOV) in the z-direction has been made bigger for the BEM designed coil, the FOV is 210 millimeter (140 pixels) for the BEM head coil, while the FOV is 180 millimeter (120 pixels) for the reference coil.

Looking at Figure 4.23a we can see that the backside of the head (top part of image), the imaging is deeper in the neck of the phantom than at the front side of the head (bottom part of image). The difference between front and back is 20 pixels, which corresponds to 30 millimeter. Figure 4.23b shows the same slice for the reference coil. The BEM designed coil images 10 millimeter more at the front and 40 mm more at the back side of the head. The same effect can be seen in the other slices given.

Figure 4.24 shows the transverse slices for both coils using the phantom. The slice numbers are not the same, however they left and right figure do both image the same spatial location. From Figures 4.24a and 4.24b it can be seen that the sides of the coil are better imaged using the BEM designed coil. Figures 4.24c and 4.24d reinforce this view. Figures 4.24e and 4.24f show the location for which the signal of the reference coil is very little, such that the image becomes very dark. For the coil designed using the Boundary Element Method it is clear that it still possible measure at this depth into the brain.

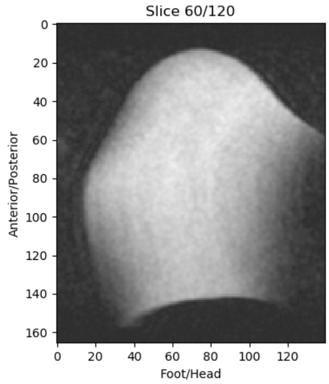

(a) Sagittal slice of the human brain at the center $x = 0$ meter using the BEM designed coil.

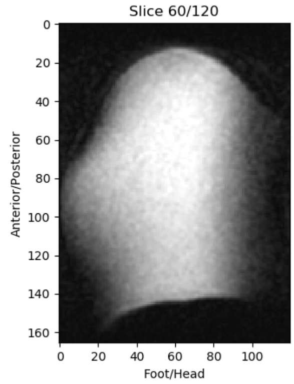

(b) Sagittal slice of the human brain at the center $x = 0$ meter using the reference coil.

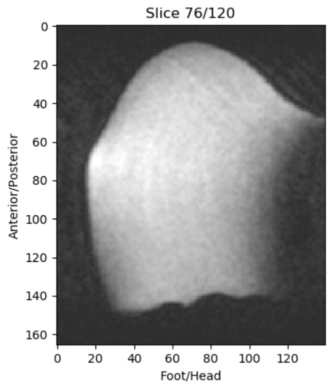

(c) Sagittal slice of the human brain at $x = 24$ millimeter using the BEM designed coil.

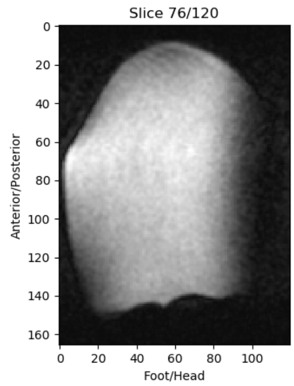

(d) Sagittal slice of the human brain at $x = 24$ millimeter using the reference coil.

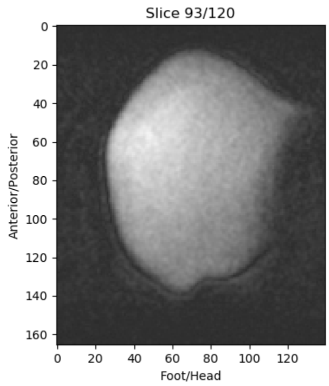

(e) Sagittal slice of the human brain at $x = 48$ millimeter using the BEM designed coil.

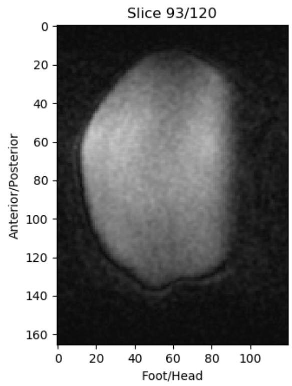

(f) Sagittal slice of the human brain at $x = 48$ millimeter using the reference coil.

Figure 4.23: Sagittal slices for both the BEM designed coil and the reference coil using the phantom. Images are acquired using a Turbo Spin Echo sequence. Acquisition parameters(left): 210 x 180 x 249, data matrix: 140(x) x 120(z) x 166(y), TR/TE: 4000/19ms, echo train length: 5, scan duration: 24 min. Acquisition parameters(right): 180 x 180 x 249, data matrix: 120(x) x 120(z) x 166(y), TR/TE: 4000/19ms, echo train length: 5, scan duration: 28 min. The x- and y-axis in the figures are in pixels. The pixel size is 1.5 x 1.5 millimeter for both measurements.

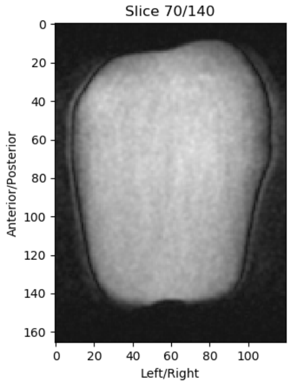

(a) Transverse slice of the human brain at the center $z = 0$ meter using the BEM designed coil.

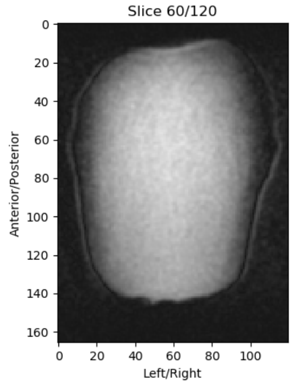

(b) Transverse slice of the human brain at the center $z = 0$ meter using the reference coil.

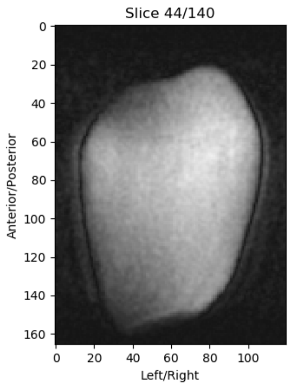

(c) Transverse slice of the human brain at $z = -39$ millimeter using the BEM designed coil.

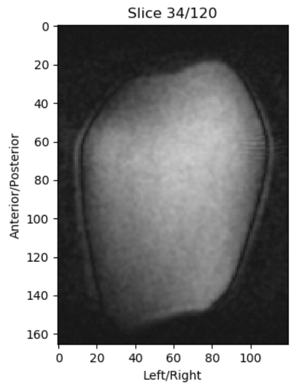

(d) Transverse slice of the human brain at $z = -39$ millimeter using the reference coil.

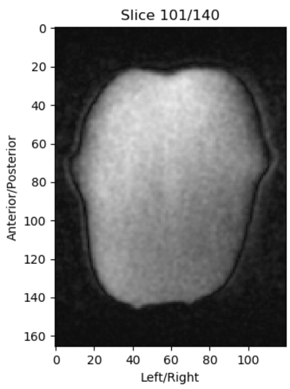

(e) Transverse slice of the human brain at $z = 39$ millimeter using the BEM designed coil.

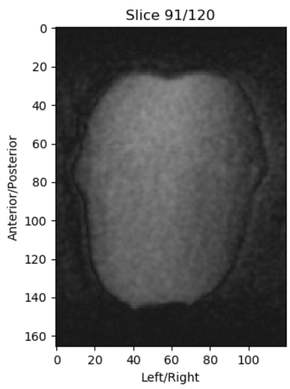

(f) Transverse slice of the human brain at $z = 39$ millimeter using the reference coil.

Figure 4.24: Transverse slices for both the BEM designed coil and the reference coil using the phantom. Images are acquired using a Turbo Spin Echo sequence. Acquisition parameters(left): 210 x 180 x 249, data matrix: 140(x) x 120(z) x 166(y), TR/TE: 4000/19ms, echo train length: 5, scan duration: 28 min. Acquisition parameters(right): 180 x 180 x 249, data matrix: 120(x) x 120(z) x 166(y), TR/TE: 4000/19ms, echo train length: 5, scan duration: 24 min. The x- and y-axis in the figures are in pixels. The pixel size is 1.5 x 1.5 millimeter for both measurements.

5
Conclusions and Recommendations

In this thesis, a method and framework have been developed to design a coil on an arbitrary surface using the boundary element method. This method allows to create coils on surfaces for which no analytical solution is possible, for example, coils for specific body parts can be designed. To design a coil using this method a surface on which the coil may lie and a target field are to be provided. This surface is discretized into elements and nodes, using methods of regularization a buildable coil design is derived. As proof of concept a radio-frequency coil is designed for a low field MRI system.

Firstly, the relation between the magnetic flux density and the surface current density are derived followed by the relationship between the stream function and the surface current density. The stream function is the *surface quantity* of the BEM problem, while the magnetic flux density is the *field quantity*. In the Boundary Element Method we assume the surface current density is constant within an element, while the stream function is linear within an element. This assumption makes it possible to separate the contribution of each of the nodes to the magnetic flux density. With a formulation of the magnetic flux density induced by the stream function at a node, a matrix formulation is formed. This matrix formulation forms the basis of the forward- and inverse source problem. In this thesis the underlying principles of this mathematical framework are derived and discussed.

This matrix formulation is used to solve the forward problem. In the forward problem we determine the magnetic flux density according to known stream functions values. The magnetic flux density is then compared to an analytical solution. The forward problem shows that with smaller elements and nodes, the accuracy of the solution increases.

In the inverse source problem, the magnetic flux density is given as a variable and we want to know the stream function values. The stream function values are restricted by the continuity equation and a method to find these boundary locations has been designed. Using these stream function values a wire pattern can be created, a three-dimensional contouring algorithm has been created to find these wire patterns. The inverse source problem is an ill-posed problem, is not stable and does not necessarily provide a feasible solution. Regularization is used to given some freedom to differ from the optimal matrix solution and edit the stream function in such a way that the coil pattern is buildable. Regularization is done using Tikhonov regularization. Different regularization matrices are discussed and a method to regularize on an arbitrary surface has been developed. This method works for arbitrary surfaces, however a certain element structure is needed. To verify the proposed design method, the method is compared to other design methods that require a cylindrical surface and a regular grid. Similar wire patterns are obtained in this case thereby demonstrating that the current design method forms a proper generalization of surface current design methods that require cylindrical surfaces and regular grids.

With a method that is capable of regularizing on an arbitrary surface, a proof of concept has been made. A radio-frequency coil for the Low field MRI system of the Leiden University Medical Center has been created. The design goal of this proof of concept is to create an RF coil that is capable of imaging the complete brain of an adult. A surface design has been created for an adult head with an extension in the neck to be able to image the brain stem.

This design is printed using a 3d printer and has been wired by hand. The coil is tested using a human subject as well as a phantom. From the results it has become clear that it is possible to image the human brain using the coil designed using the Boundary Element Method. It has been shown that the coil can image more than 30 millimeter lower into the skull than a coil that is currently in use. With these results, we have shown this method can be used in practice to create a buildable coil that is fit-for-purpose.

From the simulations and the proof of concept, multiple recommendations have been established. The current method of regularization creates a stable solution but does not optimize for other design variables. For different implementations it might be useful to incorporate a design variable in the regularization. For example, minimize the inductance for the design of a gradient coil or an RF coil optimized for minimal power usage. This design variable could be implemented alongside the current method to ensure a stable solution.

In some situations it might be necessary to reduce the concomitant components of the magnetic field, these components affect the magnetic field strength and thus the measured frequency. By adding these components to the minimization function a coil can be designed which takes into account the minimization of the concomitant components.

While Tikhonov regularization has given buildable results, it might be possible to design different coils using other norms for regularization. This could lead to coils with different characteristics and field distributions which can be advantageous in certain circumstances.

Having a smaller meshing, and thus more nodes, leads to the possibility of less error on the magnetic flux density. It can also lead to small variations in wire trajectories. This can make it hard to build the coil since sharp turns cannot be easily built using a wire with a solid core. To use smaller meshing a smoothing algorithm can be implemented to smooth out small variations.

A big factor in the speed of testing currently lies within the calculations of the magnetic flux density, as a significant amount of calculations have to be made. This calculation is done by discretizing the integral for each of the elements. An analytical solution would increase the simulation speed significantly.

Lastly, in the testing of the RF coil it has become clear that it is hard to calculate system characteristics for example resistance and inductance. Leading to discrepancy in the quality factor and thus the imaging bandwidth. Since this bandwidth greatly influences the signal to noise ratio, it is a vital metric in the design process. A better estimation from simulations would be advised, this could be implemented using data that is gathered from the coil that is built and other coils that might be build in the future.

A

Boundary Element Method Coil design Manual

Boundary Element Coil Design – Manual

By: Teun de Smalen

I. Table of Contents

II. Introduction

In this document the process of designing a coil from a 3d model is shown. The coil is designed using the Boundary Element Method as part of my thesis project. The steps necessary to create a model that is suitable for the boundary element method as well as the implementation and how to run it yourself (using the available code) are given. The programs used are either free, used under educational license or access is provided by the LUMC of TU Delft.

In the first chapter a 3d model, is given and a method to make the boundary 'thin' is shown. The next chapter provides a way method of converting the 3D model into "MATLAB ready"-data. This is done using Python. Chapter 3 discusses the implementation of creating the matrix system used in the Boundary Element Method. The next step is the regularization of the problem and how possible solutions can be chosen. Chapter 4 will discuss the stitching of the separate wires. Chapter 5 provides the possibility of simulating in CST.

As an appendix the several MATLAB functions created, not all of these functions are discussed in the document but might be seen useful to the reader. The following programs are used in this document:

Programs used:

- MATLAB
- Python
- Solidworks (optional)
- Autodesk 3DS MAX
- Autodesk Meshmixer
- CST EM Studio

III. Making your 3D model ready for BEM

In this chapter the method of making your 3D model ready for the BEM are shown. Most 3D models created by programs such as Solidworks are models that are meant to be build physically. Such that everything has a thickness. In the Boundary Element Method we assume the currents are placed on an infinitesimal thin layer. This layer is then discretized into elements, however when a physical model is discretized it leads to a discretization with at least two surfaces. In the next Section a Solidworks model is edited such that it is ready to be used to be discretized. If this is step is not necessary for your model one can move on to section B to create a mesh.

A. Solidworks Model

The example used in this section is based on the coil build in my thesis. The original design is given as Figure 1. Everything apart from the parts where the Boundary Element Method will be used on need to be removed. In this case, that means the rests and most front half circle. This results in Figure 2. The model can then be saved as a '.sldprt' .

Within Solidworks, the file can also be exported as STL and one can skip the next section and move on to Section III.C.

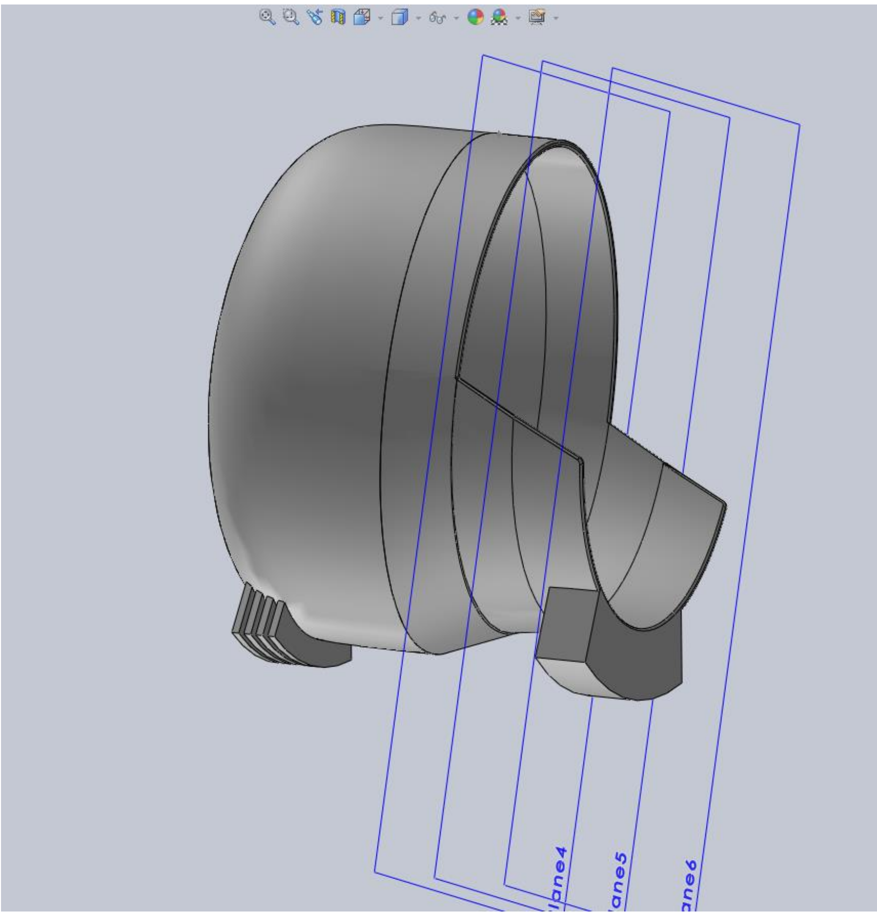

Figure 1 Solidworks Original Model

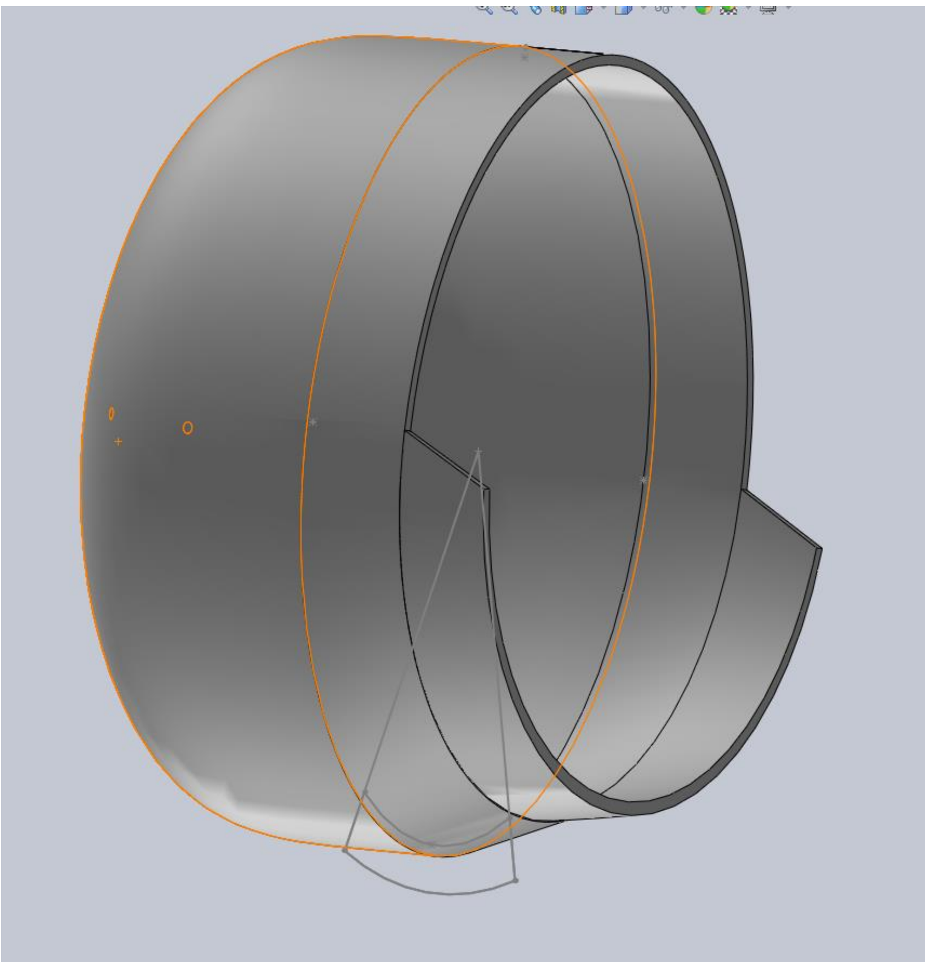

Figure 2 Solidworks model stripped to elements that are part of the Boundary Element Method

B. Meshing the model using Autodesk 3DS Max

With the .sldprt-file we can make it into a mesh using Autodesk 3DS Max. First open 3DS Max, then go to *Customize -> Units Setup* in the top panel as shown below.

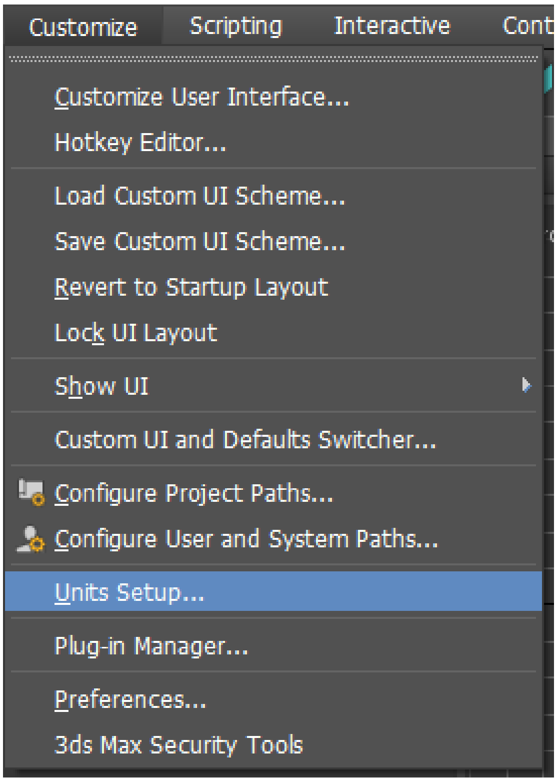

Figure 3 How to get to the Units Setup

In the dialog that opens, press the top button *"System Unit Setup",* another dialog will open. Set this system unit scale to 1,0 meters. If this scale is different and we do not change it, there will be scaling in the exported mesh.

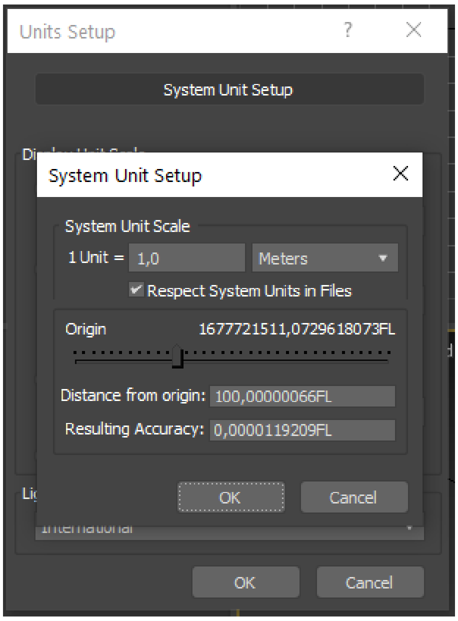

Figure 4 Units Setup Settings

After the unit variables are set, go to *File -> Import -> Import* and select your file.

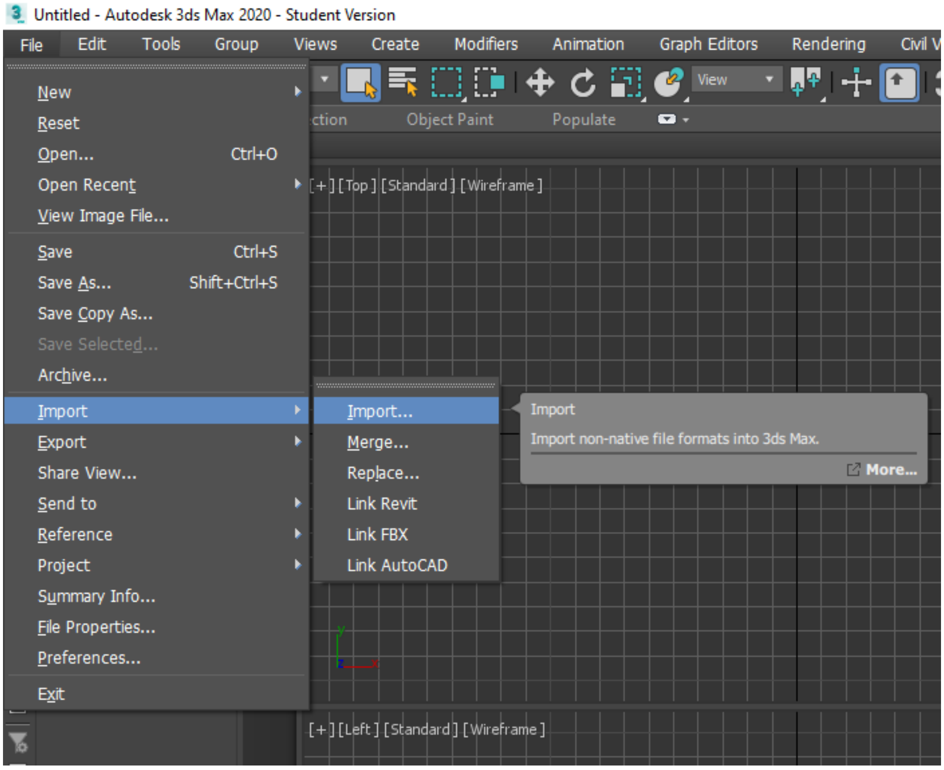

Figure 5 Importing your file into 3DS Max

An import settings window will appear. Convert to Mesh should be "On", the other settings can be changed. The mesh resolution only changes the resolutions in direction of change. In a later step we will still remesh the model so this is not a problem. After changing the settings click 'Import'.

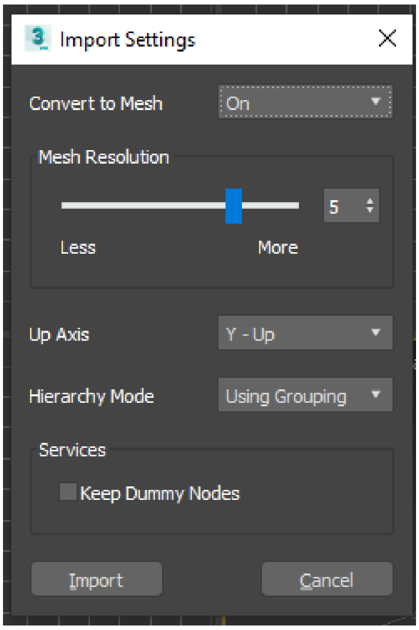

Figure 6 Import settings window

A view such as shown in Figure 7 is given. This model still has an inner- and outer layer as it is build on a physical model.

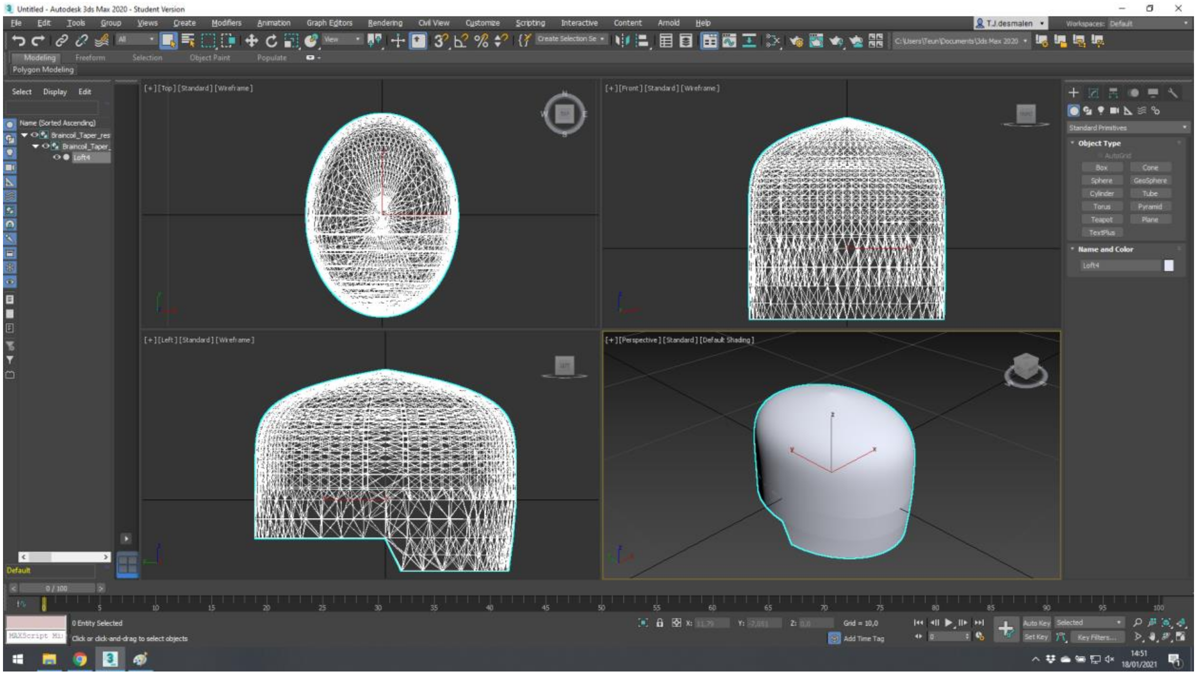

Figure 7 Screenshot of how a model in 3DS Max looks like

This model is now exported by going to *File -> Export -> Export*. Choose the location where you want to save your file and set the "save as type"-option on *"StereoLitho Type (stl)".*

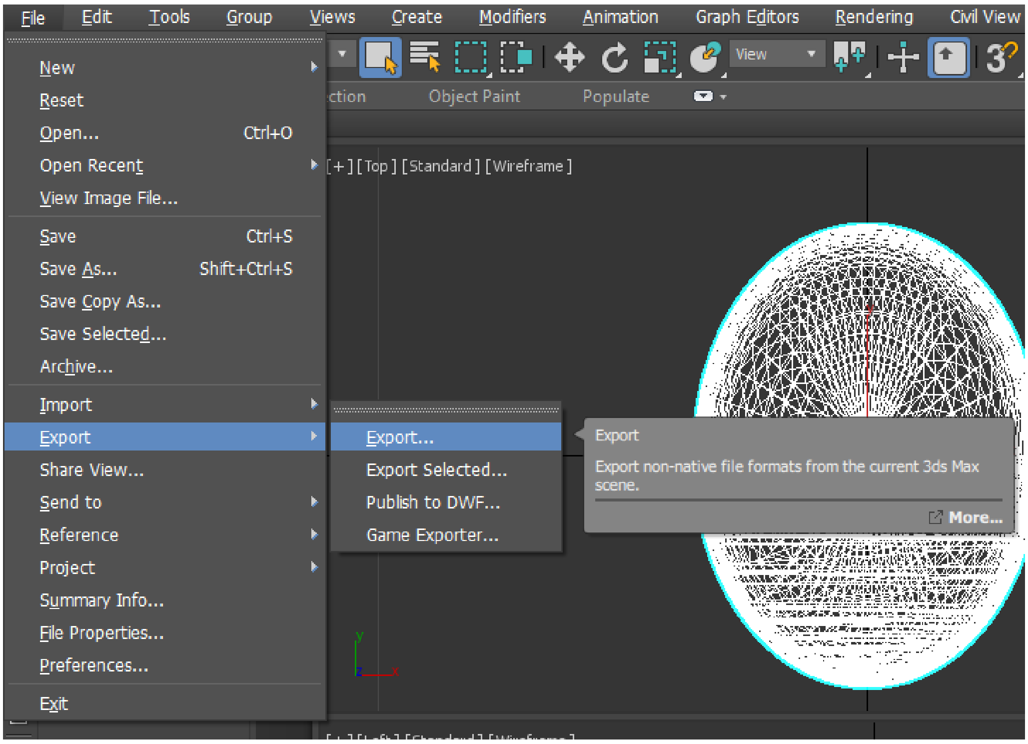

Figure 8 How to get to Export in 3DS Max

In the next step the inner layer is removed and it is shown how to remesh the model.

C. Removing the inner layer in Autodesk MeshMixer

In this step the inner layer of the mesh is removed, such that it is ready for the Boundary Element Method. Also a method of remeshing and a solution to boundary at unexpected locations is given. Start by opening Autodesk Meshmixer.

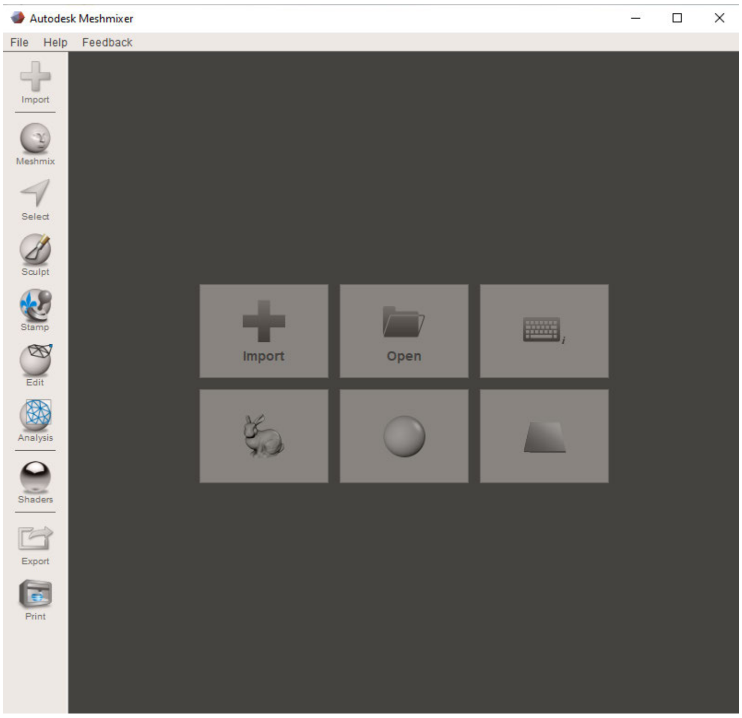

Figure 9 Home screen of Meshmixer

Click the Import button and browse to the ‘stl’-file created in the previous step. The model will now open, in the ‘View’ option at the top the wireframe and boundaries can be toggled on and off. The view can be moved by pressing the middle mouse button, rotated by pressing middle mouse + shift and zoomed by middle mouse + ctrl.

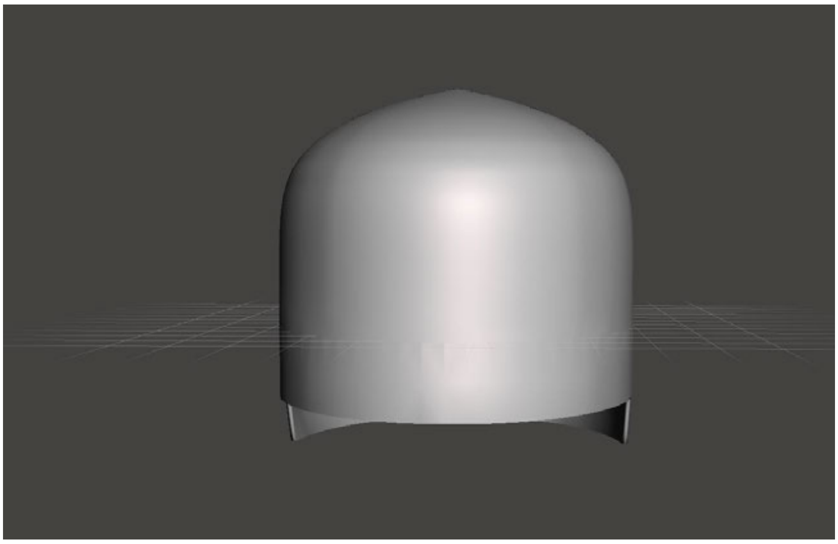

Figure 10 Model opened.

Next go to the “Edit”-tab in the left panel and to “Generate Face groups”. Shown in Figure 11.

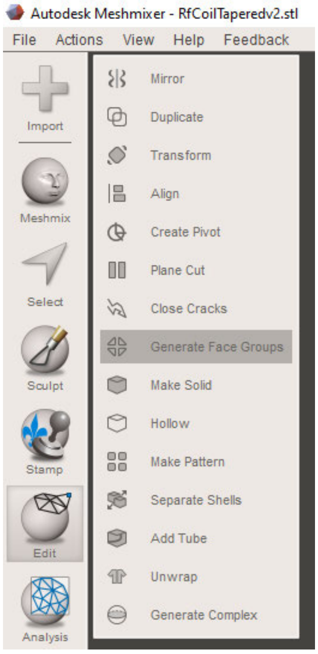

Figure 11 Location where the Face groups option is located

In the top-left corner a settings window opens and the mesh will get different colours. Every colour is a facegroup. Make sure that the inner part and edges have a different colour that the outside, if this is not the case change the thresholds in the settings menu.

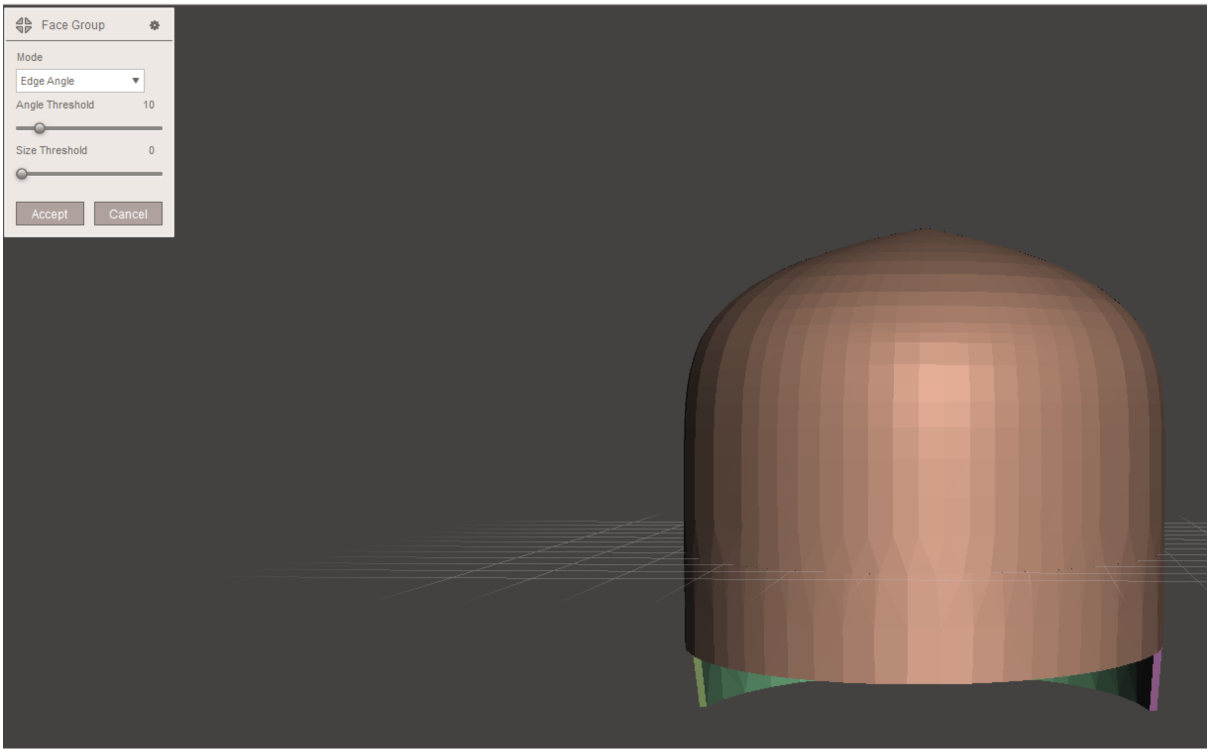

Figure 12 Meshmixer Face Group settings with mesh

In the left panel, click the "Select" – option and go to the inside of the model.

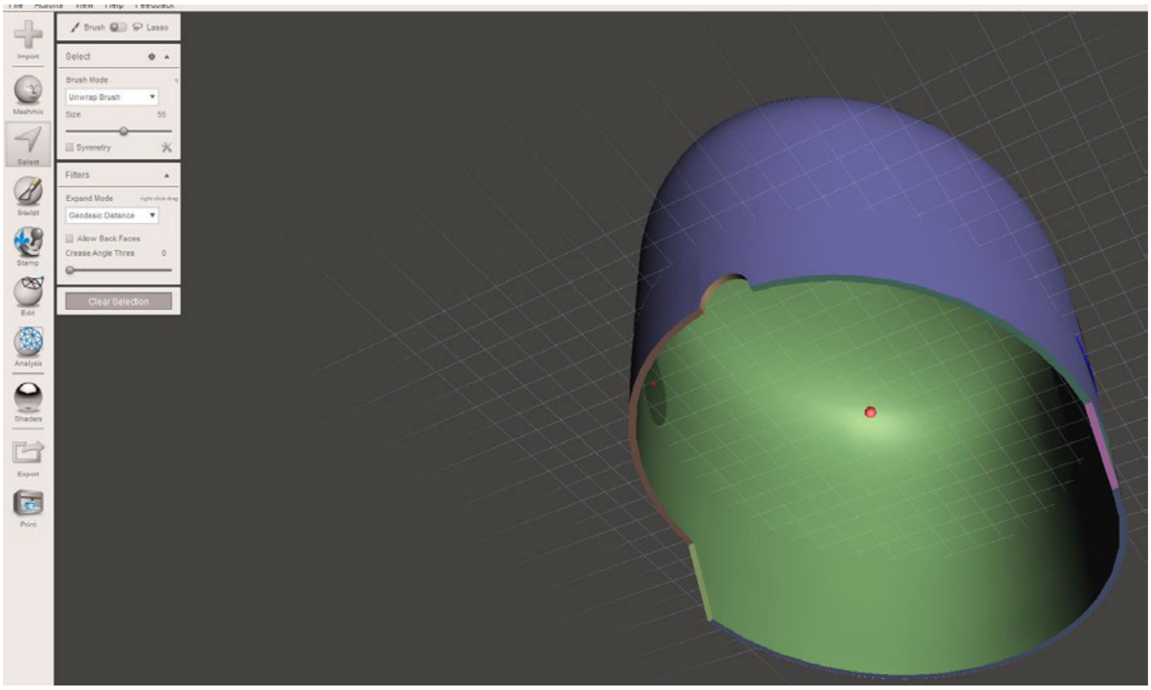

Figure 13 Inside of the model

Click on an element on the inside of the model followed by a key-press on “g” on the keyboard or double-click on the element. The complete facegroup will colour orange.

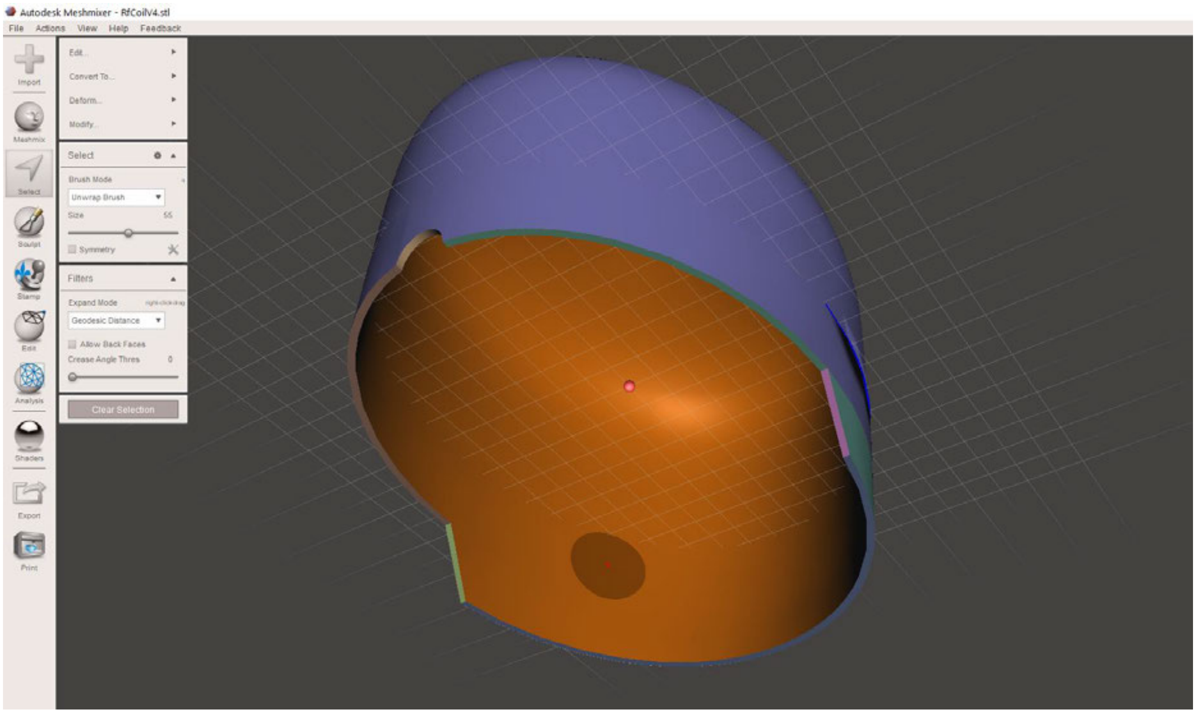

Figure 14 Inside of the model selected.

This can be delete using the “delete” button or “X” button on the keyboard. The triangles inside are now deleted. Do the same for the small edges connecting the inner and outer layer. Such that the model becomes pink.

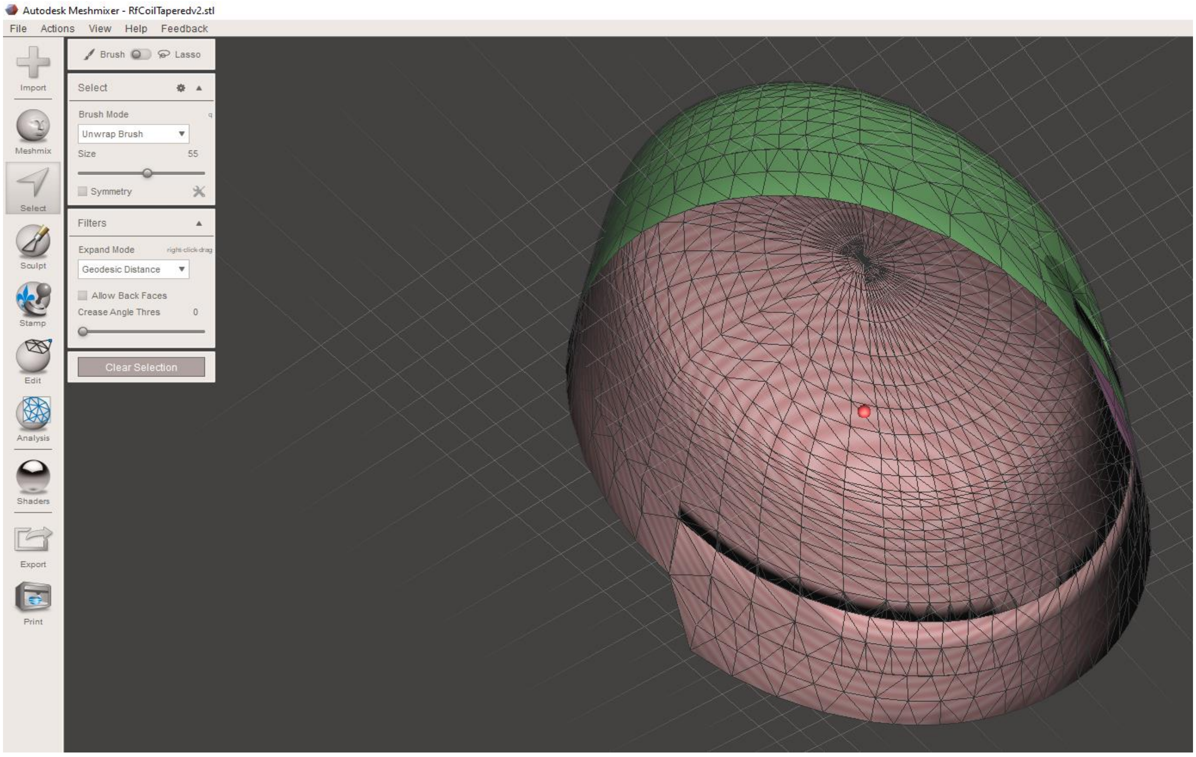

Figure 15 Inside of the model is deleted.

This model is now a thin layer. In the next step remeshing is shown. If you do not want to Remesh one can move on to Section III.F.

D. Remeshing in Autodesk Meshmixer

With the unwanted faces deleted we want to remesh the triangles to more evenly redistribute them over the surface. This can be done by selecting all triangles by going to the *"select"*-tab and clicking on a triangle followed by pressing *"A"*. To select all triangles that are in the model. In the Select menu, go to *"Edit…"* and then *"Remesh"* or by pressing *"R"*.

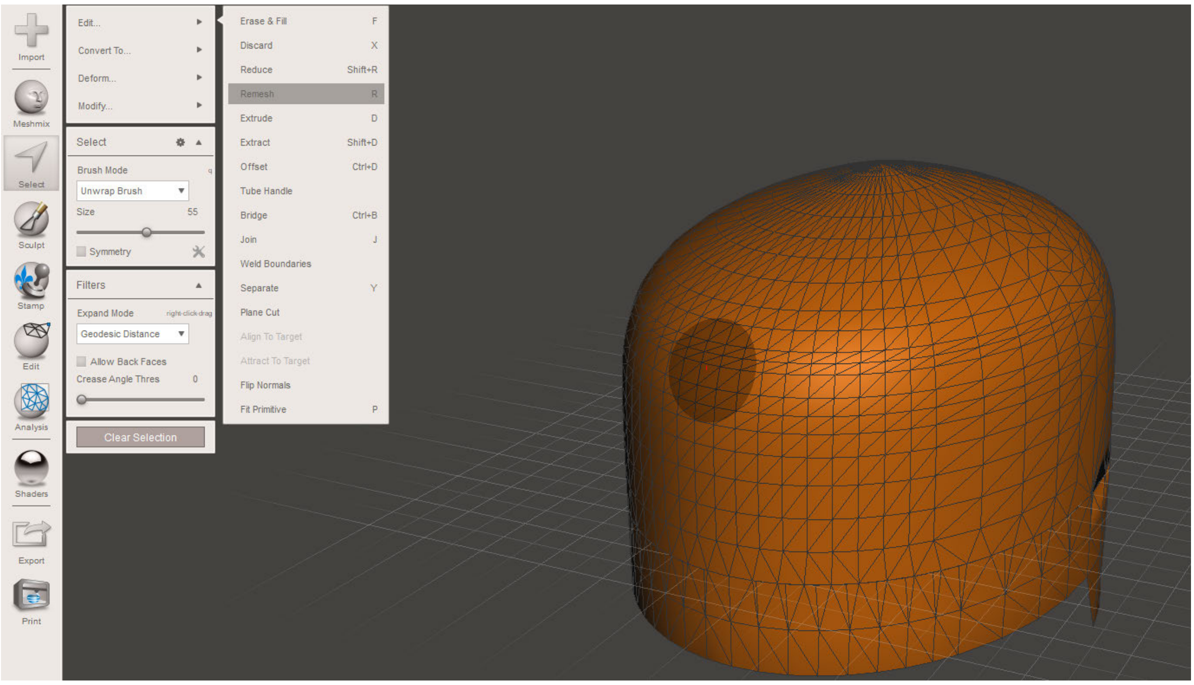

Figure 16 Location of the remesh window

The Remesh-settings will open:

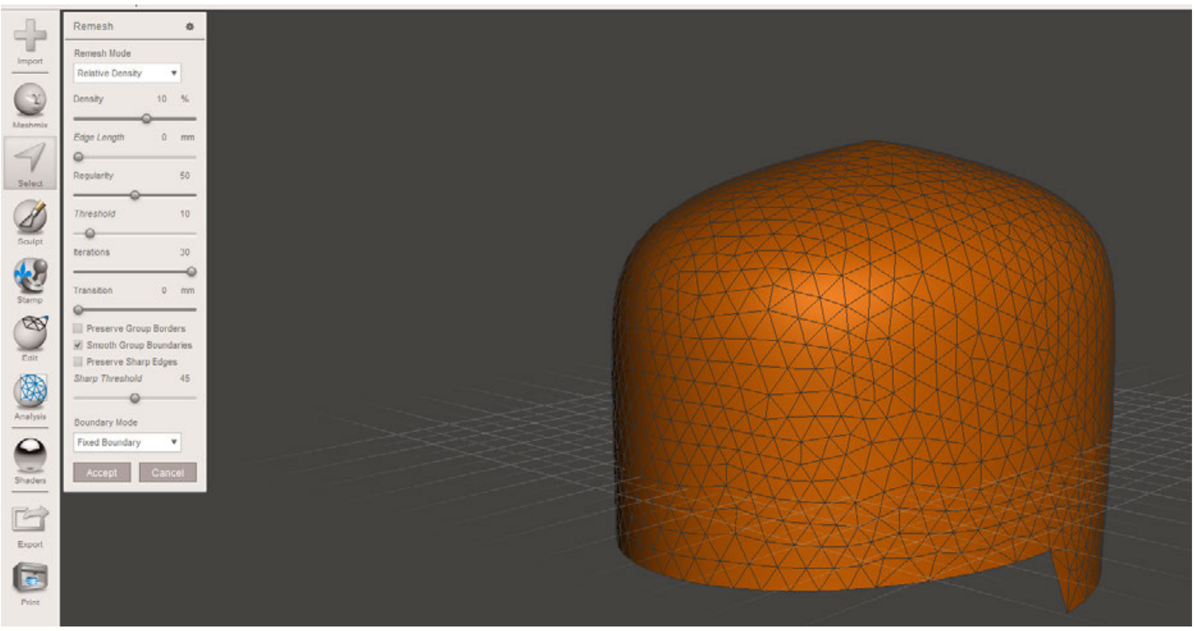

Figure 17 Remesh Window

The window has the following Settings, the dots under give more information. For some I have given my recommendation, for others simply trying is the best to get some hands on knowledge. For more information see the link at the bottom of the page.

- Remesh mode:
    - Recommended choice: Relative Density and Adaptive Density.
  - *Relative Density:*
    - *Changes the size of the triangles relative to the current average size, the result of this option has (on average) equally sized triangles.*
  - *Adaptive Density:*
    - *Places more triangles on areas with more change in geometry.*
  - *Target Edge Length:*
    - *Determines triangles on the target edge length, making this values to small will leads to extremely long processing time. So beware!*
  - *Linear Subdivision:*
    - *Splits existing edges in new edges, usually not recommended as first step. Can be done for a second iteration of remeshing.*
- Density:
  - *Determines the increase of triangle density compared to the current amount of triangles.*
- Edge Length:
  - *Setting for the Remesh mode "Target Edge Length", and is this target edge length.*
- Threshold:
  - *Highering the threshold leads to more deviation of the original model. So be aware with the threshold.*
- Iterations:
  - *The amount of remesh iterations used, the maximum is fine, but on heavy function it is advised to first lower it.*
- Transition:
  - *Only needed when not the complete model is remeshed.*
- Preserve Group borders
  - *Can be toggled on or off, this option makes sure that the face group borders stay the same. Only makes a difference if you have multiple face groups.*
- Smooth Group borders
  - *Can be toggled on or off, smooths the transition between groups.*
- Preserve Sharp Edges
  - *Can be toggled on or off, determines whether or not an certain angle is allowed to be smoothened or not.*
- Boundary Mode
  - *Needs to be on* ***Fixed Boundary*** *otherwise the boundary location will change.*

https://knowledge.autodesk.com/search-result/caas/CloudHelp/cloudhelp/2019/ENU/MSHMXR/files/GUID-6EF8ABD4-AB4A-426F-A0C4-DE96FAABF520-htm.html

E. Removing Boundary at unwanted locations in Meshmixer

The problem described here occurs when two features of a model do not perfectly stitch together. If you do not have this problem, one can move to Section III.F. It is recommended to fix this issue in the original model (i.e. Solidworks) instead of this solution. As this solution not necessarily keeps the geometry completely the same. The blue boundary shows the boundary we do not want, the boundaries can be toggled on and off in the View panel at the top. The first step is to select the triangles located around the edge, as highlighted below.

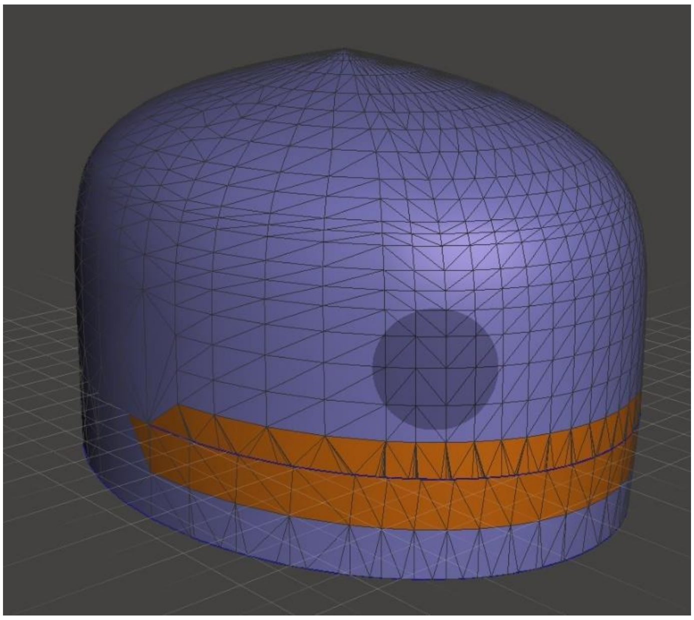

Figure 18 Model with Boundary located at a wrong location (given by the blue line).

Now delete these triangles using either the “X” or “delete” key on your keyboard. Select the surrounding points around this new edge, such that one gets the following

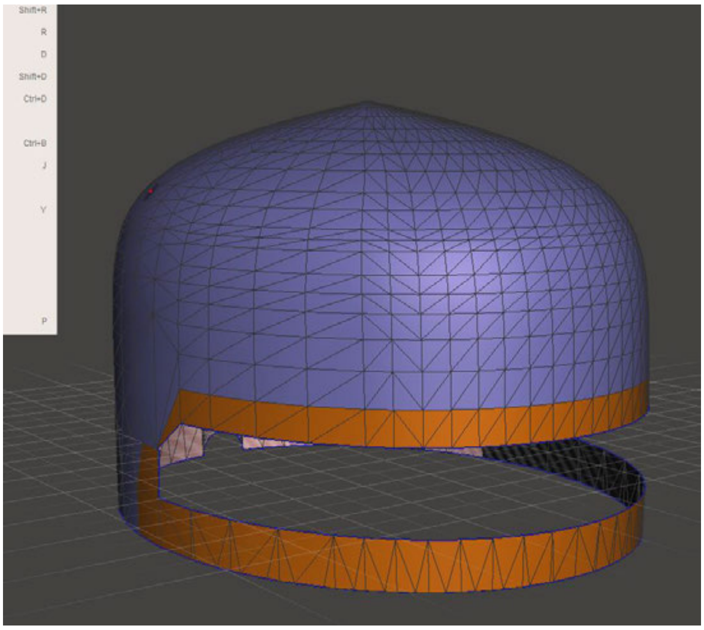

Figure 19 Points removed as part of the correction

Now go to the Erase & Fill option located in *Select -> Edit -> Erase & Fill*.

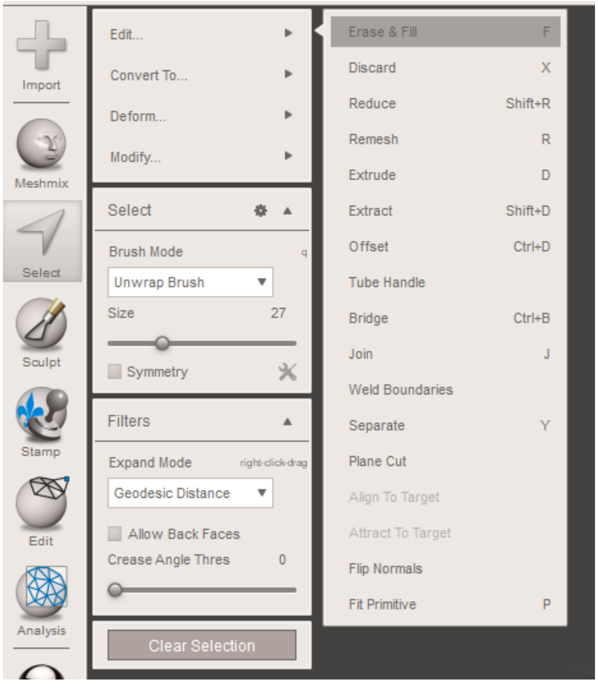

Figure 20 How to get to the Replace and Fill Option

The following settings panel will open.

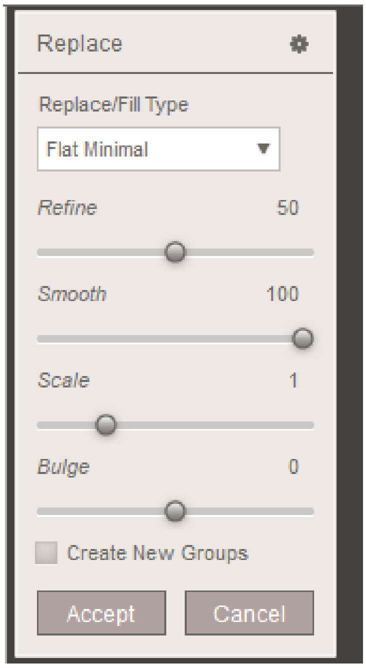

Figure 21 Replace and Fill Settings Panel

The type used can be either *Flat minimal* (for areas with relative low curvature) or *Smooth MVC*, depended on which result is wanted. Simply trying is the best option to find the best fit. After this step remeshing, as discussed in Section III.D, can be reapplied to get similar smoothing over the complete surface.

F. Exporting the model from Autodesk Meshmixer

The last step in this part of the process is to export the model to a suitable format. Go to *File -> Export*.

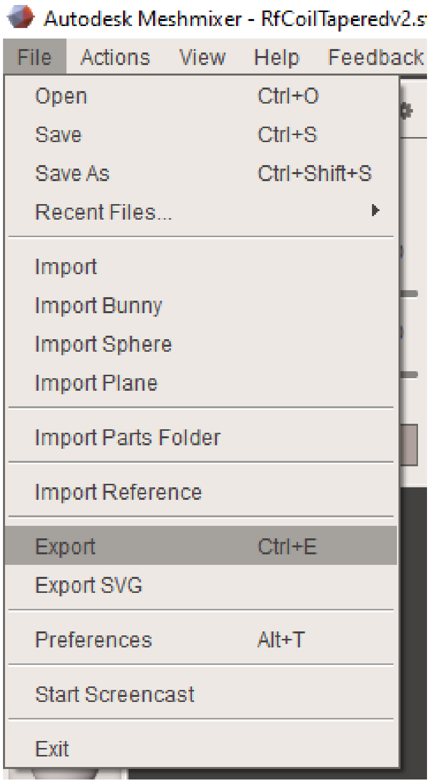

Save the file at the location you want it to be, choose the file type *"COLLADA Format (.dae)"*. This file-type will be used in this next step. It is advised to also save the file using the .mix format as a backup to be used for remeshing in case that is needed.

G. Convert mesh data to ‘.mat’-file

The python script on the next page can be used to convert the ‘.dae’-file type into a ‘.mat’-file type. This script use the following python packages:

- Scipy.io
- Bs4
- Numpy

In the script, the variables DataFile and SaveFile are to be set by the user, you, where DataFile points to the file you are loading the data from and SaveFile is a (new) file you want it to be saved to.

In the ‘.mat’-file two variables can be found:

- NodalCoordinates
  - A Nn by 3 matrix, where Nn is the amount of nodes.
  - Where the ith row contains the coordinates of the ith node.
- TriangleReferences
  - A Nt by 3 matrix, where Nt is the amount of triangles.
  - Contains the references of which nodes combined make a triangle.

```python
#Import data from DAE file type exported using for example Autodesk 3DS MAX
#Written by Teun de Smalen

from scipy.io import savemat
from bs4 import BeautifulSoup as bs
import numpy as np

#User Can Set Paths and filenames here
DataFile = "C:/Path/Mesh.dae"
SaveFile = "C:/Path/MatlabData.mat"
#End of user variables!

#Create .mat-
file with Triangles and Nodes, with variable names TriangleReferences and NodalCoordin
ates
content = []
with open(DataFile, "r")  as file:
    content = file.readlines()
    content = "".join(content)
    bs_content = bs(content, "lxml")

sources = bs_content.find('library_geometries').geometry.mesh.find_all('source')

for source in sources:
    if "position" in source["id"].lower():
        position = source
        break

positions = position.float_array
positions = [x.split(' ') for x in positions.contents[0].strip().split('\n')]
positions = np.asarray(positions, dtype=np.float64, order='C')

elements = bs_content.find("library_geometries").geometry.mesh.triangles.find("p")
elements = [x.split(' ') for x in elements.contents[0].strip().split(' ')]


Triangles = []

for i in range(0, int(len(elements)/9)):
    Triangles.append([float(elements[(i-1)*9][0])+1, float(elements[(i-
1)*9+3][0])+1, float(elements[(i-1)*9+6][0])+1])


if len(positions[0]) != 3:
    positions = np.reshape(positions, (int(len(positions[0])/3),3))
savemat(SaveFile, {"TriangleReferences": Triangles, "NodalCoordinates": positions})
```

IV. MATLAB Data Processing – Determining Magnetic Field

In this chapter, the matlab data processing is discussed. It is assumed both the variables 'NodalCoordinates' and 'TriangleReferences' are present, as these have been made in the previous chapter. The corresponding MATLAB files and functions can be found in the folder 'Step2DetermineField'. The main file is called 'mainCalcField.m'. First the Visual Functions are discussed, followed by the setup in main file.

A. Visual Functions:

The functions used are split into two families:

```
PlotGrid(NodalCoordinates, ElementReferences, TargetLocations)
```

This function creates a 3d plot of the mesh surface. Both NodalCoordinates and TriangleReferences are necessary. If Locations is empty, then no Locations are plotted.

```
PlotGridWithNormals(NodalCoordinates, ElementReferences, TargetLocations)
```

This function creates a 3d plot of the mesh surface with the normals of each of the triangles. These normal should all be in the same direction. Both NodalCoordinates and TriangleReferences are necessary. If Locations is empty, then no Locations are plotted.

```
PlotGridFilled(NodalCoordinates, ElementReferences, StreamF, colorbar)
```

This function creates a 3d plot of the mesh surface with the surface filled and not see-through. StreamF should be a vector of the length of NodalCoordinates. Can be filled with for example ones, which will lead to a same color.

B. Main file:

The main file runs through the following steps:

- Load meshdata or choose a function that has been designed to create a mesh.
- Design the target locations
- Set Filename to in which file to save the data.
- Set the segmentation for the amount of points used in the midpoint-rule (about 100.000 is reasonable).
- Check for duplicate nodes and merge found duplicates.
- Check if all normals of the triangles are in the same direction and change the normal direction if not in the right direction.
- Calculate the magnetic flux density components of the A matrix. (This takes a while)
- Saving the data to file.

V. MATLAB Data Processing – Finding stream function with regularization

In this step the regularization is used to determine the stream function values. The code can be found in the folder ‘Step3Regularization’ in the file ‘mainRegularization’. The important variables created in this function are.

- `Lambda_list` – contains the different regularization parameters lambda.
- `X` – contains the stream function results, where the *i*th column corresponds to the *i*th regularization parameter from Lambda_list.

In the following subsections, the different steps of the file ‘mainRegularization’ are discussed.

A. Locations

In this step a subset of the target locations can be made on which the regularization will be done. An example is given in the corresponding matlab-file.

B. Set target values of Locations

For these Locations target values need to be set in the vector **b.** For example a x-gradient could be made with a strength of 0.2mT/m:

```
b = 0.2E-3*Locations(:,1);
```

C. Component of Magnetic flux density

A component of the magnetic flux density needs to be chosen. Either Ax, Ay or Az can be used. Which are the components of the magnetic flux density.

D. Regularisation matrices

Either of these regularisation matrices can be used in the reguarlisation.

```
L = CreateLArbitrarySurface(NodalCoordinates, TriangleReferences);
```

Creates the regularization matrix for an arbitrary surface using the method discussed in the thesis.

```
L = CreateL2ndOrder(NodalCoordinates);
```

Creates the regularization matrix for a cylinder with a regular grid. If this not a regular grid, this code will not work.

```
L = speye(size(NodalCoordinates,1));
```

Creates the regularization matrix as an identity matrix, such that the regularization matrix minimizes x.

E. Edge matrix

This function determines the edges on which the stream function needs to be constant.

```
[L_edge] = CreateLedge(TriangleReferences);
```

F. Set Lambda’s for regularization

“`Lambda_list`”, is a list of lambdas for which we want to determine the stream function.
“`lambda_edge`”, is the lambda for edges. Needs to be big compared to the lambda’s of lambda_list.

VI. MATLAB Data Processing – Interpretation of regularized data

In this step the several functions that can be used to make a choice on which regularization pattern is chosen. The functions designed will be discussed here. In the corresponding matlab file some extra options are available but not discussed here. The file is found in the folder 'Step4ChooseReg' and is called 'mainChooseReg'. The main variables of the previous section were X and `Lambda_list`, these can be used in for example the lcurve and plot the sensitivity versus lambda.

```
lcurve(A,X,b,LambdaList,IList)
[Sensitivity] = SensVSLambda(X,LambdaList,NumWires, Comp, WireRadius);
```

For the other functions a choice needs to be made to run these functions of X.

```
x_used = X(:,15);
```

A wire pattern can be determined from this using the function Contouring3D, as:

```
[XArray, YArray, ZArray, current] = Contouring3D(NumWires,
NodalCoordinates, TriangleReferences, x_used);
```

The following function shows the stream function on the grid.

```
PlotGridFilled(NodalCoordinates, ElementReferences, StreamF, colorbar)
```

The following function shows the wire pattern (colors might be off sometimes) :

```
PlotWires(XArray, YArray, ZArray, current)
```

The following functions are able to display the Magnetic flux density on slices throughout the media, both functions have quite some variables which are discussed within the function as well as in the main file of this step.

```
PlotErrorSlices
PlotErrorSlicesRelative
```

The following functions determine certain parameters using the wire pattern.

```
R = Resistance(XArray, YArray, ZArray, WireRadius);
L = Inductance(XArray, YArray, ZArray, current);
Length = WireLength(XArray, YArray, ZArray);
[Bx, By, Bz] = CalcBFromWires(XArray, YArray, ZArray, current, Locations);
```

VII. MATLAB Data Processing – Stitching Wires

In this Section the function is discussed that stitches the wires created in the previous steps. The function is named Stitching and is given as, the code is found in the previous step its folder:

```
[XArrayOut, YArrayOut, ZArrayOut] = Stitching(XArray, YArray, ZArray,
current, Stitchdir, Stitchplane, distance, NodalCoordinatesExtraFine)
```

Where `XArray, YArray, ZArray, current` are designed in the previous section.

`Stitchdir` is the direction in which the stitch is made, either 'x', 'y' or 'z'. The stitched is placed around the 0 of this specific direction.

`Stitchplane` is the second direction used to determine where the stitch is placed, can be either 'x', 'y' or 'z'. This parameter determines where the stitches are placed if there are two places. If for example Stitchdir was 'x' and Stitchplane is 'y', than the stitching is done around x = 0 and y < 0.

`distance` is the stitch length. The stitch is made from -distance/2 to distance/2.

`NodalCoordinatesExtraFine` can be left empty. Only needed if the carving does not fit to the surface in SolidWorks. An extra fine mesh can be created using Meshmixer and using the pyhton code made into a MATLAB file. An example of an extra fine mesh is given below. The location of wires is then fitted to the NodalCoordinate locations of the extra fine mesh.

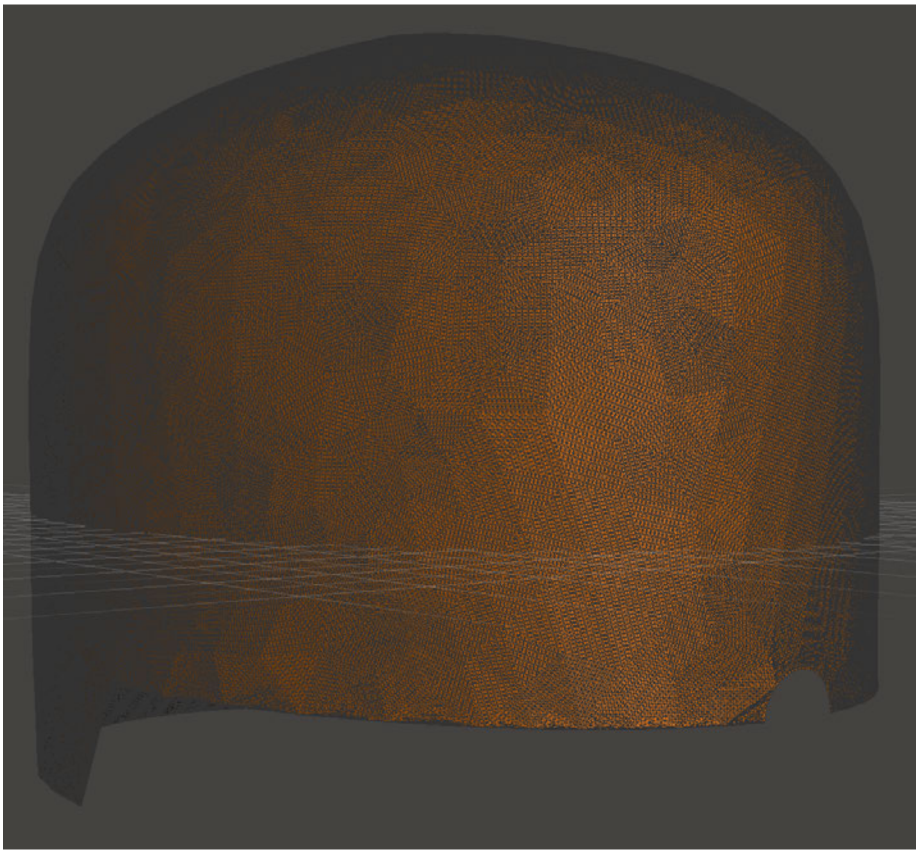

Figure 22 Extra Fine Mesh made in Meshmixer

VIII. MATLAB Data Processing – Move data to CST EM Studio

From the wire pattern one can use an electromagnetic solver to verify the simulations and to get further information about the rf coil. This is implemented for CST EM Studio, the code for this can be found in the folder 'Step6WiresToCST'. The code here has originally been created by Sander van Katwijk, edited by Bart de Vos and further changed to fit the purpose here used. The function `WirePatternToCST` can be called.

```
WirePatternToCST(XArray, YArray, ZArray, current)
```

Where the XArray, YArray, ZArray contain the wires of eaceh of these coordinates and current contains the current component for each of the wires. This function works with separate wires as well as with the stitched wire pattern.

CST will open and a new project will be started where the design is placed in.

IX. Solidworks – Wires on surface

The method in this thesis to print the wire locations is to “carve out” these wires in Solidworks. First the wires need to exported from MATLAB. If the wires are stitched the following lines of code can be used to export the wires to a ‘.txt’-file that can be used in Solidworks.

```
Wires = [XArray YArray ZArray]*1000;
writematrix(round(Wires,4), 'Wires.txt','Delimiter','space')
```

The values are separated by spaces and this file can be imported in Solidworks. In Solidworks, open the original file where the discretized surface is based on. Go to the “Features”-Tab, “Curves” and choose “Curve Through XYZ Points”. Click on Browse and load the ‘.txt’-file.

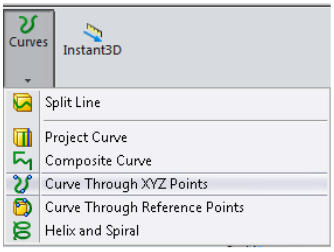

Figure 23 Curve Tab

Next go to the “Features”-Tab, “Reference Geometry”, “Point” and choose either the begin or end of the curve created.

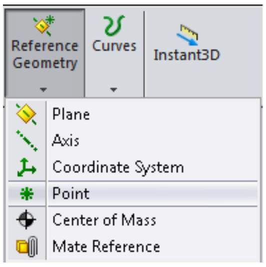

Figure 24 Reference Geometry Tab, chose Point

Next go to the “Features”-Tab, “Reference Geometry”, “Plane” and choose the point just created followed by one of the reference planes. The plane that is perpendicular to the direction of the curve should be chosen.

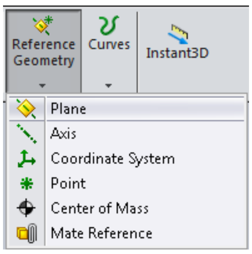

Figure 25 Reference Geometry Tab, chose Plane

Next go to the “Sketch”- Tab, choose either the circle (top row, second from left) or ellipse (second row, third from left).

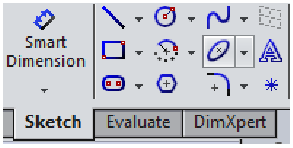

Figure 26 Choose either the ellipse or Circle

Choose the point as location where to place the ellipse or circle. For the ellipse choose the direction parallel to the surface and second direction will be perpendicular to the surface. The lengths can be changed in the bottom left. The depth can be changed accordingly and is given here as 0.9 millimetres and 0.6 mm as radius for the width. This is for a wire radius of 0.5mm so there is a margin of 0.1 mm.

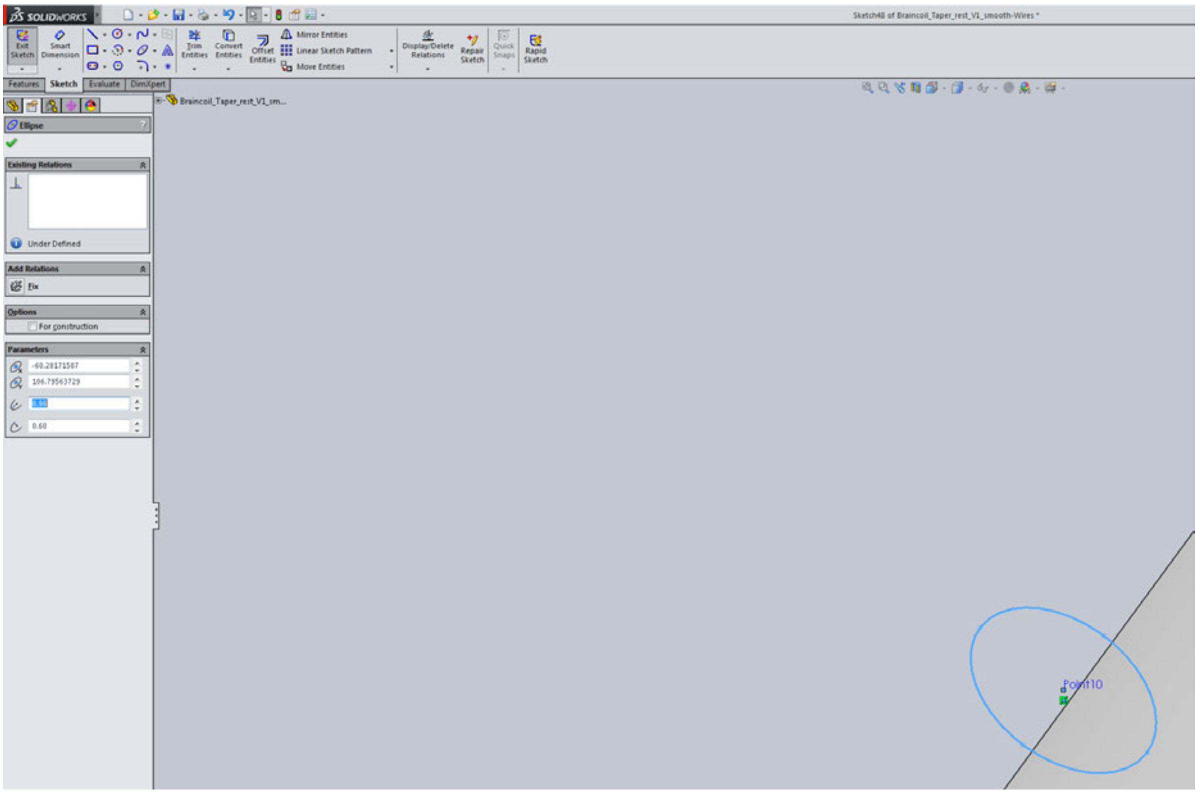

Figure 27 Ellipse created on the surface.

Lastly, a swept cut needs to be done to edge out the wires. Which can be found in “Features”, “Swept Cut”.

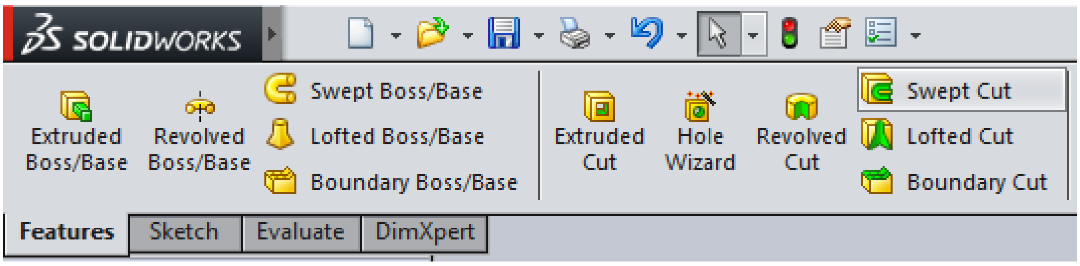

Figure 28 Swept Cut in menu

The menu is as in Figure 29, the first option that needs to be chosen is the circle or ellipse. The second is the Curve. In the Options tab, “Twist Along Path” works best.

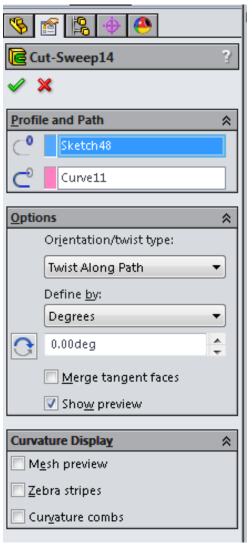

Figure 29 Swept cut menu variables

Finally accept the changes and this loading may take a small while. Sometimes, the wire does not load this can mean that there are too many locations. In for example Notepad++ a macro can be created to delete certain entries to decrease the amount of nodes.

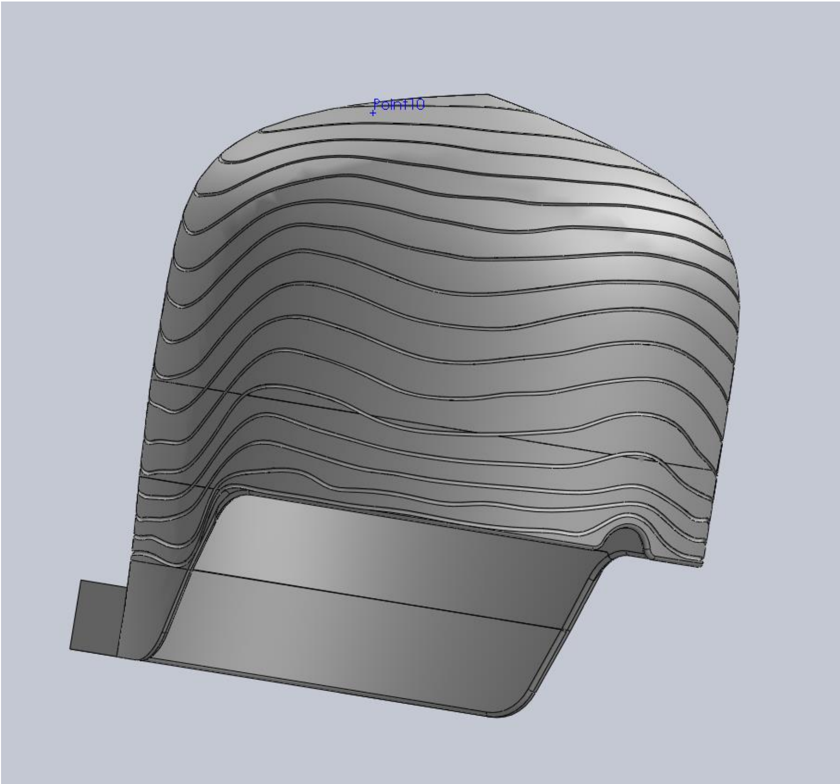

Figure 30 Result of the swept cut surface

If the carved out path is not showing up at certain locations, please refer back to Section VII and use the method with the extra fine mesh.

Bibliography

[1] National Health Service. Hydrocephalus. [Online]. Available: https://www.nhs.uk/conditions/hydrocephalus/

[2] N. B. Smith and A. Webb, *Introduction to medical imaging: physics, engineering and clinical applications*. Cambridge university press, 2010.

[3] T. O'Reilly, W. Teeuwisse, and A. Webb, "Three-dimensional mri in a homogenous 27 cm diameter bore halbach array magnet," *Journal of Magnetic Resonance*, vol. 307, p. 106578, 2019.

[4] S. Shen, Z. Xu, N. Koonjoo, and M. Rosen, "Optimization of a close-fitting volume rf coil for brain imaging at 6.5 mt using linear programming," *IEEE Transactions on Biomedical Engineering*, 2020.

[5] R. Turner, "Gradient coil design: a review of methods," *Magnetic resonance imaging*, vol. 11, no. 7, pp. 903–920, 1993.

[6] ——, "A target field approach to optimal coil design," *Journal of physics D: Applied physics*, vol. 19, no. 8, p. L147, 1986.

[7] L. K. Forbes and S. Crozier, "A novel target-field method for finite-length magnetic resonance shim coils: I. zonal shims," *Journal of physics D: Applied physics*, vol. 34, no. 24, p. 3447, 2001.

[8] F. Jia, Z. Liu, M. Zaitsev, J. Hennig, and J. G. Korvink, "Design multiple-layer gradient coils using least-squares finite element method," *Structural and Multidisciplinary Optimization*, vol. 49, no. 3, pp. 523–535, 2014.

[9] S. Pissanetzky, "Minimum energy MRI gradient coils of general geometry," *Measurement Science and Technology*, vol. 3, no. 7, pp. 667–673, 1992.

[10] S. Hidalgo-Tobon, "Theory of Gradient Coil Design Methods for Magnetic Resonance Imaging," *Concepts in Magnetic Resonance Part A*, vol. 36, no. 4, pp. 223—-242, 2010.

[11] R. F. Remis, *Maxwell's Equations - Lecture Notes*, Delft University of Technology, Delft, 2019.

[12] F. T. Ulaby, E. Michielssen, and U. Ravaioli, "Fundamentals of applied electromagnetics 7e," *Boston, Massachussetts: Prentice Hall*, 2010.

[13] D. J. Griffiths, *Introduction to electrodynamics*. Prentice-Hall, 1999.

[14] H. S. Lopez, F. Liu, and S. Crozier, "The equivalent magnetizing method applied to the design of gradient coils for mri," *Proceedings of the 30th Annual International Conference of the IEEE Engineering in Medicine and Biology Society, EMBS'08 - "Personalized Healthcare through Technology"*, pp. 2805–2808, 2008.

[15] B. de Vos, "Gradient coil design and construction for a halbach based mri system," Master's thesis, Delft University of Technology, 6 2019. [Online]. Available: http://resolver.tudelft.nl/uuid:bb09923a-e4b8-45b9-969e-c614e53cdc66

[16] M. A. Brideson, L. K. Forbes, and S. Crozier, "Determining complicated winding patterns for shim coils using stream functions and the target-field method," *Concepts in Magnetic Resonance Part A: Bridging Education and Research*, vol. 14, no. 1, pp. 9–18, 2002.

[17] M. Poole, "Novel Gradient Coils Designed Using a Boundary Element Method," *Concepts in Magnetic Resonance Part B: Magnetic Resonance Engineering*, vol. 31B, no. 3, pp. 162–175, 2007.

[18] R. A. Lemdiasov and R. Ludwig, "A stream function method for gradient coil design," *Concepts in Magnetic Resonance Part B: Magnetic Resonance Engineering*, vol. 26, no. 1, pp. 67–80, 2005.

[19] P. Doust. geometry - rotate-3d-plane. [Online]. Available: https://math.stackexchange.com/questions/375995/rotate-3d-plane

[20] Y. Lee and W. Lim, "Shoelace formula: Connecting the area of a polygon and the vector cross product," *The Mathematics Teacher*, vol. 110, no. 8, pp. 631–636, 2017.

[21] J. R. Nagel, "Introduction to numerical integration," *University of Utah, Salt Lake City, Utah. URL http://www. ece. utah. edu/~ ece6340/LECTURES/Jan30/. PDF soubor Numerical Intergation, poslední přístup*, vol. 8, no. 5, p. 2019, 2012.

[22] J. Jin, *Electromagnetic analysis and design in magnetic resonance imaging*. CRC press, 1998, vol. 1.

[23] G. Kukaba, "The boundary element method: Errors and gridding for problems with hot spots," Ph.D. dissertation, Ph. D. thesis, Eindhoven University of Technology, 2011.

[24] P. C. Hansen, *Discrete inverse problems: insight and algorithms*. SIAM, 2010.

[25] S. Boyd, S. P. Boyd, and L. Vandenberghe, *Convex optimization*. Cambridge university press, 2004.

[26] Hansen P.C., "REGULARIZATION TOOLS: A Matlab package for analysis and solution of discrete ill-posed problems," *Numerical Algorithms*, vol. 6, no. I 994, pp. 1–35, 1994.

[27] *MATLAB Function Reference*, The MathWorks Inc., Natick MA, USA. [Online]. Available: https://nl.mathworks.com/help/pdf_doc/matlab/index.html

[28] Y. Hu, Q. Wang, X. Zhu, C. Niu, and Y. Wang, "Optimization magnetic resonance imaging shim coil using second derivative discretized stream function," *Concepts in Magnetic Resonance Part B: Magnetic Resonance Engineering*, vol. 47B, no. 1, 2017.

[29] S. Kolmanič and N. Guid, "The flattening of arbitrary surfaces by approximation with developable stripes," in *International Workshop on Geometric Modelling*. Springer, 2000, pp. 35–46.

[30] A. Sheffer, B. Lévy, M. Mogilnitsky, and A. Bogomyakov, "Abf++: fast and robust angle based flattening," *ACM Transactions on Graphics (TOG)*, vol. 24, no. 2, pp. 311–330, 2005.

[31] F. de Goes, W. Sheffler, M. Comet, A. Martinez, and A. Kutt, "Patch-based surface relaxation," in *ACM SIGGRAPH 2018 Talks*, 2018, pp. 1–2.

[32] *MeshMixer™*, Autodesk®Inc. [Online]. Available: https://www.meshmixer.com

[33] J. Mispelter, M. Lupu, and A. Briguet, *NMR probeheads for biophysical and biomedical experiments: theoretical principles and practical guidelines*. World Scientific Publishing Company, 2015.

[34] Standford School of Medicine - Stanford University Medical Center. Sagittal image of skull and brain (t1-weighted mri) [7 of 7]. [Online]. Available: https://web.stanford.edu/dept/radiology/radiologysite/site481.html

[35] *Solidworks 2015 x64 edition*, Dassault Systèmes SE (3DS). [Online]. Available: https://www.solidworks.com/

[36] R. Dengler, "Self inductance of a wire loop as a curve integral," *arXiv preprint arXiv:1204.1486*, 2012.

[37] Z. B. Popović and B. D. Popović, *Introductory electromagnetics*. Addison-Wesley, 2000. [Online]. Available: http://ecee.colorado.edu/~ecen3400/Chapter%2020%20-%20The%20Skin%20Effect.pdf

[38] M. S. Raven, "Experimental measurements of the skin effect and internal inductance at low frequencies," *Acta Techn*, vol. 60, pp. 51–69, 2015.